2017

Remote Sensing of Understory Plant Phenology: A Framework for Monitoring and Projecting the Impacts of Climate Change

Laskin, David

UNIVERSITY OF CALGARY

Remote Sensing of Understory Plant Phenology: A Framework for Monitoring and Projecting the Impacts of Climate Change

by

David N. Laskin

A THESIS

SUBMITTED TO THE FACULTY OF GRADUATE STUDIES

IN PARTIAL FULFILMENT OF THE REQUIREMENTS FOR THE

DEGREE OF DOCTOR OF PHILOSOPHY

GRADUATE PROGRAM IN GEOGRAPHY

CALGARY, ALBERTA

JANUARY, 2017

Abstract

Phenology is an integrative environmental science used to examine recurring biological events in nature. The emphasis is in observing recurring plant and animal life cycle stages, especially their timing and relationship with weather and climate. Examples include wildlife migrations, spawning, or the flowering and fruiting of plants. At higher latitudes, temperature has strong physiological control over rates of vegetation development. Variability in seasonal temperature can therefore influence the timing of vegetation phenology and all of the interrelated ecosystem processes that rely on it. Shifts in phenology are one of the first observed impacts of climate change. Increasing temperatures are advancing the timing of spring onset which in turn alters species movement and interactions, increasing the risk of trophic mismatches. Satellite remote sensing provides an efficient means of uncovering broad-scale phenology patterns, however monitoring the comprehensive development of an individual plant species remains a significant challenge. These complexities are exacerbated in forest ecosystems due to interference from overstory canopies on the remote detection of understory vegetation. This research exploits the physiological nexus between plants and temperature as a window through which understory phenology can be observed. A framework was developed to produce daily maps of understory plant phenology using satellite-derived estimates of understory air temperature. It examines the scales at which phenological relationships operate and how they vary in space and time in the southern Rocky Mountains of Canada. It also explores the projected impacts of climate change on phenological timing through mapped scenarios and experimental warming in climate-controlled growth chambers. The framework provides global extensibility to monitor intra- and interannual phenology patterns for any species with distinct seasonal phenology; providing near-real-time ecosystem monitoring for a dynamic alternative to traditionally static, niche-based approaches of environmental modeling.

Preface

This is a manuscript-based thesis prepared in accordance with the Faculty of Graduate Studies Guidelines. Chapters 2, 3, and 4, have been published in peer-reviewed journals, the case study outlined in the introductory chapter was published in the Foothills Research Institute Grizzly Bear Program 2014 Annual Report, and Chapter 5 is currently in preparation for journal submission. The principal chapters have been reproduced under copyright agreements granted by the publishers: Elsevier, MDPI, and Taylor & Francis respectively. I am intellectually responsible for the research design, analysis, graphical preparation, and writing of these works. In the spring of 2016, a letter published in the journal Science (De Frenne and Verheyen) stressed the importance of focusing global attention to the lack of microclimate analysis within the forest understory. This series of publications are my initial contribution to this contemporary conservation focus. The full citations are as follows:

Chapter 2: Laskin, D.N., & McDermid, G.J. (2016). Evaluating the level of agreement between human and time-lapse camera observations of understory plant phenology at multiple scales. *Ecological Informatics*, 33: 1-9.

Chapter 3: Laskin, D.N., Montaghi, A., Nielsen, S.E., & McDermid, G.J. (2016). Estimating understory temperatures using MODIS LST in mixed cordilleran forests. *Remote Sensing*, *8*(8): 658.

Chapter 4: Laskin, D.N., Montaghi, A., & McDermid, G.J. (2016). An open-source method of constructing cloud-free composites of forest understory temperature using MODIS. *Remote Sensing Letters*, *8*(2): 165-174.

Acknowledgements

This thesis would not have been possible without the ideas, support, and friendship of numerous people. The highlight of this research was encountering so many kind and enthusiastic individuals along the way. Foremost among them is Dr. Greg McDermid, the opportunity to have him as a mentor was one of the main reasons I decided to undertake PhD research. He possesses immeasurable patience and is curiously insightful when providing guidance or inspiration.

I feel enormously privileged to have had Dr. Scott Nielsen and Dr. Shawn Marshall on my supervisory committee, as they are both extraordinary scientists. I also thank the external members of my defence committee, Dr. Joseph Piwowar and Dr. Alessanrdo Massolo, for their optimism and critical evaluation of my research.

Thanks to Gord Stenhouse for inspiring this effort in the first place and supporting me throughout, it has been fulfilling to be part of such an effective conservation program. Also, the enduring support of Dr. Steven Franklin has had a profound impact on my graduate experience, and for this I am immensely grateful.

I will not soon forget the help and friendship of Jay Woosaree, Jeff Newman, and everyone at AITF who helped make the climate chamber research a reality.

I thank all of my friends, especially my labmates on the 9th floor of Earth Sciences, this is a special environment where we can come up with great ideas and enjoy the view. Thanks to everyone in the Department and around campus who are now more like family than friends. I am indebted to those of you who offered your time to join me on long drives through the mountains and late night treks through the wilderness.

Most importantly I thank my family for their enthusiasm and indelible support. It is difficult to imagine that this thesis would have been completed without the love of my partner and best friend Gennyne.

For Mom, my brothers on the farm, and the best brother

Table of Contents

Abstract ii
Preface iii
Acknowledgements iv
List of Tables ix
List of Figures xi
List of Symbols, Abbreviations and Nomenclature xiv

CHAPTER ONE: Introduction 1
1.1 Overview 1
1.1.1 Statement of the problem 3
1.1.2 Conceptual Framework 3
1.2 Background 4
1.2.1 Phenology 4
1.2.2 Phenology and Climate Change 6
1.2.3 Remote Sensing of Phenology 8
1.3 Exploring the Controls of Phenology in Western Alberta 13
1.3.1 Rationale 13
1.3.2 Objectives 16
1.3.3 Methods 16
1.3.4 Results 20
1.3.5 Discussion and Conclusion 24
1.4 Research Objectives 26
1.5 Organization of the Thesis 27

CHAPTER TWO: Evaluating the Level of Agreement Between Human and Time-Lapse Camera Observations of Understory Plant Phenology at Multiple Scales 29
2.1 Abstract 29
2.2 Introduction 30
2.3 Methods 33
2.3.1 Study Area 33
2.3.2 Camera Network Observations 35
2.3.3 Field Observations 37
2.3.4 Photo Analysis and Statistics 39
2.4 Results 41
2.5 Discussion 50
2.6 Conclusion 57
2.7 References 58

CHAPTER THREE: Estimating Understory Temperatures Using MODIS LST in Mixed Cordilleran Forests 64
3.1 Abstract 64
3.2 Introduction 65
3.3 Materials and Methods 70
3.3.1 Study Area 70

3.3.2 In Situ T_{ust} Observations....72
3.3.3 MODIS Land Surface Temperature Observations....73
3.3.4 LiDAR-Derived Canopy Metrics....76
3.3.5 Conventional Forest and Topographic Variables....77
3.3.6 Statistical Methods and Model Ranking....79
3.4 Results....81
3.5 Discussion....89
3.6 Conclusions....96
3.7 References....98

CHAPTER FOUR: An Open-Source Method of Constructing Cloud-Free Composites of Forest Understory Temperature Using MODIS....108
4.1 Abstract....108
4.2 Introduction....109
4.3 Methods....111
4.3.1 Study Area and T_{ust} Observation Plots....111
4.3.2 MODIS LST pre-processing....112
4.3.3 Spatially Extending the T_{ust} Models....113
4.3.4 Temporal Gap Filling....114
4.4 Results....116
4.5 Discussion and Conclusion....119
4.6 References....121

CHAPTER FIVE: A Remote Sensing Framework for Mapping the Phenology of Plant Resources Used by Grizzly Bears and Projecting the Impacts of Climate Change....125
5.1 Abstract....125
5.2 Introduction....126
5.2.1 Grizzly Bear Plant Foods....130
5.2.2 Objectives....132
5.3 Materials and Methods....133
5.3.1 Study Area....133
5.3.2 Phenology Observations....134
5.3.3 The Phenology Mapping Framework....136
5.3.4 Air Temperature Modeling Using MODIS LST....138
5.3.5 Growing Degree Days and Developmental Threshold Temperature Calculation....141
5.3.6 Phenology Map Development....143
5.3.7 Map Validation....144
5.3.8 Future Climate Scenarios....145
5.3.9 Growth Chamber Observations....146
5.4 Results....147
5.4.1 Baseline Phenology Maps....147
5.4.2 Growth Chamber Observations....149
5.4.3 Future Climate Scenarios....150
5.5 Discussion....156
5.5.1 Baseline Phenology Maps....156

5.5.2 Extensibility of the Framework 159
5.5.3 Growth Chamber Observations 164
5.5.4 Climate Projections and Effects on Grizzly Bears 165
5.6 Conclusions 169
5.7 References 171

CHAPTER SIX: Conclusions 187
6.1 Research Objectives Summary 188
6.2 Research Contributions 193
6.3 Recommendations for Future Research 196
6.4 Bibliography 201

List of Tables

Table 1.1 Satellite sensors and datasets used for phenological research (adapted from Reed *et al.*, 2009). 9

Table 1.2 Estimated model parameters for top-ranked AIC models of *Shepherdia canadensis* phenological timing. For Julian day (jday), the quadratic term of Julian day (jday^2), mean annual tempertaure (mat), the spring values of the multivariate El Niño inde*x* (mei_mar_apr), and the interaction term (*). Raw coefficients and Standard errors (in parentheses) are presented. 21

Table 1.3 Green-up, senescence, and reproductive model prediction RMSE validation showing phenophases with the best and worst prediction accuracy (in days). 21

Table 2.1 Phenophase codes for woody (*Shepherdia canadensis*) and herbaceous (*Hedysarum alpinum*) plants, adapted from Dierschke (1972). 38

Table 2.2 Level of agreement (weighted kappa) between phenological observations made through image interpretation and by field personnel and across three spatial scales. 44

Table 2.3 Average variation ratio (variation) expressed as the percent (%) of non-mode observations, and average range of phenophases observed per site visit at the neighbourhood and pixel-scales. 45

Table 2.4 Comparison of the level of agreement between plant-scale camera observations in relation to phenological observations at the neighbourhood and pixel-scales. 46

Table 2.5 Average mismatch (in days) of field observations vs. camera observations at the plant-scale. Negative values denote camera interpretations occurring earlier than the corresponding field observation, and positive values later (refer to Table 2.1 for phenophase code names). 49

Table 2.6 Advantages and disadvantages of digital repeat photography for assessment of structural phenophases in the understory. 56

Table 3.1 LiDAR-derived forest canopy metrics/T_{ust} explanatory variables. 77

Table 3.2 Conventional explanatory variables used for modeling understory temperature. 79

Table 3.3 Baseline Akaike information criterion (AIC) model rankings (top 10) showing relative performance of conventional and LiDAR-derived variable types, as well as individual variable contributions in estimating T_{ust} using all clear-sky (day–night) observations. Model rank was assessed through difference in AIC values (Δi) and weights (w_i) reflecting model likelihood. Model complexity is characterized by the number of model parameters (K_i). 83

Table 3.4 AIC ranking of the top day-night, night, and daytime models within the candidate groupings of conventional, LiDAR-derived, and the combined metrics to predict T_{ust}. 84

Table 3.5 Estimated parameters for the top-ranked models from each overpass dataset. Standardized coefficients and standard errors (in parentheses) are presented by model..... 86

Table 3.6 Comprehensive results of the top-ranked T_{ust} models. Coefficient of determination (R^2), mean absolute error (MAE), root mean square error (RMSE) . 87

Table 4.1 Plot-scale regression estimates of average daily T_{ust}..... 117

Table 5.1 Reproductive phenophases of Canada buffaloberry (*S. canadensis*) 135

Table 5.2 *Shepherdia canadensis* baseline map start dates (day of year) validated against in situ ground observations. Average start dates by phenophase and the difference between them (in days) are shown for the entire study area, individual subregions, and the mean absolute error (MAE) in days at the pixel-scale. Negative values indicate an underestimation by the map. Fully Ripe is highlighted to indicate the timing of peak nutrition. The lowermost row displays the overall duration between the beginning of flowering and peak nutrition. 149

Table 5.3 The summary of present day and future spatial and temporal changes in critical *Shepherdia canadensis* phenophases within the study area. The appearance of first flower acts as a proxy for start of season, first ripe represents the beginning of a critical foraging period for grizzly bears, and fully ripe marks the peak of available nutrition. Phenophase start times and the time of peak coverage are day of year, elevation in meters above sea level, extent of peak spatial coverage in square kilometers. Table rows display the baseline scenario values followed by the amount of shift experienced under the B1 (moderate) and A2 (aggressive) warming scenarios. 153

Table 5.4 *Hedysarum alpinum* map start dates (day of year) validated against in situ ground observations. Average start dates by phenophase and the difference between them (in days) are shown for the entire study area, individual subregions, and the mean absolute error (MAE) in days at the pixel-scale. Negative values indicate an underestimation by the map. 1st Leaf Unfolded is highlighted to indicate the timing of peak nutrition. *Snowfall in subalpine. 161

List of Figures

Figure 1.1 *Shepherdia canadensis* bearing ripe fruit. 15

Figure 1.2 Study area and *Shepherdia canadensis* phenology observation sites..... 17

Figure 1.3 Green-up and senescence *Shepherdia canadensis* vegetative models predictions of interannual phenological variability based on the minimum, maximum, and neutral Multivariate El Niño Southern Oscillation Index (MEI) values occurring during the study period, 2008-2010. 23

Figure 1.4 *Shepherdia canadensis* reproductive model predictions of interannual phenological variability based on the minimum, maximum and average mean average temperature (MAT) values occurring during the study period, 2008-2010. 24

Figure 2.1 Study area extent and observation plot locations throughout the Rocky Mountains of western Alberta, Canada. Highest plot elevation: 1800 m, lowest: 800 m. 35

Figure 2.2 Mounting system and camera placement relative to *Shepherdia canadensis* (foreground) and *Hedysarum alpinum* (background). 36

Figure 2.3 The three observation scales of vegetation phenology: Plant, Neighbourhood, and Pixel 39

Figure 2.4 Examples of landmark phenophase images of *Hedysarum alpinum* (a) and *Shepherdia canadensis* (b). 43

Figure 2.5 Relative average phenophase durations of the focus species highlighting the increased temporal brevity of both the early-season and reproductive phenophases…….50

Figure 3.1 Study area extent and understory temperature observation plot locations. 71

Figure 3.2 Understory temperature (T_{ust}) observation plot and sensor locations..... 72

Figure 3.3 Simplified flow chart of the understory temperature modeling process. 74

Figure 3.4 Example observation plot sample transects of tree species composition prism sweep sites (percent confer) and hemispherical photography locations (percent closure)..... 78

Figure 3.5 Spatial and temporal characteristics of the valid Moderate Resolution Imaging Spectroradiometer (MODIS) overpass dataset including spatial distribution of total clear-sky MODIS overpasses for each observation plot. Also, the proportional percentage of total clear-sky overpasses by month, and the proportional percentage of valid clear-sky observations versus all potential MODIS observations (cloud contamination) for the duration of the study period. .. 81

Figure 3.6 In situ understory temperatures vs. predicted T_{ust} values estimated using the top-ranked models for (a) day and night; (b) daytime; and (c) night. These validation data were collected during clear-sky MODIS overpasses within a nearly-deciduous (6% conifer) observation plot with moderate canopy closure (60%) at an elevation of 1330 m. 88

Figure 3.7 In situ understory temperatures vs. predicted T_{ust} values estimated using the top-ranked models for (a) day and night; (b) daytime; and (c) night. Data are the randomly withheld clear-sky MODIS overpasses of the study area over the duration of the study period. 89

Figure 4.1 Simplified flow chart of the understory temperature (T_{ust}) composite mapping procedure 116

Figure 4.2 Example of removing cloud gaps beginning with a single overpass image (left), increasing coverage by combining all four daily overpasses (centre), and lastly the gap-filled, cloud-free average T_{ust} map. Study area extent shown in inset. Cool regions of the map correspond with high alpine areas. 118

Figure 4.3 Correlation between average daily in situ T_{ust} observations vs. map T_{ust} values at three representative elevations for a single growing season. 118

Figure 5.1 Typical seasonal progression of vegetation consumed by grizzly bears in the central Rocky Mountains of Alberta represented by percent digestible dry matter derived from scat samples. Perennial taproots such as *H. alpinum* are critical in early spring while fruits, such as the berries of *S. canadensis*, are a significant caloric source in late summer and early autumn. (Figure adapted from Bater *et al*. (2011) using data from Munro *et al*. (2006), Table 2). 131

Figure 5.2 The study area is defined by the present-day extent of grizzly bear range in Alberta, Canada. It encompasses three unique ecological subregions: the foothills, montane, and subalpine. 134

Figure 5.3 Procedural flow chart of the phenology mapping framework. The methodology is comprised of three major components: (i) modeling understory air temperature (T_{ust}), (ii) deriving present-day baseline phenology maps, and (iii) deriving projected phenology maps based on two future warming scenarios, moderate B1 and aggressive A2 (IPCC 2014). 138

Figure 5.4 The t_b (threshold temperature) = 0° AGDD requirements for reproductive phenophases of *Shepherdia canadensis* shown against the relative average temporal phenophase duration. 143

Figure 5.5 Example intervals (day of year) of the seasonal accumulated growing degree days (AGDD) derived from the daily average understory temperature (T_{ust}) imagery at 250 m spatial resolution. Cool regions of the map correspond with high-relief alpine and subalpine regions. 144

Figure 5.6 Distribution and seasonal progression of discrete phenophases of *Shepherdia canadensis* across the study area in the baseline year 2012, or present day scenario. Arbitrary intervals used to portray developmental rate over time (day of year). 148

Figure 5.7 Differences in combined observations of developmental phenophase timing between the baseline and A2 warming scenarios for *Shepherdia canadensis*. Temperature values indicate the difference in mean chamber temperatures preceding each phenophase. 150

Figure 5.8 Shifts in phenophase timing and habitat distribution of *Shepherdia canadensis* under future warming scenarios B1 (moderate) and A2 (aggressive) relative to the 2012 baseline. Arbitrary intervals to portray seasonal development (day of year). Habitat niche-extent based on models derived by Roberts et al. (2014) for present day and end-of-century forecasts. 152

Figure 5.9 The timing of maximum spatial coverage of fully ripe *Shepherdia canadensis* under the baseline, B1 (moderate), and A2 (aggressive) warming scenarios. Dates of peak coverage in the warming scenarios clearly advance compared to the baseline by 10 (+1.8°C) and 17 (+3.4°C) days respectively. 154

Figure 5.10 Curves illustrate the area of the landscape (km^2) covered by fully ripe *Shepherida canadensis* across the growing season for the baseline, B1, and A2 scenarios. The circles indicate the timing of peak coverage for the appearance of first flowers as a gauge of developmental start dates. There is a clear seasonal advance in timing that increases proportionately with the amount of projected warming. 155

Figure 5.11 Shifts in phenophase timing and habitat distribution of *Hedysarum alpinum* under future warming scenarios B1 (moderate) and A2 (aggressive) relative to the 2012 baseline. Arbitrary intervals to portray early to mid-season development highlighting the period of peak crude protein (day of year). Habitat niche-extent based on models derived by Roberts et al. (2014) for present day and end-of-century forecasts. 162

Figure 5.12 Curves illustrate the area of the landscape (km^2) covered by peak crude protein in *Hedysarum alpinum* across the growing season for the baseline, B1, and A2 scenarios. Overall, there is a delayed occurrence in peak coverage in the future scenarios compared to the baseline year as a result of upslope habitat migration to cooler regions. 163

List of Symbols, Abbreviations and Nomenclature

Abbreviations:

2G-RBi	Digital Camera Greenness Index
A2	IPCC Emissions Scenario Family, Aggressive
AGDD	Accumulated Growing Degree Days
AIC	Akaike's Information Criterion
AM	Ante Meridiem, before midday
AR5	Fifth Assessment Report on Climate Change
AVHRR	Advanced Very High Resolution Radiometer
B1	IPCC Emissions Scenario Family, Moderate
°Bx	Degrees Brix, Sugar Content in Solution
°C	Temperature in Celsius
CC	Canopy Closure
CDD	Chilling Degree Days
CMIP5	Coupled Model Intercomparison Project Phase 5
DOY	Day of Year
ENSO	El Niño Southern Oscillation
EOT	Equation of Time, see (Eq. 3.2)
ETM+	Enhanced Thematic Mapper
EVI	Enhanced Vegetation Index
FOV	Field of View
°GDD	Growing Degree Days
GEE	Google Earth Engine
GLM	Generalized Linear Model
GLS	Generalized Least Squares Estimator
GPS	Global Positioning System
IPCC	Intergovernmental Panel on Climate Change
JDAY	Julian Day
°K	Temperature in Kelvin
LC	Longitudinal Correction
LiDAR	Light Detection and Ranging
LP DAAC	NASA Land Processes Distributed Active Archive Center
LSP	Land Surface Phenology
LST	Land Surface Temperature
MAE	Mean Absolute Error
MAT	Mean Annual Temperature
MEI	Multivariate El Niño Southern Oscillation Index
MERIS	Medium Resolution Imaging Spectroradiometer
MOD11A1	MODIS Terra Temperature and Emissivity Product
MODIS	Moderate Resolution Imaging Spectroradiometer
MRT	MODIS Reprojection Tool
MSS	Multispectral Scanner System
MYD11A1	MODIS Aqua Temperature and Emissivity Product
NARR	North American Regional Reanalysis

NARCCAP	North American Regional Climate Change Assessment Program
NDVI	Normalized Difference Vegetation Index
PDO	Pacific Decadal Oscillation
PM	Post Meridiem, after midday
QA	Quality Assessment (MODIS)
RGB	Red, Green, and Blue Image Channels
RMSE	Root Mean Square Error
SOS	Start of Season
STDD	Standard Deviation of Canopy Height, see section 3.3.4
T_{air}	Surface Air Temperature
TIR	Thermal Infrared
TM	Thematic Mapper
T_{max}	Maximum Daily Air Temperature
T_{min}	Minimum Daily Air Temperature
T_{ust}	Understory Air Temperature
TVX	Temperature Vegetation Index
VIIRS	Visible Infrared Imaging Radiometer Suite
WH/m^2	Watt-Hours per Square Meter

Symbols:

b	Estimated Model Coefficient
d_i	Number of Days in the i^{th} Case, see (Eq. 5.2)
Δ_i	Change in Akaike Score, see section 3.4
$f(x)$	Function of x
ρ_{nir}	Corrected Near Surface Infrared Reflectance
ρ_{red}	Corrected Near Surface Red Reflectance
t_b	Minimum Developmental Threshold Temperature, see (Eq. 5.3)
T_i	Sum of Daily Mean Temperature, see (Eq. 5.2)
t_s	Solar Time
μ	Image Brightness Value
v	Variation Ratio, see (Eq. 2.2)
w_i	Akaike Weight, see section 3.4; Weighted Kappa, see (Eq. 2.1)
x	Model Covariate
y	Dependent Variable
Z_{AB}	Standardized Z-Score, see (Eq. 2.3)

Keeping records enhances the pleasure of the search

and the chance of finding order and meaning in these events

Aldo Leopold

Chapter One: Introduction

> The study of the annual timing of events such as spring flowering […] embodies one of the clearest and most inherently appreciated manifestations of organism-environment interactions (Post and Inouye 2008).

1.1 Overview

Phenology is the study of recurring biological events and seasonal cycles within nature (Edwards and Richardson 2004). It is an integrative discipline that gives fundamental insight into ecology at the individual level, but can scale interactions to the population, community, and landscape levels as well (Schwartz 2003; Cleland *et al.*, 2007). Across large extents of the planet, the arrival of spring sets forth a wave of green as plants commence their perennial cycle of growth, reproduction, and senescence. The timing of this sequence is closely tied to temperature and climate, becoming increasingly brief and pronounced at northern latitudes (White *et al*., 1999). While it may not be immediately intuitive, slight variabilities in temperature can produce marked changes in the timing of plant development (Busetto *et al*., 2010). This temporal shift can reverberate through the bottom-up ecosystem linkages that rely on the availability of vegetation. Changes in plant phenology has been one of the first observed impacts of climate change (Root *et al*., 2003). If these shifts become too great they will alter species interactions and thus threaten to decouple trophic linkages (Visser and Both 2005).

Time-series mapping of vegetation phenology provides a dynamic alternative to traditional, static landscape maps. They offer a harmonized perspective into the inherently

dynamic processes occurring within ecosystems. Rapid image acquisition from spaceborne sensors perceive inter- and intra-season phenological patterns, and assess ongoing trends in ecosystem responses to climate warming (Zhang *et al*., 2003). Phenology maps express the geographical distribution of the current stages, or *phenophases*, of plant development at a particular point in time. They provide a foundation for evaluating which species interactions are most sensitive to temperature, and help us understand how trophic mismatches can affect community dynamics, ecosystem services, and species conservation over time (Morellato *et al*., 2016).

This thesis works to explore the phenological patterns of plant species inhabiting the forest understories of western Alberta, Canada. This microclimate is of particular research interest because it is home to a threatened population of grizzly bears (*Ursus arctos*). These animals strategically exploit a wide variety of understory plants that provide variable nutrition at differential times of the growing season (Nielsen *et al*., 2003). An improved understanding of phenological diversity and the availability of food-resources will support the long-term management and conservation of grizzlies within the province.

This introductory chapter defines the knowledge gaps and provides the necessary background to prepare the reader for the forthcoming chapters. It encompasses a number of relevant topics including (i) a brief history of phenology and its function in observing vegetation, (ii) phenology as a bioindicator of climate change, and (iii) the technological approaches to monitoring phenology using satellites. Following this is an exploratory case-study that examines an alternate method of modeling phenology to the one ultimately pursued in this research: that of climate proxies. This exploratory work provides insight into the controls of phenological timing in western Alberta and establishes the scale and

intensity of observations on which to base the greater research program. The chapter concludes with a list of specific objectives required to satisfy the overall research goal.

1.1.1 Statement of the problem

Forest ecosystems provide habitat for roughly 65% of the world's taxa (Lindenmayer *et al*., 2006). Of the countless plant-animal interactions taking place within forests, the vast majority occur below the canopy (De Frenne and Verheyen 2016). Detecting understory phenology using satellite imagery is met with a variety challenges. Firstly, the presence of overstory canopy in forests interferes with the remote detection of understory vegetation using Earth-observing sensors (Tuanmu *et al*., 2010). In addition, physical developmental changes of a specific species, such as the appearance of ripe fruit, are fundamentally imperceptible in satellite imagery; and the rapid reproductive phenology common to northern temperate and boreal forests generates phenophases with very brief durations. Lastly, the spatial heterogeneity of phenology can vary over very short distances. This thesis endeavours to resolve some of these intrinsic challenges of monitoring forest ecosystem phenology.

1.1.2 Conceptual Framework

Remote sensing provides a rapid and efficient means of monitoring regional and global vegetation phenology (Schwartz 1999). Linking broad-scale spaceborne metrics to community or species-level development on the ground requires a supplementary estimation technique. Physical or statistical models work to correlate in situ observations on the ground with coincident satellite imagery. Ground observations are now commonly

made using repeat photography from digital camera networks. The phenological progression is typically acquired by extracting the seasonal variation of red, green and blue spectral information from the camera imagery (e.g. Richardson *et al*., 2007; Nagai *et al*., 2016; Nijland *et al*., 2016). This spectral index is related to general phenological events on the ground and then tied to phenology indices derived from the satellite imagery overhead. At present, this approach is highly effective in determining critical seasonal metrics such as the timing of spring onset, autumn senescence, or vegetative maximums. However, temporally isolating discrete physical development of a specific species can only be inferred – especially with structural changes that are not reflected spectrally. A different approach is required to capture short-lived, ecologically significant phenophases. The strong physiological linkage of temperature with plant development provides a gateway to observing phenology below the forest canopy. The remote sensing framework presented hereafter is founded on the use of thermal imagery in generating a connection from the sensor to the understory.

1.2 Background

1.2.1 Phenology

The term was introduced by the botanist Charles Morren in 1853, derived from the Greek words *phainomai*, 'to appear', and *logos*, meaning 'to study' (Demarée 2009). In the context of an integrative discipline, the following definition of phenology is suitably inclusive:

> Phenology is the study of the timing of recurring biological events, the causes of their timing with regard to biotic and abiotic forces, and the interrelation among phases of the same or different species (Lieth 1974).

In plants, insects, and animals, these phenophases can include leaf emergence, flowering, first ripe fruit, molting, mating, hatching, fledging, migrating, or emergence from hibernation (Dube *et al*., 1984). There are dozens of identifiable phenophases, however the number required for an analysis will vary widely depending on the research application, observation method, and species of interest (Meier 2003). The research in this thesis falls under the designation of *phytophenology*: the branch of phenology that encompasses the seasonal rhythm of plants (Defila and Clot 2001). Temperature, photoperiod, and moisture all affect rates of phenological development, but of these, temperature has the greatest effect (Sparks *et al*., 1997). This is because plants require a specific amount of accumulated heat energy in order to move from one phenophase to the next (Magoon and Culpepper 1932). The quantity of heat remains constant each year, but the length of time between phenophases can vary due to variability in weather and surrounding ambient temperatures (Schwartz 2003). Timing and duration is also affected by geographic location and can be factored through *Hopkin's Law* (1918), which states that phenophases will be delayed by approximately 4 days per degree latitude or every 120 m increase in elevation (Campbell 1974). The naturalist Carl Linnaeus put great effort into monitoring the seasonal aspects of living things and relating them to geographical and climatic factors (Puppi 2007). His work manifested in a series of phenological calendars that detailed the seasonal timing of various species in various locations – *Calendaruium florae*, 1756. Observation networks are still

an integral aspect to phenological research and are constantly evolving with the advent of new technologies, from Linnaeus's thermometer to internet-synched digital cameras (Graham *et al*., 2010; Ide and Oguma 2010).

1.2.2 Phenology and Climate Change

There is ample evidence to suggest that twentieth-century climate change has already altered phenologies and living systems (e.g. Parmesan and Yohe 2003; Parmesan 2006; Schwartz *et al*., 2006). Vegetation phenology is one of the most sensitive and easily observable traits in nature that changes in response to climate (Menzel and Fabian 1999; Badeck *et al*., 2004). On average, springtime phenological events have shifted by 2.3 days per decade globally (Parmesan and Yohe 2003; Root *et al*., 2003). There are significant, negative phenological influences to early spring such as exposure to increased frost risk, which can reduce both floral abundance and germination success, impacting the number of surviving individuals the following season (Myking 1997; Inouye 2008; Bennie *et al*., 2009). Disruption of phenological timing also affects the frost hardiness of some plants as well as their photosynthetic capacity (Kramer and Hännien 2009). Inouye and McGuire (1991) found that early reduced snow cover impacts the success of seed production in an early-blooming herbaceous perennial of montane western North America. Bokhorst *et al*. (2008) explained that climate-change scenarios predict an increased frequency of extreme climatic events, and found that a sudden winter warming can lead to near-complete elimination of berry production in some species the following summer. The advance in spring onset will continue along with anomalous weather events as mean annual

temperatures are expected to rise by up to 7°C during this century (worst-case scenario) (IPCC 2014; Friedrich *et al*., 2016).

For every 1°C of average global temperature change, ecological zones can shift up to 160 km (Thuiller 2007). As a result, regions over much of the planet are likely to undergo species incursions, increased competition, and other *ecological surprises* (Williams and Jackson 2007). Sherry *et al.* (2007) found that increased warming accelerates development in early season species, but delays development in later-active species, resulting in an open phenological niche that could facilitate invasion by non-native species. Considering the inherent complexity of climate-species relationships, the exact impact of climate change on phenological interactions is difficult to predict (Araújo and Guisan 2006; Parmesan *et al*., 1999). However, it is known that changes in phenological timing can create asynchrony with mutualistic species, impacting community ecosystem dynamics. This divergence in species interaction escalates the potential for trophic cascades throughout entire ecosystems (Edwards and Richardson 2004; Butt *et al*., 2015). Certain species depend on the coordination of phenophases for survival, such as pollination by insects (Ehrlich 1986; Warren *et al.*, 2010; Kudo and Ida 2013). Insect phenology is also tied to temperature, and an advance or delay in flowering can jeopardize reproduction in that particular plant species (Fenner 1998). The same premise applies to seed dispersers, such as bears, where temporal shifts in fruiting can limit calories for a species that requires abundant nutrition to prepare for hibernation (Davis 2006). Conversely, variation in the timing of phenophases, genetic or otherwise, can be favored by natural selection. This is important for maintaining species coexistence within some plant communities by reducing competition for pollinators and other resources (Rathcke and Lacey 1985). For example, certain temporal outliers may

avoid predatory insect emergence, seed predation from migrating birds, or survive through an unseasonal drought (Richardson and O'Keefe 2009).

As climate warming affects phenology, these changes are in turn impacting climate (Alessandri *et al*., 2007). For example, vegetation phenology plays a crucial role in the carbon balance of terrestrial ecosystems (Nemanill 1997). A major fraction of seasonal CO_2 amplitude is explained by the lengthening of the growing season in mid and high-latitude ecosystems (Keeling *et al*., 1996; Morisette *et al*., 2009; Barr *et al*., 2009). Peñuelas *et al*. (2009) describe that earlier leaf unfolding and delayed abscission due to climate warming will in turn exacerbate climate change as part of a positive feedback loop. Phenological records of substantial duration provide a measure of these biological responses to variations in climate (Spano *et al*., 1999). A detailed global record of phenological dynamics has been amassing for some time through ongoing monitoring by spaceborne sensors.

1.2.3 Remote Sensing of Phenology

As an exemplary interdisciplinary field, phenology did not attract much attention before the age of satellites (Schwartz 1999). The broad perspective offered from this viewpoint reveals trends in phenology that would be difficult, if not impossible, to detect from the ground. Numerous platforms have been employed in the phenological analysis of vegetation since the early 1970's (e.g. Morain 1974) (Table 1.1). Some of these sensors possess lengthy imagery archives for observing long term phenology trends, such as the prolific Advanced Very High Resolution Radiometer (AVHRR) and Landsat. However, the variable spatial and temporal resolutions of the various sensors dictate the scale and

objectives of the research undertaken. Image fusion has worked to some extent as a compromise in bridging this gap (e.g. Hilker *et al*., 2009).

Table 1.1 Satellite sensors and datasets used for phenological research (adapted from Reed *et al.*, 2009).

Platform	Sensor	Operation	Resolution	Frequency
Landsat	MSS	1973-1985	79 m	18 days
Landsat	TM	1984-present	30 m	16 days
Landsat	ETM+	1999-present	30 m	16 days
NOAA	AVHRR	1982-present	8 km	twice monthly
NOAA	AVHRR	1989-present	1 km	twice monthly
SPOT	Vegetation	1999-present	1 km	1-2 days
Envisat	MERIS	2002-present	300 m	1-3 days
Terra	MODIS	2000-present	250 m, 500 m, 1 km	1-2 days
Aqua	MODIS	2002-present	250 m, 500 m, 1 km	1-2 days

The chlorophyll in healthy vegetation absorbs the red segment of the electromagnetic spectrum for use in photosynthesis, but reflects highly in the green, and even more so in near-infrared segments, this disparity in reflectance is known as the *red edge* (Myneni *et al*., 1995). The sensors are sensitive to these wavelengths and a popular index was derived to exploit the differences in the red visible and near-infrared called the *normalized difference vegetation index* (NDVI) (Equation 1.1). The NDVI is often used as a proxy for vegetation cover since it is directly related to the overall density of healthy vegetation on the planet's surface (He *et al*., 2009; Jensen 2009). By creating a ratio between the red and near-infrared bands, much of the inherent signal variation due to calibration, noise, and atmospheric effects are minimized (Huete *et al*., 1999). However NDVI is limited by saturation in high biomass regions such as the tropics, the amount of

soil brightness, and is intrinsically nonlinear (Goward *et al*., 1991; Carlson and Ripley 1997; Huete *et al*., 2002). The NDVI was originally developed by Deering (1978) and is calculated as:

$$NDVI = \frac{(\rho_{nir} - \rho_{red})}{(\rho_{nir} + \rho_{red})} \qquad \text{(Equation 1.1)}$$

where ρ_{nir} is the corrected near infrared surface reflectance, ρ_{red} is the corrected red surface reflectance. The Enhanced Vegetation Index (EVI) was subsequently developed to improve on NDVI in the ability to separate bare soil from vegetation (Zhang *et al*., 2003). Klosterman *et al*. (2014) found the phenology dates derived from EVI to have smaller uncertainty than those derived from NDVI.

Schwartz (1999) states that the paper by Reed *et al*. (1994) should be credited with hastening the pursuit of phenology in the late 1990's. The paper itself discusses that a sharp increase in NDVI can be related to the onset of significant photosynthetic activity, or spring green-up. This was a major step in systematically identifying key phenological events using an automated quantitative approach. Schwartz (1997) and Schwartz and Reed (1999) worked to refine the observed timing between satellite derived *start of season* (SOS) and actual green-up on the ground. A fundamental problem described by Swartz (1997) and White *et al*. (1997) was how to accurately relate satellite observations to species-level phenological events: a necessary factor in describing the processes affecting SOS.

The launch of the Moderate Resolution Imaging Spectroradiometer (MODIS) in 1999 significantly augmented phenology research – and still remains the flagship sensor for this application today. It is mounted on two platforms in near polar, sun-synchronous orbit with two daily equatorial crossings each (Terra AM and Aqua PM, launched in 2002).

This high temporal resolution paired with moderate spatial resolution of 250 m is ideal for regional and global phenology assessments. MODIS provides a suite of high-quality vegetation products that undergo rigorous quality assessments before release (Huete *et al*., 2002). MODIS also provides a land surface temperature (LST) product which has been effective in modeling land surface phenology. For example, Zhang *et al.* (2004) merged MODIS NDVI with LST to observe growing season patterns and identified a poleward latitudinal movement in annual green up. LST is derived from emitted thermal infrared radiation and landcover specific emissivity values (Wan and Dozier 1996). A split window algorithm compares differential absorption rates between two thermal bands to effectively estimate the land surface skin temperature (Wan and Dozier 1996; Trigo *et al*., 2008). Validation of MODIS LST using in situ ground measurements has expressed a radiometric accuracy of ±1°C (Wan *et al*., 2002). However, a supplementary estimation technique is required to convert LST to surface air temperature (e.g. Mostovoy *et al*., 2006; Neteler 2010; Niclos *et al*., 2014).

An enduring remote sensing problem indirectly solved by MODIS is the issue of surface reflectance in the visible and infrared bands being absorbed by cloud cover. Imagery contaminated by clouds punctuates the time-series dataset, interrupting the phenological sequence. The solution is to group daily imagery into 8- and 16-day composites and average the clear NDVI or LST values at each pixel location (van Leeuwen *et al*., 1999). These temporal composites work to create a trending seasonal curve from which significant phenological metrics can be extracted (Schwartz and Reed 2002; Reed 2006; White *et al*., 2009). These metrics predominantly include SOS, maximum rate of green up, maximum NDVI, end of season, and length of growing season. These are

important indicators of phenological trends and shifts from climate change, but there is a pressing need to characterize successive stages within the continuous progression of plant development (Reed *et al*., 2009). However, the MODIS composite periods are too temporally coarse to distinguish short-lived phenological events of a single species (Coops *et al*., 2007; de Beurs and Henebry 2010).

Land surface phenology (LSP) is defined as the seasonal pattern of variation in vegetated land surfaces observed using remote sensing (White and Nemani 2006). The challenges of linking species-specific phenophases observed on the ground to satellite imagery are multifarious. The main obstacle being extrapolating observations at the level of individual plants across space and determining the scales at which this is possible (Badeck *et al.,* 2004). There is a lack of biome-scale ground-truth data that can be successfully compared with satellite measurements using a common scale (Fisher *et al*., 2006; Cleland *et al.,* 2007). Even where ground data exist, it is most likely point data at a single location, whereas the common resolution MODIS is 250 m (Misra *et al*., 2016). Improvements in comprehensive ground-level observations are being made through an emergent, intermediate-scale technique that uses ground-based time-lapse cameras to accurately detect fine-resolution vegetation development (Crimmins and Crimmins 2008; Bater *et al*., 2011). Described as 'near' remote sensing, inexpensive visible spectrum cameras are becoming widespread in phenological monitoring (Brown *et al*., 2016). A popular spectral index developed by Richardson *et al.* (2007) compares the green channel of a standard RGB image with radiance in the red and blue channels (Equation 1.2). This index is now commonly used for obtaining ground-based phenology metrics of forest

canopies (e.g. Richardson *et al*., 2009; Sonnentag *et al*., 2012) and individual plants (e.g. Nijland *et al*., 2013):

$$2\text{G-RBi} = 2\mu\text{G} - (\mu\text{R} + \mu\text{B}) \qquad \text{(Equation 1.2)}$$

where μR, μG, and μB are the image brightness values in the red, green, and blue channels, respectively. This index has been effective in estimating standard in situ seasonal metrics, such as SOS and senescence (e.g. Nagai *et al*., 2016), and extrapolating these signals to satellite imagery (e.g. Coops *et al*., 2012; Nijland *et al*., 2016). However, similar to seasonal curves from NDVI, the 2G-RB index remains too general to clearly and sequentially define each individual phenophase. Consequently, scaling the discrete ontogenetic stages of a single species to satellite imagery remains a significant research challenge.

1.3 Exploring the Controls of Phenology in Western Alberta

1.3.1 Rationale

Before undertaking a research program that seeks to develop a remote sensing framework for predicting phenological development in the understory, perhaps a more straightforward approach was available that had not yet been considered. It has been established that plant development is closely tied to temperature, and that seasonal climate is a dominant control of phenology in western Canada (Beaubien and Freeland 2000). Therefore, it was conceivable that understory phenology could be modeled directly from regional climate variables. Perhaps deploying a network of cameras and weather stations – something that ended up being central to this thesis research – would be unnecessary if the

regional phenology did not necessarily operate at the scale of a satellite image pixel. Or, if it did, seasonal climate may explain enough variability in phenology that the benefit of more extensive field analysis would be negligible. Regardless, a preliminary exploration of phenological controls in western Alberta was undertaken to provide a better understanding of how to effectively fill the knowledge gap.

Variability in temperature over western Canada is mainly attributed to broad-scale climate anomalies originating over the Pacific Ocean, chiefly the Pacific Decadal Oscillation (PDO) and the El Niño-Southern Oscillation (ENSO) (Redmond and Koch 1991; Shabbar and Khandekar 1996). These anomalies are initiated by changing patterns of ocean circulation, sea surface temperatures, and air surface pressures that are capable of modifying weather around the globe. The amplitude of these climate phenomena vary irregularly at interannual-to-inderdecadal time scales, either increasing or decreasing temperatures over Canada, depending on the phase of the oscillation (Mantua 1997). The temperature response in western Canada during a significant ENSO anomaly can be considerably large (~5°C) (Shabbar and Khandekar 1996). There have been a number of studies on coupled ocean-atmosphere indices altering the timing of phenological events (Beaubien and Freeland 2000; Cook *et al*., 2005; Ault *et al*., 2011; Li *et al*., 2012; McCabe 2012). These large-scale climate indices have been found to be useful predictors of ecological processes, even more so than local climate (Hallet *et al*., 2004). This is attributable to the persistence of anomalies and their atmospheric teleconnection lags that provide ample time to forecast phenological events elsewhere, and to resolve spatial patterns of plant development (McCabe 2012).

Again, most phenology research examines only a single life-cycle event, which is typically spring budburst because of its established importance as a bioindicator of climate change (Hänninien 1995; Linkosalo *et al*., 2008). This preliminary exploration looked to model the complete phenological progression from budburst to senescence, as it was initially not well known how to model ordinal phenophase events over time. Phenophases beyond budburst, such as *fruiting*, represent the timing of available nutrition and are therefore fundamental controllers of higher trophic levels (Power 1992). The focus-species of this study was Canada buffaloberry (*Shepherdia canadensis*), a widespread and critical food-source for many species living in the Rocky Mountains of Canada (Figure 1.1). It is a dioecious perennial shrub approximately 1.5 m tall, with oval 3-5 cm long dark green leaves, and 4-6 mm fruit. *Shepherdia canadensis* has distinct, easily observable phenophases with leaf budburst occurring in mid-May, flowering in late-May or early-June, and ripe fruit appearing in the latter part of July.

Figure 1.1 *Shepherdia canadensis* bearing ripe fruit.

1.3.2 Objectives

This preliminary inquiry had two objectives: first, to attempt to model the complete phenological sequence of *S. canadensis* along the central Rocky Mountains of Alberta, using large-scale climate indices as proxies for temperature. Second, to model the interannual variation of this sequence using these same climate proxies to predict the temporal lag (or advance) of phenological timing in *S. canadensis* year-to-year. The potential of using climate indices as proxies for at-site temperature would define patterns of phenology within the study area while significantly reducing field observation efforts.

1.3.3 Methods

The study area was a subset of the broader region mapped later in this thesis. It was located in west-central Alberta along the eastern slopes of the Rocky Mountains (Figure 1.2). Phenological observations of *S. canadensis* were made weekly by field personnel operating within a collaborating project – the Foothills Research Institute Grizzly Bear Program – from May until October for three years: 2008-2010.

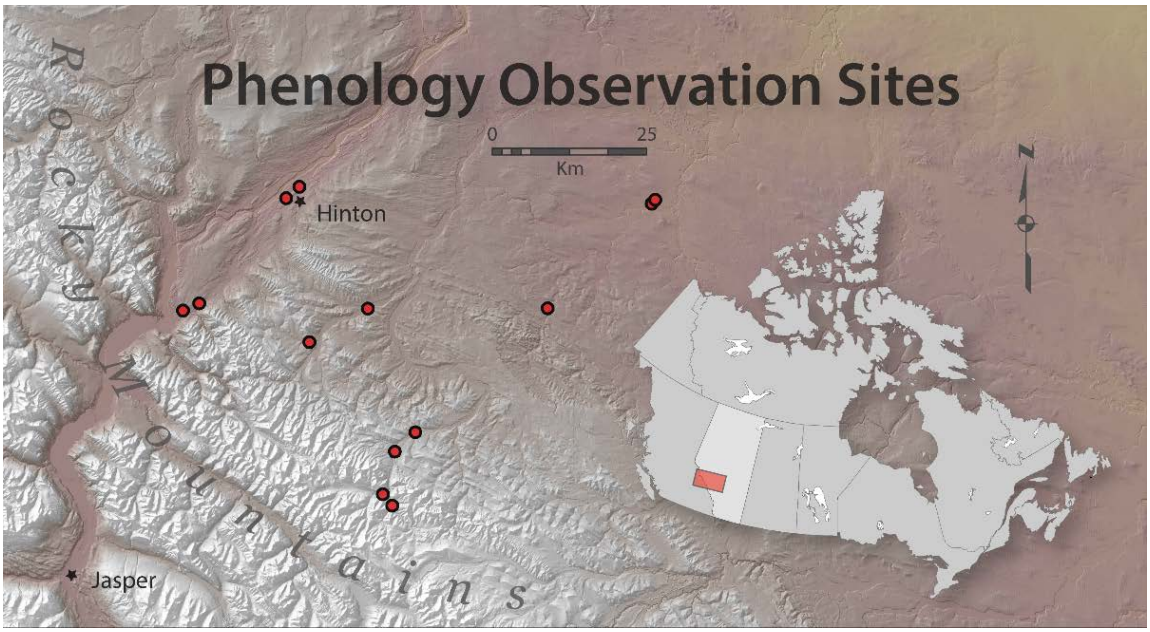

Figure 1.2 Study area and *Shepherdia canadensis* phenology observation sites.

Monthly multivariate El Niño Southern Oscillation index (MEI) and PDO index values were acquired from NOAA and the University of Washington's Joint Institute for the Study of Atmosphere and Oceans. These indices are used to synthesize complex sea-surface and atmospheric variables into a single summarized value (McCabe 2012). Both the MEI and PDO index are derived by extracting the leading, unrotated principle component of observed meteorological phenomena over the Pacific Ocean (Wolter and Timlin 1998; Mantua *et al*., 1997). The PDO index is calculated monthly, while the MEI is computed separately for each of twelve sliding bi-monthly seasons (i.e. Dec/Jan, Jan/Feb,...). Warm North American climate anomalies associated with the PDO are similar to those connected with El Niño (MEI) and La Niña, though generally not as extreme (Latif and Barnett 1994). Both the PDO index and the MEI have two phases: warm and cool, where index values are positive for warm phase conditions and negative for cool phase

conditions. During the study period, the PDO and El Niño Southern Oscillation were both in a cool phase which tends to exacerbate precipitation and temperature patterns over western Canada. While these oscillations affect broad-scale trends over the study area, higher frequency temperature-shifts are a result of the local micro climate typical of mountainous topography. It is for this reason medium-scale mean annual temperature (MAT) from 30-year climate normals (1960-1999) was used to account for local spatial variation primarily due to elevation differences.

Using STATA version 12.0 (StataCorp 2013) a logit transformation was applied to proportionally scale the ordinal phenophase values to between 0 and 1, this way a Generalized Liner Model (GLM) could be used (Equation 1.3). This particular model was chosen by virtue of the logistic curve's shape best-representing the sigmoid growth curve typical to plant development (Fisher *et al*., 2007). The vegetative (green leaf) developmental sequence is in fact a double sigmoid, whereby the growth curve in early spring is flat and static until budburst, and then rapidly progresses through phenophases as leaves unfold and fully develop in only a matter of weeks. The sequence plateaus again mid-summer, as there is no change in mature leaves until senescence. At this point leaves begin to yellow, and transition rapidly through the final phenophases until leaf abscission. Because no single model is capable of fitting a double sigmoid dataset, the vegetative sequence was split in two, modeled separately, and then stacked to represent the entire season. The first model encompassing early-season developmental phenophases (0-6) and the second including the late-season senescence phenophases (6-10) hereafter referred to as the *green-up* and *senescence* models respectively. Reproductive phenology transitions consistently across the growing season and was modeled as a single dataset. All model

datasets were declared as panel data because of repeated observations at each site, and *random effects* were employed to offset this bias.

$$y = a + b_1x_1 + b_2x_2 \ldots + b_nx_n \qquad \text{(Equation 1.3)}$$

A series of candidate models were assembled and ranked to estimate the complete phenological sequence of *S. canadensis* as a function of time (Julian day), and various combinations of average monthly PDO/MEI index values, MAT, non-linear factors, and interaction terms. Akaike's Information Criterion (AIC) was used to determine the best model (Wagenmakers *et al*., 2004). It was found that the two-month average index values during March and April consistently dominated the top-ranked models. A final series of candidate models was developed isolating these early-season values, with the *standard null* model simply being Julian date where phenological sequences should be explained by the day of the year without regard to site differences (MAT) or interannual variability due to climate proxies.

The range of climate-index values experienced during the study period was used to predict the resulting variability in phenological timing. Discrete daily probabilities of phenological timing were modeled given a particular early-spring index value. Variability of the models to changes in the PDO index, MEI or MAT could be observed as a lag or advancement in the developmental sequence. Throughout the three year study period, MEI index values in March and April varied from -1.3 to 1.13 and PDO varied from -1.62 to 0.61; MAT (30-year normal) across sites ranged from -1.9°C to 2.63°C. Model sensitivity was estimated by inserting these minimum-maximum and neutral index values.

Root mean squared error (RMSE) model validation was performed using phenological data collected in 2011 at 10 sites unique to the location where the 2008-2010 model training data was obtained. Model accuracy was tested by comparing model predictions of phenological timing in 2011, using MEI values for that year, with the actual 2011 in situ observations.

1.3.4 Results

The phenological progression of *S. canadensis* is largely explained by climate index values occurring in early spring at the beginning of the growing season. The most supported green-up model was explained by the interaction term of March/April MEI with Julian day. The same model was also ranked highest for senescence. The top reproductive model was largely explained by MAT (Table 1.2). The influence of climate indices was not as strong in predicting reproductive phenology as they were with the green-leaf vegetation. However, the interaction between Julian day and March/April PDO had a significant, inverse relationship on reproductive phenology – outperforming the null model. The quadratic term of Julian day had a much higher influence on the vegetative models than reproductive, suggesting very little non-linear effect on reproduction and more gradual development. The estimated model parameters are coefficients expressed in the units of each explanatory variable.

Table 1.2 Estimated model parameters for top-ranked AIC models of *Shepherdia canadensis* phenological timing. For Julian day (jday), the quadratic term of Julian day ($jday^2$), mean annual temperature (mat), the spring values of the multivariate El Niño index (mei_mar_apr), and the interaction term (*). Raw coefficients and Standard errors (in parentheses) are presented.

Phenology model	jday	$jday^2$	mat	mei_mar_apr	jday*mei_mar_apr
Vegetative Green-up	0.694 (0.043)	-0.002 (0.000)		6.916 (0.886)	-0.033 (0.005)
Vegetative Senescence	-0.505 (0.034)	0.001 (0.000)		-3.332 (0.740)	0.018 (0.003)
Reproductive	0.027 (0.015)	0.00007 (.00003)	0.891 (0.296)		

The green-up model had excellent predictive accuracy with an RMSE of only 3 days (Table 1.3). The senescence model performed poorly with an average error of 3 weeks, consistently predicting phenophases to occur much later in the season than observed. The reproductive model had an average RMSE of 14 days in prediction error, mostly overestimating the observed timing.

Table 1.3 Green-up, senescence, and reproductive model prediction RMSE validation showing phenophases with the best and worst prediction accuracy (in days).

Model	*RMSE*	Best Prediction	Worst Prediction
Green-up	3 days	Leaves fully unfolded (0)	Leaves 25% unfolded (-6)
Senescence	21 days	Over 50% yellow (+18)	Leaves beginning to fade (+28)
Reproduction	14 days	Bearing green fruit (-4)	Bearing overripe fruit (+38)

Interannual variability within the vegetative models saw an advance in green-leaf development across the entire season when MEI values were high (warm phase).

Alternatively, phenological development was delayed when this value dropped (Figure 1.3). Compared to an average year (MEI = 0), the maximum index value advanced the model by 12 days, while using the minimum value delayed development by 10 days. The maximum absolute difference in timing for *leaf out* was 22 days, and for *beginning to yellow* was nearly two weeks. For reproductive phenology there was a maximum delay of 39 days between average MAT and MAT at the coldest site (highest elevation). There was a two-week advance in flowering between average MAT and the site with the warmest MAT (lowest elevation). The maximum absolute variation between max and min in situ MAT values was 52 days (Figure 1.4) (phenophase definitions from Dierschke 1972).

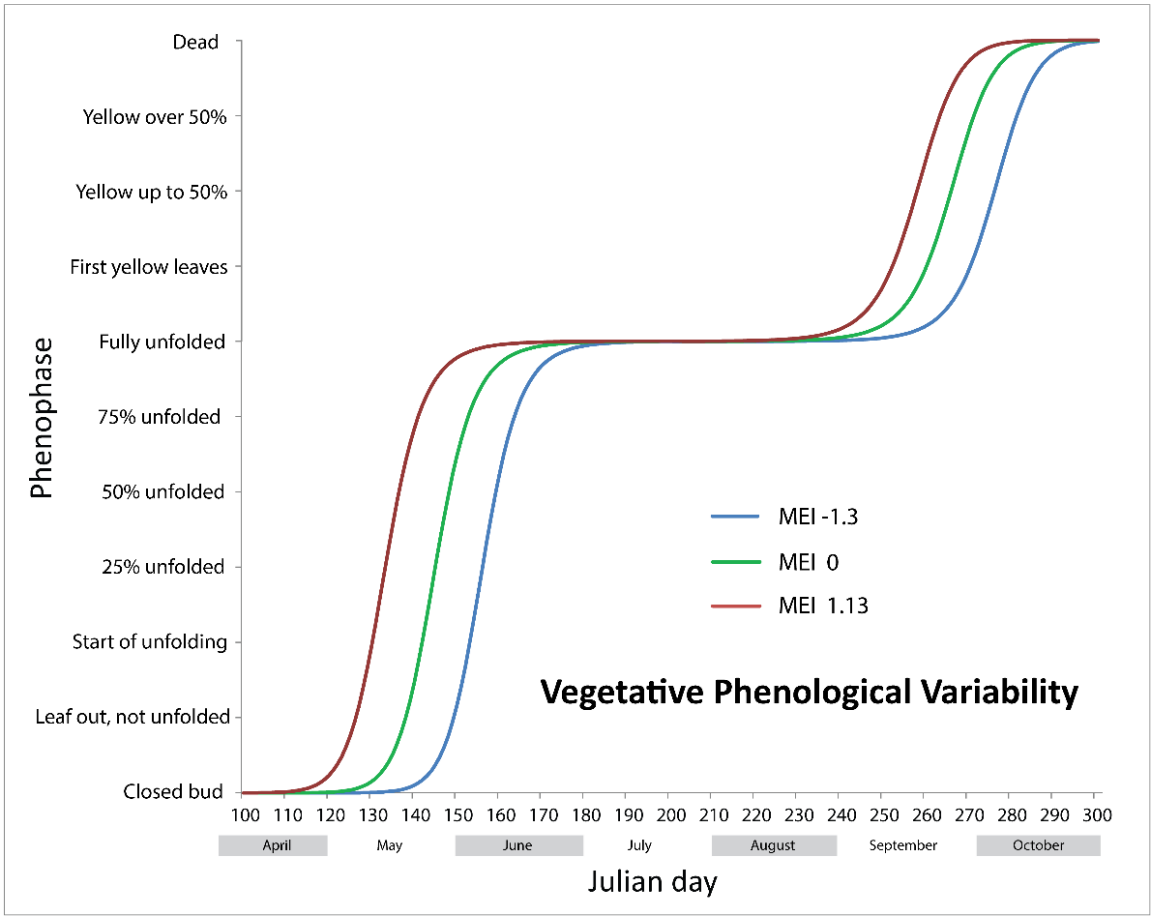

Figure 1.3 Green-up and senescence *Shepherdia canadensis* vegetative models predictions of interannual phenological variability based on the minimum, maximum, and neutral Multivariate El Niño Southern Oscillation Index (MEI) values occurring during the study period, 2008-2010.

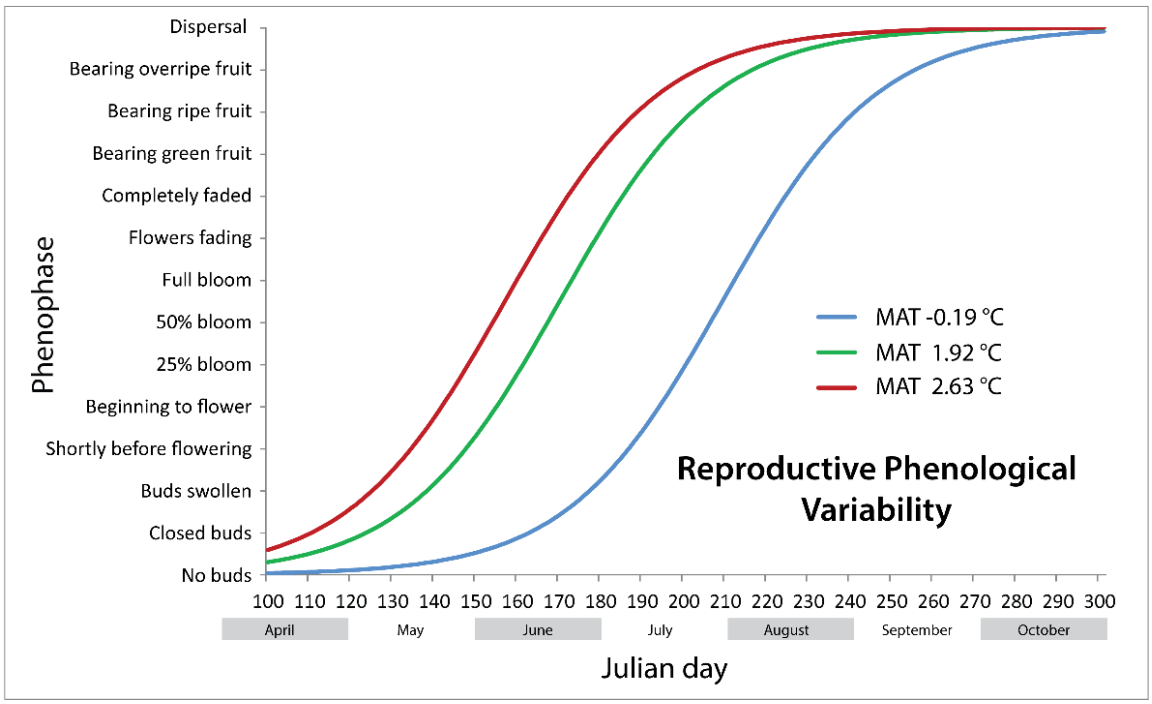

Figure 1.4 *Shepherdia canadensis* reproductive model predictions of interannual phenological variability based on the minimum, maximum and average mean average temperature (MAT) values occurring during the study period, 2008-2010.

1.3.5 Discussion and Conclusion

The complete phenological sequence of *S. canadensis* was successfully modeled and found to be controlled, to some extent, by the MEI. There was very good predictive accuracy of early season vegetative development until mid-August with an RMSE of three days. Although statistically significant, model predictions for reproductive phenology were much less accurate, with calculations of ripe berries occurring two weeks too late. Where green-leaf models incorporated the MEI climate proxy, variability of reproductive phenology was chiefly controlled by MAT. Julian day anchored all of the models by establishing the rate of progress through the growing season, with variation in interannual timing arising from changes in MEI or MAT. Uncertainty in the senescence model could

be partially due to these late season phenophases having long durations and gradual transitions, making them more difficult to pinpoint. Also, spring phenophases (leaf out) have been found to be more responsive to temperature change than those occurring later in summer/autumn (Chuine and Beaubien 2001; Pudas *et al*., 2008).

Interannual variability in MEI and MAT had large impacts on the timing of both vegetative and reproductive phenology respectively. Variability in MEI predicted a maximum variation in timing of 22 days for leaf out. Variation in MAT of nearly 3°C produced a shift in timing of over one month for the ripening of fruit. Unlike climate indices, the 30-year normal MAT is constant at each site, varying only across elevation making it a relatively poor predictor of interannual variability. The PDO index had no influence in the top models, this could simply be because it is uncorrelated, but more likely its effects are too weak or confounded by the more prominent MEI or the local climate. Despite the coarse predictions of reproductive phenology, there remains a significant correlation with MAT. This confirmed the physiological control of temperature on seasonal development and indicates that future models should include intensified observations of in situ temperature across the study area. Hourly temperature recordings would be more than sufficient to capture the variability required to base subsequent models (Schwartz 2003; Haggerty and Mazer 2008). It is believed that the models suffered from temporal gaps in the phenophase observation data. Using time-lapse cameras to increase the observation frequency should considerably improve model accuracy.

Through this preliminary inquiry it was determined that although climate proxies are a controlling factor in species phenology, the predictive capacity of the models is not sufficient for predictive mapping. The reproductive phenophases are exceedingly

important as they represent the availability of nutrition for the many foraging animals within the study area. Consequently, using a remote sensing approach to map discrete understory phenology events must overcome some significant research challenges. Firstly, it needs to be determined if an intensified observation effort using a network of cameras and weather stations will adequately detect fine-scale changes in phenology. Next, the relationship between MODIS LST and understory temperature needs to be established. In order to track daily phenology, a procedure is needed to contend with cloud contamination in the imagery time-series. Lastly, it is fundamental to assess if the thermal accumulation technique will adequately predict phenophases in the target species. The use of thermal imagery to map the discrete phenological stages of an understory species, from budburst to senescence, has not been done before.

1.4 Research Objectives

The overall goal of this thesis is to develop a remote sensing framework for monitoring distinct phenophases in understory vegetation and investigate the projected effects of climate change on developmental timing. The following research objectives were formulated to address the overall research goal:

1. Evaluate the level of agreement between multi-scale field observations and time-lapse camera imagery for identifying phenophases in understory species.
2. Establish if understory air temperature can be estimated using MODIS land surface temperature imagery.

3. Determine the high-resolution spatiotemporal patterns of understory phenology throughout western Alberta using understory air temperatures.
4. Explore the effects of experimental warming on phenophase timing and project how this shift will alter phenology patterns on the landscape.

1.5 Organization of the Thesis

The pursuit of these objectives are presented in four independent research articles that fit together into a unified body of work. Chapter 2 works to develop an effective methodological protocol for accurately observing phenology in the field using digital cameras (Objective 1). It builds off of the recommendations from the preceding climate-proxy inquiry to intensify and refine in situ measurements of temperature and phenology. It explores the effectiveness of using a time-lapse camera network in lieu of traditional observations made by personnel; including an investigation into the scale of phenological progression relative to the individual plant, the surrounding individuals, and satellite imagery pixels. The scaling of plot-level phenology to the broader landscape relies heavily on the concepts investigated in Chapter 2. Chapter 3 overcomes a major research hurdle in bridging the gap between canopy-top temperatures as seen by MODIS and those in the underlying understory (Objective 2). The forest characteristics and environmental variables which best-explain variability in understory temperature were also ascertained in this procedure. Chapter 4 develops a semi-automated methodology to effectively 'remove' cloud contamination in the daily MODIS LST imagery. Using the variables obtained in the previous chapter, the plot-level understory temperature estimates are extended across the study area to produce wall-to-wall maps of daily average understory temperature. These

maps were used to derive thermal accumulations to predict phenological development in the following chapter. Chapter 5 draws on all of the preceding chapters to develop the full theoretical and practical framework for mapping understory phenology (Objective 3). It also identifies the range of phenological variability anticipated under future warming scenarios (Objective 4). This variation is explored both spatio-temporally across the study area and experimentally in climate controlled growth chambers. Chapter 6 provides a summary of the conclusions, outlines the main research contributions, and offers considerations for future research.

Chapter Two: Evaluating the Level of Agreement Between Human and Time-Lapse Camera Observations of Understory Plant Phenology at Multiple Scales

2.1 Abstract

The growing popularity of digital-repeat photography in field research is seeing traditional field efforts being assisted and even replaced by low-cost cameras. The efficiency of using cameras is obvious, but there is an assumption that they capture the same information as observations made by humans. This paper aims to determine the level of agreement between these two methods of interpreting understory vegetation phenology. We compared daily phenological observations made by low-cost cameras with those made by personnel during field visits every 10 days. Phenophases were defined as the non-spectral, physical developmental stages of Canada buffaloberry (*Shepherdia canadensis*) and alpine sweetvetch (*Hedysarum alpinum*). The relationship between observation methods was quantified using a weighted kappa statistic at three spatial scales ranging from individual plants to areas up to 6 hectares. Agreement between the camera imagery and those made by field personnel was nearly perfect (Kappa > 0.9) for both the vegetative and reproductive phenology of both study species at all spatial scales. The level of agreement was found to be more variable early in the season when plant growth is more rapid. Overall there was a slight bias in the image interpretations to underestimate the rate of development. Time-lapse photography was found to be an analogous replacement for field visits; however, some plant species are more suitable for observation by camera than others. Spatially, it was determined that observations of a single plant are all that is required to capture the phenology of the surrounding region in excess of 6 hectares. This analysis

was carried out over a single growing season in the Rocky Mountains of western Alberta, Canada.

2.2 Introduction

A fundamental premise of scientific research is that repeated observations of natural phenomena can be used to identify patterns, trends, and changes over time and space (MacArthur 1972). Traditionally these observations have been obtained manually by individuals in the field. Over time, however, this effort has transitioned towards the use of automated digital sensors (Crimmins and Crimmins 2008). The benefit of this technology is primarily for the acquisition of consistent, high-quality datasets at substantially reduced costs and effort (Sonnentag 2012). For instance, digital-repeat photography has been broadly applied in ecosystem research, with a critical focus on vegetation phenology (Schwartz 2013, Inoue 2014): the study of the periodic life-cycle phases of plants which include leaf-out, flowering, and senescence (Badeck *et al*., 2004). Applications include observing rates of vegetation development as a bioindicator of climate change (Richardson *et al.*, 2009b, Nagai *et al.*, 2014), carbon flux calculations (Ide and Oguma 2010; Ahrends *et al.*, 2008), and species habitat assessment (Proulx and Parrott 2008, Bater *et al.*, 2011a, Coops *et al.*, 2012, Nijland *et al.*, 2013).

Imaging sensors capture vegetation phenology by either recording structural changes during leaf and flower development, or collecting the spectral information reflected by the plants as a measure of overall image ‘greenness’ (Richardson *et al.*, 2007). The latter method is the most common and is used to bridge phenological observations on the ground with satellite imagery to evaluate phenology at the ecosystem scale, also known

as *land-surface phenology* (Schwartz and Reed 1999, Beaubien and Hall-Beyer 2003, Richardson *et al.,* 2013). As a result, ground-level camera observations (near-surface remote sensing) are typically made of the forest canopy or the vegetated land cover which is directly observable by satellites (Inoue *et al.,* 2015). Beneath the canopy, near-surface remote sensing is less prevalent, though it is becoming increasingly important in a variety of applications. An improved understanding of the relationship between forest tiers provides further insight into monitoring vegetation spectral-dynamics via satellite (Miller *et al.,* 1997), differences in phenological timing (Richardson and O'Keefe 2009; Ryu *et al.,* 2014), ecosystem structure (Kudo *et al.,* 2008; Nijland *et al.,* 2014), and wildlife habitat quality (Tuanmu *et al.,* 2010; Bater *et al.,* 2011b). Assessments of habitat quality sometimes use phenology as a proxy for the amount of available nutrition on the landscape by relating a specific phenophase to forage quality, particularly when the appearance of a particular phenophase equates to a readily available food-source, such as fruit (Hebblewhite *et al.,* 2008; Nielsen *et al.,* 2010). This method of near-surface phenological monitoring requires direct visual inspections of plant-level phenology to validate camera imagery and to collect biomass samples for nutritional analysis (Coogan *et al.,* 2012; Nijland *et al.,* 2013).

For this study, the effort to observe understory vegetation phenology is motivated by our involvement in an ongoing grizzly bear (*Ursus arctos*) research program where we are working to monitor critical habitat for this species in Alberta, Canada (https://friresearch.ca/program/grizzly-bear-program). These animals strategically exploit a wide variety of understory plants that provide variable nutrition at differential times of the growing season (Nielsen *et al.,* 2003). Alpine sweet vetch (*Hedysarum alpinum*) is a

herbaceous legume with a nutrient-rich perennial taproot that offers quality forage preceding spring green-up, and after autumn senescence (Coogan *et al.,* 2012). Canada buffaloberry (*Shepherdia canadensis*) is a widespread diaceous shrub that fruits in late summer (Hamer and Herrero 1987). The ensuing objective of this research is to eventually scale the nutritional development of these plants from the plot level to a much larger region using satellite remote sensing. In general, extending localized understory phenological observations to the broader area is difficult for reasons that include environmental gradients and micro-climate, as they tend to alter phenology over space (Fisher *et al.,* 2006). Phenotypic and genetic variation can also alter the rate at which plant species respond to environmental cues (MacDonald and Chinnappa 1989, Richardson and O'Keefe 2009). As a result, spatially characterizing the phenology of a specific plant species in the forest understory is complex, and represents a significant research challenge (Tuanmu *et al.,* 2010).

Broad FOV cameras that acquire spectral indices such as NDVI and *greenness* do not directly observe the structural changes of individual plants. Studies examining the linkages between camera phenological metrics and the structural properties of vegetation remain elusive (Yang *et al.,* 2014). To our knowledge, attempts to extend the phenological observations of a single understory plant-camera pairings to the broader area is absent from the literature. The rapid adoption of repeat digital photography in ecosystem phenology research necessitates ongoing assessment of the limitations and utility of the imagery collected (e.g. Keenan *et al.,* 2014; Vartanian *et al.,* 2014). Despite their consistent and objective observations, cameras produce imagery that still requires field validation and post-hoc interpretation by human observers so as to extract meaningful data. There is a

need to compare interpretations of camera imagery with traditional direct field observations to ascertain how closely they agree. The manner and scale in which plant phenology is recorded with digital cameras can affect overall confidence in the dataset (Vartanian *et al.*, 2014).

The objective of this study was to evaluate the level of agreement between phenophase observations made in-person during field visits and those interpreted from imagery collected by digital cameras. Observations were made of the structural-physical changes in the vegetative (green-leaf) and reproductive phenology of *S. canadensis* and *H. alpinum*. The agreement between the two methods were compared across three spatial scales: 1) individual plants, or *plant-scale*, 2) plants occurring within a 10m radius plot, or *neighbourhood-scale*, and 3) plants occurring within a 250 m plot analogous to the ground resolution of a satellite sensor image pixel, or *pixel-scale*. We hypothesized that there would be no significant difference between the two phenological observation methods, though the relative merits of cameras (enhanced observation frequency; limited visual perspective) versus humans (unrestricted visual interpretation; limited revisit frequency) might lead to results that vary with scale. In all, 55 plants were observed daily using cameras, and nearly 4000 phenological observations were made by field personnel during weekly visits over a single growing season.

2.3 Methods

2.3.1 Study Area

The study area is located along the eastern slopes of the Rocky Mountains in Alberta, Canada (Figure 2.1). The landcover of this region is comprised of deciduous aspen

(*Populus tremuloides*), balsam poplar (*Populus balsamifera*), and white spruce (*Picea glauca*) mixed forests at lower elevations. The upper-foothills and mountains are dominated by mature lodgepole pine (*Pinus contorta*), Engelmann spruce (*Picea engelmannii*), and sub-alpine fir (*Abies lasiocarpa*) conifer forests.

A total of 37 observation plots were distributed over 650km along five elevational transects to obtain a variation of growing environments and temperature regimes (between latitudes 49.9° and 54.4°). Twenty three of these plots were *neighbourhood-scale* (10m radius or 0.0314ha) while the remaining 15 plots were *pixel-scale* (250 x 250 m or 6.25 ha). This ground coverage of pixel-scale plots relates specifically to the image pixel size of the Moderate Resolution Imaging Spectroradiometer (MODIS), which is a popular spaceborne platform for phenological observation of vegetation (Soudani *et al.,* 2008; Badeck *et al.*, 2004; Zhang *et al.,* 2003). The pixel-scale plots were comprised of a variety of spatially homogeneous forest stand-types (deciduous, coniferous, and mixed) with low local topographic complexity.

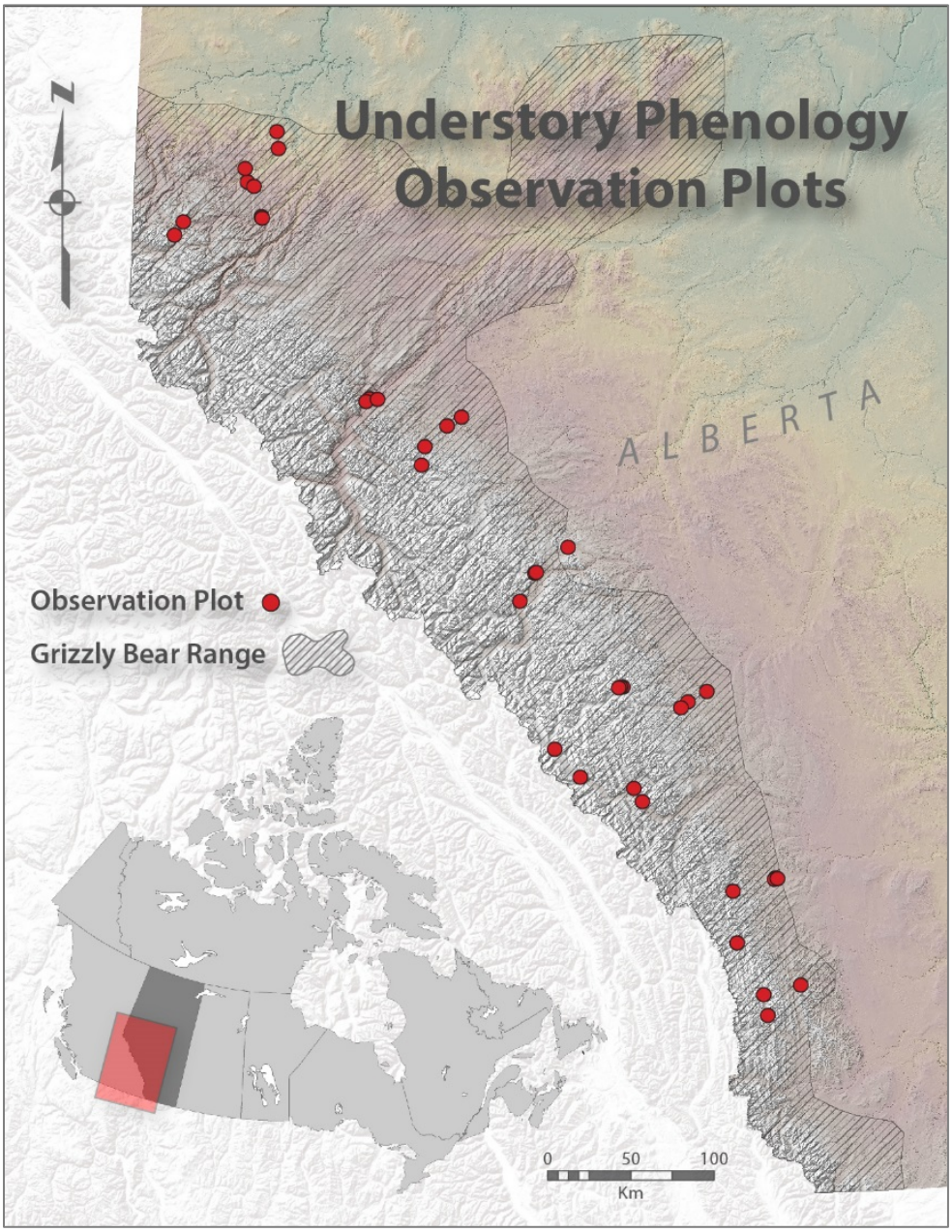

Figure 2.1 Study area extent and observation plot locations throughout the Rocky Mountains of western Alberta, Canada. Highest plot elevation: 1800 m, lowest: 800 m.

2.3.2 Camera Network Observations

A digital camera network of 55 Wingscapes PlantCams® (6MP) was distributed throughout the study area. Each unit incorporates a weatherproof casing which contains a

built-in intervalometer and lithium (AA) batteries that provided ample seasonal duration. 2560 x 1920 pixel resolution JPEG images (~1MB) were recorded to 4GB SD cards. Image compression through *lossy* formats such as JPEG could affect phenotyping accuracy, but this resolution is ample to discern the phenological changes in this study. It is also the most common image format for this type of observation (Minervini *et al.,* 2015). Phenophases of the focus species were defined by human interpreters observing the relative changes of images taken by individual cameras in a time series, so between-camera colour calibration was deemed unnecessary. Each plot contained at least one camera-plant pairing for each focus species with the cameras mounted north-facing on 1m steel monopods (Figure 2.2). The primary focus species of this study was on *S. canadensis* because of its visually distinct phenophases, widespread distribution, and critical nutritional importance. Therefore the majority of cameras were allocated to this species (n = 37). The remaining cameras were positioned to image *H. alpinum* (n = 18).

Figure 2.2 Mounting system and camera placement relative to *Shepherdia canadensis* (foreground) and *Hedysarum alpinum* (background).

With the emphasis of this study on structural phenology, camera placement was contingent on resolving the finest physical details of the focus species. For instance the flowers of *S. canadensis* are approximately 2 mm in size, therefore the distance between the camera and plant was variable to maximize both image resolution and FOV, usually between 30 cm to 1m. Each camera was set to record three images per day, one at solar noon, one an hour before, and one an hour after. This timing minimized directional effects from lighting, and provided image redundancy in case of inclement weather or cloud shadows. Observations were carried out from 23 April (Julian day 113) to 23 October (Julian day 296), 2011.

2.3.3 Field Observations

The plots were visited by trained staff at approximately 10-day intervals throughout the growing season, although this visitation rate was diminished in more-remote plot locations. Focus species were given *phenophase codes* based on the current stage of their vegetative and reproductive development (Table 2.1). These codes are based on those developed by Dierschke (1972), but modified to better suit the purposes of the study. For example ‘up to 50% yellow’ was changed to ‘50% yellow’ so a more temporally discrete phenophase-call could be made for a more effective comparison and analysis of observation agreement. The fruiting phenophase was broken into a subset of increments to glean the most temporal information about this critical nutritional stage. Phenophase codes vary in number and definition depending on the species type, in this study either woody plants (*S. canadensis*) or herbaceous forbs (*H. alpinum*). Personnel were equipped with ‘field guides’ containing

specific examples, descriptions, and imagery for each species to help reduce subjectivity and observer bias.

Table 2.1 Phenophase codes for woody (*Shepherdia canadensis*) and herbaceous (*Hedysarum alpinum*) plants, adapted from Dierschke (1972).

Shepherdia canadensis

VEGETATIVE PHENOPHASES	REPRODUCTIVE PHENOPHASES
0. Closed leaf bud	1. Flower buds recognizable
1. Leaf elongated	2. Flower buds strongly swollen
2. First leaf unfolded	3. Shortly before flowering
3. Leaves unfolded to 25%	4. Beginning to flower
4. Leaves unfolded to 50%	5. 25% flowers in bloom
5. Leaves unfolded to 75%	6. 50% flowers in bloom
6. Full leaf unfolding	7. Full bloom
7. First leaves turning yellow	8. Fading
8. 50% yellow	9. Completely faded
9. Completely yellow	10. Bearing green fruit
10. Abscission	11. First ripe fruit
	11.1 25% of fruit ripe
	11.2 50% of fruit ripe
	11.3 Completely ripe
	12. Bearing overripe fruit
	13. Dispersal

Hedysarum alpinum

VEGETATIVE PHENOPHASES	REPRODUCTIVE PHENOPHASES
0. Without shoots above ground	0. Without flower buds
1. Shoots without leaves	1. Flower buds recognizable
2. First leaf unfolded	2. Flower buds strongly swollen
3. Two or three leaves unfolded	3. Shortly before flowering
4. Plant fully developed	4. Beginning to flower
5. First leaves turning yellow	5. 25% flowers in bloom
6. 50% yellow	6. 50% flowers in bloom
7. Completely yellow	7. Full bloom
8. Abscission	8. Fading
	9. Bearing green seeds
	10. Bearing ripe seeds
	11. Bearing overripe seeds
	12. Dispersal

During field visits, observations were made at each individual plant-camera pair location (the *plant-scale*), and then a 10 m radius sweep was made around the camera to identify the phenophases of any focus species falling within that *neighbourhood*. Phenology at the *pixel-scale* was observed along two pre-established linear random transects bisecting each plot (500 m total) (Figure 3). The phenophase of any focus species encountered along the transect was recorded. Being a diaceous plant, only the reproductive phenology of female *S. canadensis* was observed, since there is differential blooming times between male and female plants (Johnson and Nielsen 2014).

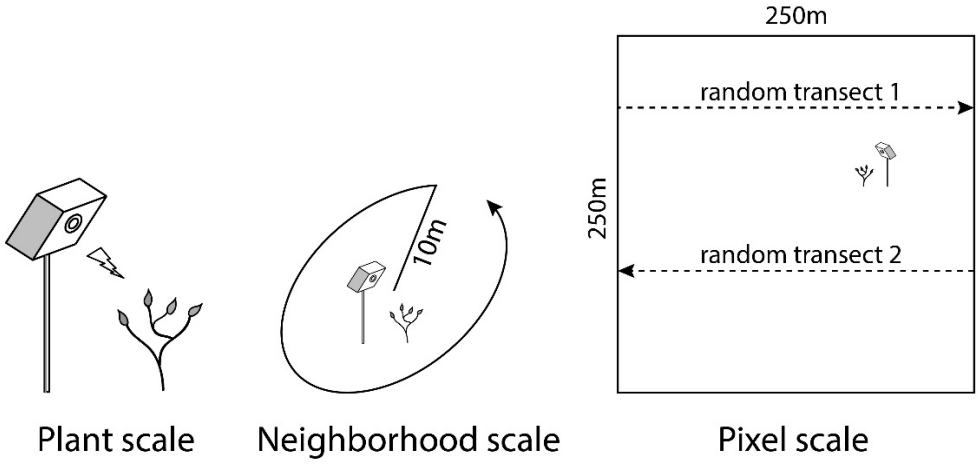

Figure 2.3 The three observation scales of vegetation phenology: Plant, Neighbourhood, and Pixel.

2.3.4 Photo Analysis and Statistics

Imagery was processed at the end of the season in Adobe Bridge CS6® using the same phenophase definitions used for the field observations. Photo interpretation was performed by the same individuals who carried out the field effort, but with no reference to the field

observation dataset. Each daily image was assigned a phenophase code based on the apparent stage of development.

We used error matrices (Congalton and Green 1999) to evaluate the level of agreement between the photo- and field-derived phenophase codes. The reference observations were those identified by observers in the field, to which the camera images were then matched via date. A weighted kappa statistic (Altman 1991) was calculated to evaluate the strength of agreement between the two observation methods (Equation 2.1).

$$w_i = \frac{i^2}{(k-1)^2} \qquad \text{(Equation 2.1)}$$

differing weights (w_i) are assigned to i phenological categories so that k number of categories can contribute varying levels of phenophase agreement to the kappa statistic. Additional matrices were produced to compare the camera observations to the neighbourhood-scale phenology, and then to the pixel-scale phenology by species. The mode was selected as the measure of central tendency to obtain a single phenophase code for aggregate observations of plants at these broader scales. A tie-breaker was used in the case of multimodal distributions, where the skewness of the phenophase distribution was used to indicate the prevailing stage of development. The *variation ratio* was calculated to determine phenological dispersion within the same species across the neighbourhood and pixel study plots at the same point in time (Equation 2.2). Where v is the variation ratio, f_m is the number of observations in the mode, and N is the total number of single species observations.

$$v = 1 - \frac{f_m}{N} \qquad \text{(Equation 2.2)}$$

The mode provides the majority phenophase within each plot, and the variation ratio conveys the proportion of observations that were not included in the mode. Higher variation ratios imply less confidence in estimations of broad-scale phenology during certain phenophases. Additionally, the *range* of phenophase codes observed per site visit was used to provide another measure dispersion. It is simply the difference between the largest and smallest codes recorded for a particular species in any given plot. The kappa statistics were compared between all three spatial scales to determine if the level of agreement between field observations and image interpretations varied significantly as the scale of observation increases using the following two-tailed Z-test statistic (Congalton and Green 1999) (Equation 2.3):

$$Z_{AB} = \frac{|k_A - k_B|}{\sqrt{var_{k_A} + var_{k_B}}} \qquad \text{(Equation 2.3)}$$

where Z_{AB} represents the standardized *z-score* derived from the kappa values of the two matrices being compared (k_A, k_B) and their variance (*var*) used in estimation of their respective confidence intervals. If there is no significant difference between the levels of agreement, this would suggest that observations from a single camera at the plant-scale are representative of phenology at the neighbourhood or pixel-scales.

2.4 Results

The high weighted kappa values suggest near-perfect agreement between the two observation methods. For both the vegetative and reproductive phenology of each focus

species and at all spatial scales the kappa statistic exceeded 0.9 (Table 2.2). A kappa of 1 would mean perfect agreement, while a value of zero implies the level of agreement is no better than chance (Landis and Koch 1977). We can conclude that agreement was significant in all cases ($p < .05$). The seasonal progression of distinct phenophases were clearly distinguishable in the imagery (Figure 2.4).

Figure 2.4 Examples of landmark phenophase images of *Hedysarum alpinum* (a) and *Shepherdia canadensis* (b).

Table 2.2 Level of agreement (weighted kappa) between phenological observations made through image interpretation and by field personnel and across three spatial scales.

PLANT-SCALE AGREEMENT

Species	Vegetative Phenophases					Reproductive Phenophases				
	Kappa	*Z*	*A.S.E.*	*p*	*n*	*Kappa*	*Z*	*A.S.E.*	*p*	*n*
S. canadensis	.942	14.97	.008	<0.01	252	.952	13.32	.009	<0.01	248
H. alpinum	.962	11.63	.008	<0.01	150	.980	10.10	.005	<0.01	137

Kappa statistic value (*Kappa)*, Z-value (*Z*), asymptotic standard error (*A.S.E.*), significance (*p*), and number of observations (*n*).

NEIGHBOURHOOD-SCALE AGREEMENT

Species	Vegetative Phenophases					Reproductive Phenophases				
	Kappa	*Z*	*A.S.E.*	*p*	*n*	*Kappa*	*Z*	*A.S.E.*	*p*	*n*
S. canadensis	.940	11.78	.011	<0.01	156	.919	10.02	.016	<0.01	153
H. alpinum	.940	7.55	.017	<0.01	67	.907	6.32	.028	<0.01	63

PIXEL-SCALE AGREEMENT

Species	Vegetative Phenophases					Reproductive Phenophases				
	Kappa	*Z*	*A.S.E.*	*p*	*n*	*Kappa*	*Z*	*A.S.E.*	*p*	*n*
S. canadensis	.924	8.372	.019	<0.01	82	.951	7.43	.022	<0.01	82
H. alpinum	.908	6.92	.027	<0.01	59	.977	6.35	.009	<0.01	51

The variation ratio consistently showed more phenological variability between individuals in the pixel plots than neighbourhood plots. *S. canadensis* had up to 50% more reproductive phenological variation and range between these two spatial scales (Table 2.3). Variability in phenophase observations remained consistent between spatial scales for *H. alpinum*, although the observed range in reproductive phenophases was relatively high. The vegetative phenophases with the highest phenological variability for both species across scales were the early stages of leaf development and latter stages of yellowing. The appearance of the first ripe berry of *S. canadensis* displayed the highest amount of spatial

variability, while *beginning to flower* and *completely ripe* had the lowest of all reproductive phenophases. The highest variability in *H. alpinum* were *fading* and the incremental stages of blooming, while the lowest was observed in *bearing overripe seeds* and *dispersal*. Higher observed range values tended to consistently correspond with higher rates of variation.

Table 2.3 Average variation ratio (variation) expressed as the percent (%) of non-mode observations, and average range of phenophases observed per site visit at the neighbourhood and pixel-scales.

Shepherdia canadensis								*Hedysarum alpinum*							
Vegetative Phenophases				Reproductive Phenophases				Vegetative Phenophases				Reproductive Phenophases			
variation		range		*variation*		range		*variation*		range		*variation*		range	
nbrhd	pixel	nbrhd	pixel	nbrhd	pixel	nbrhd	pixel	nbrhd	pixel	nbrhd	pixel	nbrhd	pixel	nbrhd	pixel
21%	28%	0.8	1.6	21%	40%	1.1	2.2	19%	21%	0.6	0.9	38%	36%	2.5	2.6

A comparison of observations from a single camera with those made across the neighbourhood and pixel-scales found no significant difference between them. The standardized Z-scores were all below 1.96 at a 95% confidence level (except reproductive phenophases of *H. alpinum* at the neighbourhood scale) (Table 2.4). We accepted the null hypothesis in this regard, that there is no difference between observations from a solitary camera and those made by staff across the larger plots. This result suggests that there would be no benefit in observing more than a single plant to approximate the phenology of an area up to 250 x 250 m (6.25 hectares).

Table 2.4 Comparison of the level of agreement between plant-scale camera observations in relation to phenological observations at the neighbourhood and pixel-scales.

Difference between plant-scale and neighbourhood-scale observer/image agreement				Difference between plant-scale and pixel-scale observer/image agreement			
S.canadensis Vegetative	*S.canadensis* Reproductive	*H. alpinum* Vegetative	*H. alpinum* Reproductive	*S.canadensis* Vegetative	*S.canadensis* Reproductive	*H. alpinum* Vegetative	*H. alpinum* Reproductive
$Z_{AB} = 0.148$ *p = 0.882*	$Z_{AB} = 1.84$ *p = 0.065*	$Z_{AB} = 1.19$ *p = 0.236*	$Z_{AB} = 2.54$ *p = 0.011*	$Z_{AB} = 0.852$ *p = 0.394*	$Z_{AB} = 0.042$ *p = 0.996*	$Z_{AB} = 1.93$ *p = 0.054*	$Z_{AB} = 0.301$ *p = 0.763*
Diff. = 0	*Diff.* = 0	*Diff.* = 0	*Diff.* ≠ 0	*Diff.* = 0	*Diff.* = 0	*Diff.* = 0	*Diff.* = 0

At the plant-scale, the biggest errors for the vegetative phenophases of *S. canadensis* were observed in the incremental stages of leaf unfolding, where a considerable proportion of image interpretations were called as *first leaf unfolded* (2) and *leaves unfolded to 25%* (3), while field observations were 3 and *Leaves unfolded to 50%* (4). This same underestimation occurred where observers recorded *starting to yellow* (7) but the camera interpreters still saw the leaves as completely green, *full leaf unfolded* (6). However, when field observers recorded *completely yellow* (9), the camera imagery was interpreted as dead (10). Similarly, the most disagreements in observing *H. alpinum* occurred during leaf development. Very early in the season, field staff identified *H. alpinum shoots above ground* (1) but the imagery did not (0). Later on some fully developed plants (as identified during field visits) were interpreted as *two or three leaves unfolded* in the camera imagery. There was also some confusion between completely yellow and dead. Overall there was very good agreement in detecting leaf emergence and abscission for both species.

For reproductive phenophases of *S. canadensis* there was no observable error bias. The biggest mismatch was *full bloom* being interpreted as *fading* or *completely faded* in the imagery. Overripe berries identified by field personnel were interpreted as *fully ripe* in

the imagery, but there is also error in the other direction where the imagery is calling overripe berries as dispersed. There was some confusion around fading in general with the cameras recording *completely faded*, while the phenophases were actually a blend of *full bloom*, *fading*, and *bearing green fruit*. For *H. alpinum* there was some late-season bias with the imagery underestimating the rate of the reproductive phenophases. *Completely faded* was labelled *faded*, and *bearing ripe seeds* was seen as *bearing green seeds* in the imagery, which is understandable given the similarities of these particular phenophases. Otherwise the reproductive observations of *H. alpinum* had minimal error and the highest overall level of agreement.

At the neighbourhood-scale, the slight bias seen in the vegetative phenophases persisted with development being underestimated in the imagery as compared to the plants in the vicinity of the cameras. This however was only noticeable in *S. canadensis* where *elongated leaves* were classified in the imagery, but observations of the neighbourhood saw that leaf-out was already underway. For *H. alpinum*, plant underdevelopment was observed through the cameras, but the neighbourhood was showing completely developed plants. This trend occurred less for the reproductive phenophases of *S. canadensis*, and the only disagreement arose during blooming, fading and protofruit development. This was similar for *H. alpinum* with some confusion between *full bloom* and *fading* and a late season bias in the imagery seeing earlier phenophases than what was occurring in the neighbourhood.

This early leaning trend of the camera observations was also apparent at the pixel-scale. The largest errors occurred during leaf development in *S. canadensis* where 2, 3, and 4 across the pixel were being identified as 1, 2 and 3 respectively in the imagery. This was

similar for *H. alpinum*, with the largest commission errors occurring between *two or three leaves unfolding* and *first leaf unfolded*. Interpretations of the reproductive phenophase imagery underestimated the rate of development of the pixel, particularly for fully ripe berries. There was no bias or specific reproductive phenophase errors at the pixel-scale for *H. alpinum*, although there was some minor confusion between *fading* and *completely faded*.

The structural logic of the error matrix is very binary, either observations matched or they did not, however a mismatch could have only been by a single day, or it may have been off by twenty. Identifying the exact amount of temporal error provides an additional degree of inference into which phenophases are more difficult to observe. These errors were calculated to examine the degree of agreement mismatch not evident in the matrices (Table 2.5). The majority of mismatches were within just one or two days. The lowest overall was the reproductive phenology of both *S. canadensis* and *H. alpinum*, with only 1.5 days average mismatch between observations. The highest overall was for the vegetative phenophases of *S. canadensis* at 3.7 days average mismatch. Reproductively, the blooming and fading phenophases of *S. canadensis* had the highest temporal mismatch of roughly 4 days, however beginning to bloom and fully ripe had some of the lowest error. The reproductive phenophases of *H. alpinum* were consistently low except some increasing mismatch in observations during the seed bearing.

Table 2.5 Average mismatch (in days) of field observations vs. camera observations at the plant-scale. Negative values denote camera interpretations occurring earlier than the corresponding field observation, and positive values later (refer to Table 2.1 for phenophase code names).

Vegetative Phenophases				Reproductive Phenophases			
S. canadensis		*H. alpinum*		*S. canadensis*		*H. alpinum*	
phen.	*ε*	*phen.*	*ε*	*phen.*	*ε*	*phen.*	*ε*
0.	–	0.	0.0	1.	0.0	0.	0.2
1.	-1.2	1.	-0.6	2.	–	1.	-0.3
2.	-1.6	2.	-0.8	3.	–	2.	-0.3
3.	-3.4	3.	-2.3	4.	-0.5	3.	0.5
4.	-5.5	4.	-1.6	5.	-1.5	4.	1.8
5.	4.3	5.	-2.1	6.	-4.0	5.	1.7
6.	-0.7	6.	-2.5	7.	4.6	6.	-1.0
7.	-6.0	7.	-3.5	8.	4.2	7.	-1.3
8.	-7.5	8.	0.0	9.	-1.4	8.	0.8
9.	6.6			10.	-1.3	9.	-3.0
10.	0.0			11.	-1.3	10.	-2.8
				11.1	-3.3	11.	-4.5
	$\lvert\bar{x}\rvert$		$\lvert\bar{x}\rvert$	11.2	3.5	12.	-0.7
	3.7d		1.5d	11.3	0.5		
				12	-3.2		
				13	-2.3		
					$\lvert\bar{x}\rvert$		$\lvert\bar{x}\rvert$
					2.3d		1.5d

Phenophase (*phen*), temporal error (ε) in days, absolute value of average error in days ($\lvert\bar{x}\rvert$).

The underestimation bias of the imagery is also apparent in the temporal errors – with the imagery consistently recording phenophases beginning a few days later than what is being recorded by field personnel. For example, when the cameras capture the first ripe fruit of *S. canadensis*, this phenophase as observed by personnel actually began about a day earlier.

2.5 Discussion

Agreement between the two observation methods was very good, however phenophases with shorter durations had slightly reduced levels of agreement. This is largely an effect of having regularly scheduled site visits at much broader temporal intervals than the rate of image capture. The cameras catch all stages of development by making daily observations, but some phenophases are so brief they are only observed once or missed completely between weekly visits by field staff. The highest agreement consistently occurred during *full leaf unfolded* and *bearing green fruit* which are the phenophases that have the longest durations and consequently encompass the most site visits. Conversely, the lowest agreement was amongst the rapid transitional phenophases that take place early in the season such as the incremental stages of leaf unfolding and flower blooming. The level of agreement varies between species simply due to the number of phenophase definitions they have. Herbaceous plants such a *H. alpinum* have a reduced number of phenophases while woody shrubs have more, which are in turn more difficult to pinpoint with the same number of field observations (Figure 2.5).

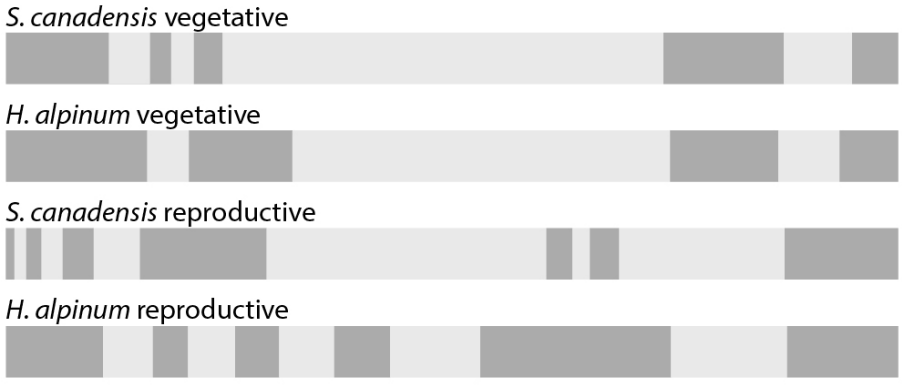

Figure 2.5 Relative average phenophase durations of the focus species highlighting the increased temporal brevity of both the early-season and reproductive phenophases.

In addition to visitation schedule incongruences, plant development during shorter phenophases tends to be more dynamic and blur the physical structures used to identify them. This requires more objective effort and interpretation skill from for both field observers and image analysts. Isolating phenophase transitions is further exacerbated by phenotypic variability between individuals (Villellas *et al.,* 2014), especially when observing a number of plants at the broader spatial scales. This variability is more pronounced during the shorter phenophases, since it would otherwise average-out over longer periods and over more field observations. Spatially, this increased variability was exhibited in the higher variation ratios and range values across spatial scales. Variable phenological expression between individuals is inevitable, and is more a concern when extrapolating observations from a single camera to the surrounding area. The main uncertainties in this study arose not so much from increasing the spatial extent, but more a result of the varying temporal duration of phenophases. Trust in observations during periods of rapid development should be circumspect, and ought to be offset by temporarily increasing site visits or expanding the camera network to capture spatial variability.

Confidence in observations from a single plant to postulate about the phenology of the broader region ultimately relies on the size of the area being generalized, the homogeneity of the landscape, and the species being observed. For this study, there was no reduction in the level of agreement as spatial scale increased up to an area covering just over 6ha. This suggests that uniform phenological rates could potentially extend to substantially broader regions if land cover and elevation remained uniform. Increased landscape complexity would introduce topographic effects that would begin to alter the microclimate and light intensity (Keenan *et al.,* 2014; Coogan *et al.,* 2012; Fisher *et al.,*

2006). This 6ha spatial coverage is similar to forest canopy observations from tower-mounted cameras (Richardson *et al.,* 2007, 2009a). However, broad FOV spectral camera observations in the understory are unattainable as they obscured by the understory itself. For this reason inferring about the broader understory phenology using observations of a single camera may be a suitable alternative to modeling land surface phenology, and certainly warrants expanded research.

The persistent developmental underestimation bias from the imagery is likely a result of the limited camera FOV. In the bulk of observations the imagery missed the transition to the next phenophase by two days on average. As an example, consider the first berry to ripen on *S. canadensis*, this particular berry is easily spotted by field crews but could be on the other side of the plant out of view of the camera. The imagery is still identifying the phenophase as *bearing green fruit* and will do so until a ripe berry appears within the FOV – in reality the plant has already transitioned to the next phenophase days earlier. With the intention of maximizing image resolution for observing minute changes in plant structure, cameras were placed 30cm to 1m from the study species. For *S. canadensis* this FOV encompasses only a portion of the plant, one complete side as a maximum, and perhaps the majority of *H. alpinum's* long areal stems, but not every developing part of the plant as seen by human observers. Image resolution could also contribute to underestimating development (Minervini *et al.*, 2015), an example being berries identified as *overripe* in the field, but are still seen as *fully ripe* in the imagery. Inadequate resolution (or focus) may make subtle discoloration or wrinkling in fruit undetectable in the imagery until they become more pronounced. This would be similar with fading flowers, where early signs of petal desiccation are difficult to detect in person,

let alone the imagery. One situation where bias may not be a result of the cameras was *H. alpinum* being identified during field visits as *fully developed*, but seen only as *two or three leaves unfolded* in the imagery. This would be a result of subjective observer bias, but the overall consistency of the directional trend in phenophase agreement points towards a bias of the mechanical setup of the cameras. Moving toward a wider FOV, while maintaining high image resolution, or using two cameras per plant to resolve a 360° view of the plant would work to offset the underestimation issue. This is not a problem in broad-FOV observations of land surface phenology or spectral averages (e.g. Vartanian *et al.*, 2014), but is unavoidable when observing structural phenology using individual plant-camera pairings.

An alternate explanation of the consistent underestimation bias may be due in part to the specific terminology used in the phenophase definitions for this study. Many of the decision-rules stated that the *majority* of leaves, flowers, or fruit had to be sufficiently developed to 'officially' transition to the next phenophase. Use of the term *majority* seemed a logical rule at the outset, but what is considered majority in the imagery is only a sample of the entire plant that field observers are using to interpret phenophases. Care should be taken in creating project-specific phenophase definitions and they should be specialized for making observations using cameras. The phenophase definitions for this project were derived from Dierschke (1972) and have been used in numerous studies (e.g. Bater *et al.*, 2011a, 2011b; Nijland *et al.*, 2013). Widespread nomenclature and semantics are essential to establish meaningful comparisons between studies. It should be taken into consideration however that the original phenophase definitions by Dierschke were developed for field observations made by humans and not for image interpretation. Given the variety of plant

species and camera systems used to observe them, it is suggested that the definitions are appropriately adapted accommodate the specifics of each study to increase observer-camera agreement. Simply having a different number of phenophase codes between forbs and woody plants was enough to alter the level of agreement in this study. Therefore, unless the definitions are modified, the highest observation agreement may always occur in species with fewer phenophases. Furthermore, the unmodified original phenophase definitions could happen simultaneously in this study, or not at all, depending on the species. *Flower buds strongly swollen* was very hard to identify in *S. canadensis*, because it was followed by *shortly before flowering* and the two were completely indistinguishable or undetected by the cameras. *Bearing overripe fruit* and *dispersal* could often occur simultaneously or not at all if animal predation occurs soon after ripening. In addition, although dispersal is triggered by the physiology of that particular individual during senescence, a strong wind could be what truly defines the end of this phenophase. In hindsight, these phenophase definitions were either too confounding, non-existent, or arbitrary to have been included in the study.

The reproductive stages of *H. alpinum* were very challenging to interpret, since up to five phenophases could occur at a single point in time. This species has a long stem along which are regularly spaced embryonic buds that begin maturation from the proximal to the distal end of the stem. There were many cases where *blooming* and *going to seed* were occurring simultaneously – observer objectivity and phenophase definitions were critical for consistency in these situations. In this specific example, the ‘majority’ rule helped with interpretation, but making reproductive phenophase classifications of this species was never straightforward and ultimately lessened the level of agreement between

observation methods. This was evident in the high range and variation ratios of these phenophases in the broad spatial plots, and more likely due to interpretive inconsistency in the field rather than actual variability in development. Phenophase definitions assist field personnel and image interpreters in making objective and consistent phenophase observations. Weather these are using the traditional nomenclature or project-specific definitions, adherence to these demarcations are essential in reducing error and improving agreement.

It is assumed that human-interpretation bias contributed a significant amount of agreement mismatch between field observations and interpretations of the camera imagery. Unfortunately it is difficult to assess the exact amount of human error in this type of classification (Congalton and Green 1999). Observational error was minimized by creating a clear visual guide with concise phenological definitions and using well-trained field personnel and image interpreters. Despite these efforts, some species are simply not well-suited for phenological observation using cameras. For example, cow parsnip (*Heracleum lanatum*) is a large leafy herb that can reach a height of 2m. It was found that *H. lanatum* grew too fast to remain in the camera FOV, and unless different equipment was used, this particular species was not suitable for camera observations without increasing site visits to constantly adjust the FOV – which essentially nullifies the convenience of using cameras. To maximize reliance on digital repeat photography, the combination of camera resolution, FOV, focus species, and phenophase definitions should all be considered carefully before commencing observations.

The overarching challenge of all phenological observations is attempting to classify continuous natural lifecycle events into discrete categories. Although each stage is

identifiably unique, to choose a temporally explicit threshold to end one phenophase and begin the next has to be, to some extent, arbitrary. Transition rates differ between phenophases, some have more distinct boundaries, others less so, which creates a challenge regardless of observation method. The benefits of repeat digital photography over laborious and costly site visits is evident. However, considering the findings of this study, there are challenges and advantages of both methods for observing understory phenology. The pros and cons of several phenology monitoring methods were described by Richardson *et al.*, (2013). Table 2.6 expands on that comparison to specifically address observing structural phenology of understory plants.

Table 2.6 Advantages and disadvantages of digital repeat photography for assessment of structural phenophases in the understory.

Advantages	***Disadvantages***
• Cameras capture daily images	• Interpretive consistency and objectivity is essential
• Low effort	• May underestimates plant development
• Obtain start date and duration of each phenophase	• Image FOV and resolution may confound interpretation
• Relatively low cost compared to using field staff	• Camera failure or animal interference may create large data gaps
• Observation of individuals may represent larger area, dependent on landscape complexity	• Phenophase definitions vary with plant types
	• Some plants are not well-suited for observation by camera

2.6 Conclusion

This study observed the physically developing structures of plants as a means of recording phenology in the understory. It worked to determine the level of agreement between phenological observations made by humans and those interpreted from time-lapse camera imagery. Agreement between the methods was very high, but there was a slight persistent underestimation of development as seen through the cameras, potentially a result of limited image FOV. Furthermore, it was found that the level of agreement was reduced when phenophase durations are brief and that confidence in the cameras should be variable at different times of the growing season depending on rate of plant development. These findings suggest that digital cameras are nearly identical as human observers, but are not faultless. Consistent and objective observations by field staff and image interpreters were the best means to control bias. It was also discovered that there was a significant spatial trend between the phenology of a single plant and others in the surrounding area up to 6 hectares. There is potential for further investigation into the range at which phenological correlations between individuals dissipate. Inexpensive digital cameras are proving invaluable for efficiently collecting consistent and reliable field observations. However, a large amount of effort is still required for post-hoc image interpretation and extracting the desired image information. With concurrent developments in computer-vision there is enormous potential for attaining completely autonomous phenophase detection. Combinations of spectral and textural feature extraction are proving to be a reliable and robust means of increasing image analysis throughput in a variety of conditions (e.g. Story and Kacira 2015; Chowdhury *et al.*, 2015). It would be compelling to examine the agreement between human image interpretations and those made through autonomous

computer-vision. The future of near-surface remote sensing for ecosystem monitoring is likely to employ such technology. In the meantime, digital repeat photography continues to be a significant benefit for phenology research, species habitat assessment and a broad variety of other applications.

2.7 References

Ahrends, H. E., Brugger, R., Stockli, R., Schenk, J., Michna, P., Jeanneret, F., . . . Eugster, W. (2008). Quantitative phenological observations of a mixed beech forest in northern Switzerland with digital photography. *Journal of Geophysical Research-Biogeosciences, 113*(G4).

Altman, D. G. (1991). *Practical statistics for medical research*: CRC press.

Badeck, F.-W., Bondeau, A., Bottcher, K., Doktor, D., Lucht, W., Schaber, J., & Sitch, S. (2004). Responses of spring phenology to climate change. *New Phytologist, 162*(2), 295-309.

Bater, C. W., Coops, N. C., Wulder, M. A., Hilker, T., Nielsen, S. E., McDermid, G., & Stenhouse, G. B. (2011b). Using digital time-lapse cameras to monitor species-specific understorey and overstorey phenology in support of wildlife habitat assessment. *Environmental Monitoring and Assessment, 180*(1-4), 1-13.

Bater, C. W., Coops, N. C., Wulder, M. A., Nielsen, S. E., McDermid, G., & Stenhouse, G. B. (2011a). Design and installation of a camera network across an elevation gradient for habitat assessment. *Instrumentation Science & Technology, 39*(3), 231-247.

Beaubien, E. G., & Hall-Beyer, M. (2003). Plant phenology in western Canada: Trends and links to the view fromspace. *Environmental Monitoring and Assessment, 88*(1-3), 419-429.

Chowdhury, S., Verma, B., & Stockwell, D. (2015). A novel texture feature based multiple classifier technique for roadside vegetation classification. *Expert Systems with Applications, 42*(12), 5047-5055.

Congalton, R. G. & Green, K. (1999). Assessing the accuracy of remotely sensed data: principles and practices. Boca Raton: CRC Press/Taylor & Francis.

Coogan, S. C. P., Nielsen, S. E., & Stenhouse, G. B. (2012). Spatial and temporal heterogeneity creates a brown tide in root phenology and nutrition. *ISRN Ecology, 2012*, 10.

Coops, N. C., Hilker, T., Bater, C. W., Wulder, M. A., Nielsen, S. E., McDermid, G., & Stenhouse, G. (2012). Linking ground-based to satellite-derived phenological metrics in support of habitat assessment. *Remote Sensing Letters, 3*(3), 191-200.

Crimmins, M. A., & Crimmins, T. M. (2008). Monitoring plant phenology using digital repeat photography. *Environmental Management, 41*(6), 949-958.

Diershke, H. (1972). On the recording and presentation of phenological phenomena in plant communities. No. Folleto 3629.

Fisher, J. I., Mustard, J. F., & Vadeboncoeur, M. A. (2006). Green leaf phenology at Landsat resolution: Scaling from the field to the satellite. *Remote Sensing of Environment, 100*(2), 265-279.

Hamer, D., & Herrero, S. (1987). Grizzly bear food and habitat in the front ranges of Banff National Park, Alberta. *Bears: their biology and management*, 199-213.

Hebblewhite, M., Merrill, E., & McDermid, G. (2008). A multi-scale test of the forage maturation hypothesis in a partially migratory ungulate population. *Ecological Monographs, 78*(2), 141-166.

Ide, R., & Oguma, H. (2010). Use of digital cameras for phenological observations. *Ecological Informatics, 5*(5), 339-347.

Inoue, T., Nagai, S., Kobayashi, H., & Koizumi, H. (2015). Utilization of ground-based digital photography for the evaluation of seasonal changes in the aboveground green biomass and foliage phenology in a grassland ecosystem. *Ecological Informatics, 25*(0), 1-9.

Inoue, T., Nagai, S., Saitoh, T. M., Muraoka, H., Nasahara, K. N., & Koizumi, H. (2014). Detection of the different characteristics of year-to-year variation in foliage phenology among deciduous broad-leaved tree species by using daily continuous canopy surface images. *Ecological Informatics, 22*(0), 58-68.

Johnson, K. M., & Nielsen, S. E. (2014). Demographic effects on fruit set in the dioecious shrub Canada buffaloberry (Shepherdia canadensis). *PeerJ, 2*, e526.

Keenan, T. F., Darby, B., Felts, E., Sonnentag, O., Friedl, M. A., Hufkens, K., . . . Richardson, A. D. (2014). Tracking forest phenology and seasonal physiology using digital repeat photography: a critical assessment. *Ecological Applications, 24*(6), 1478-1489.

Kudo, G., Ida, T. Y., & Tani, T. (2008). Linkages between phenology, pollination, photosynthesis, and reproduction in deciduous forest understory plants. *Ecology, 89*(2), 321-331.

Landis, J. R., & Koch, G. G. (1977). An application of hierarchical kappa-type statistics in the assessment of majority agreement among multiple observers. *Biometrics*, 363-374.

MacArthur, R. H. (1972). Geographical ecology: patterns in the distribution of species: Princeton University Press.

Macdonald, S. E., & Chinnappa, C. C. (1989). Population differentiation for phenotypic plasticity in the stellaria-longipes complex. *American Journal of Botany, 76*(11), 1627-1637.

Miller, J. R., White, H. P., Chen, J. M., Peddle, D. R., McDermid, G., Fournier, R. A., . . . LeDrew, E. (1997). Seasonal change in understory reflectance of boreal forests and influence on canopy vegetation indices. *Journal of Geophysical Research-Atmospheres, 102*(D24), 29475-29482.

Minervini, M., Scharr, H., & Tsaftaris, S. A. (2015). The significance of image compression in plant phenotyping applications. *Functional Plant Biology, 42*(10), 971-988.

Nagai, S., Yoshitake, S., Inoue, T., Suzuki, R., Muraoka, H., Nasahara, K. N., & Saitoh, T. M. (2014). Year-to-year blooming phenology observation using time-lapse digital camera images. *Journal of Agricultural Meteorology, 70*(3), 163-170.

Nielsen, S. E., Boyce, M. S., Stenhouse, G. B., & Munro, R. H. M. (2003). Development and testing of phenologically driven grizzly bear habitat models. *Ecoscience, 10*(1), 1-10.

Nielsen, S. E., McDermid, G., Stenhouse, G. B., & Boyce, M. S. (2010). Dynamic wildlife habitat models: Seasonal foods and mortality risk predict occupancy-abundance and habitat selection in grizzly bears. *Biological Conservation, 143*(7), 1623-1634.

Nijland, W., Coops, N. C., Coogan, S. C. P., Bater, C. W., Wulder, M. A., Nielsen, S. E., . . . Stenhouse, G. B. (2013). Vegetation phenology can be captured with digital repeat photography and linked to variability of root nutrition in Hedysarum alpinum. *Applied Vegetation Science, 16*(2), 317-324.

Nijland, W., Nielsen, S. E., Coops, N. C., Wulder, M. A., & Stenhouse, G. B. (2014). Fine-spatial scale predictions of understory species using climate- and LiDAR-derived terrain and canopy metrics. *Journal of Applied Remote Sensing, 8*.

Proulx, R., & Parrott, L. (2008). Measures of structural complexity in digital images for monitoring the ecological signature of an old-growth forest ecosystem. *Ecological Indicators, 8*(3), 270-284.

Richardson, A., & O'Keefe, J. (2009). Phenological differences between understory and overstory. In A. Noormets (Ed.), *Phenology of Ecosystem Processes* (pp. 87-117): Springer New York.

Richardson, A. D., Braswell, B. H., Hollinger, D. Y., Jenkins, J. P., & Ollinger, S. V. (2009b). Near-surface remote sensing of spatial and temporal variation in canopy phenology. *Ecological Applications, 19*(6), 1417-1428.

Richardson, A. D., Hollinger, D. Y., Dail, D. B., Lee, J. T., Munger, J. W., & O'Keefe, J. (2009a). Influence of spring phenology on seasonal and annual carbon balance in two contrasting New England forests. *Tree Physiology, 29*(3), 321-331.

Richardson, A. D., Jenkins, J. P., Braswell, B. H., Hollinger, D. Y., Ollinger, S. V., & Smith, M. L. (2007). Use of digital webcam images to track spring green-up in a deciduous broadleaf forest. *Oecologia, 152*(2), 323-334.

Richardson, A. D., Keenan, T. F., Migliavacca, M., Ryu, Y., Sonnentag, O., & Toomey, M. (2013). Climate change, phenology, and phenological control of vegetation feedbacks to the climate system. *Agricultural and Forest Meteorology, 169*, 156-173.

Ryu, Y., Lee, G., Jeon, S., Song, Y., & Kimm, H. (2014). Monitoring multi-layer canopy spring phenology of temperate deciduous and evergreen forests using low-cost spectral sensors. *Remote Sensing of Environment, 149*(0), 227-238.

Schwartz, M. D. (2013). Phenology: An Integrative Environmental Science. 2nd Edition. Springer, New York.

Schwartz, M. D., & Reed, B. C. (1999). Surface phenology and satellite sensor-derived onset of greenness: an initial comparison. *International Journal of Remote Sensing, 20*(17), 3451-3457.

Sonnentag, O., Hufkens, K., Teshera-Sterne, C., Young, A. M., Friedl, M., Braswell, B. H., . . . Richardson, A. D. (2012). Digital repeat photography for phenological research in forest ecosystems. *Agricultural and Forest Meteorology, 152*, 159-177.

Soudani, K., le Maire, G., Dufrene, E., Francois, C., Delpierre, N., Ulrich, E., & Cecchini, S. (2008). Evaluation of the onset of green-up in temperate deciduous broadleaf forests derived from Moderate Resolution Imaging Spectroradiometer (MODIS) data. *Remote Sensing of Environment, 112*(5), 2643-2655.

Story, D., & Kacira, M. (2015). Design and implementation of a computer vision-guided greenhouse crop diagnostics system. *Machine Vision and Applications, 26*(4), 495-506.

Tuanmu, M.-N., Vina, A., Bearer, S., Xu, W., Ouyang, Z., Zhang, H., & Liu, J. (2010). Mapping understory vegetation using phenological characteristics derived from remotely sensed data. *Remote Sensing of Environment, 114*(8), 1833-1844.

Vartanian, M., Nijland, W., Coops, N. C., Bater, C., Wulder, M. A., & Stenhouse, G. (2014). Research note assessing the impact of field of view on monitoring understory and overstory phenology using digital repeat photography. *Journal of Remote Sensing, 40*(2), 85-91.

Villellas, J., Berjano, R., Terrab, A., & Garcia, M. B. (2014). Divergence between phenotypic and genetic variation within populations of a common herb across Europe. *Ecosphere, 5*(5).

Yang, X., Tang, J., & Mustard, J. F. (2014). Beyond leaf color: Comparing camera-based phenological metrics with leaf biochemical, biophysical, and spectral properties throughout the growing season of a temperate deciduous forest. *Journal of Geophysical Research: Biogeosciences, 119*(3), 181-191.

Zhang, X. Y., Friedl, M. A., Schaaf, C. B., Strahler, A. H., Hodges, J. C. F., Gao, F., . . . Huete, A. (2003). Monitoring vegetation phenology using MODIS. *Remote Sensing of Environment, 84*(3), 471-475.

Chapter Three: Estimating Understory Temperatures Using MODIS LST in Mixed Cordilleran Forests

3.1 Abstract

Satellite remote sensing provides a rapid and broad-scale means for monitoring vegetation phenology and its relationship with fluctuations in air temperature. Investigating the response of plant communities to climate change is needed to gain insight into the potentially detrimental effects on ecosystem processes. While many studies have used satellite-derived land surface temperature (LST) as a proxy for air temperature, few studies have attempted to create and validate models of forest understory temperature (T_{ust}), as it is obscured from these space-borne observations. This study worked to predict instantaneous values of T_{ust} using daily Moderate Resolution Imaging Spectroradiometer (MODIS) LST data over a 125,000 km^2 study area located in the Rocky Mountains of western Alberta, Canada. Specifically, we aimed to identify the forest characteristics that improve estimates of T_{ust} over using LST alone. Our top model predicted T_{ust} to within a mean absolute error (MAE) of 1.4°C with an overall model fit of R^2 = 0.89 over two growing seasons. Canopy closure and the LiDAR-derived standard deviation of canopy height metric were found to significantly improve estimations of T_{ust} over MODIS LST alone. These findings demonstrate that canopy structure and forest stand-type function to differentiate understory air temperatures from ambient canopy temperature as seen by the sensor overhead.

3.2 Introduction

There is growing interest in using remote sensing for observing Earth's microclimates in order to acquire a better understanding of ecosystem functions such as vegetation phenology, carbon flux, and the timing of species trophic interactions (e.g. Hanes and Schwartz, 2011). Surface air temperature (T_{air}) is a critical driver of these environmental processes, especially at high latitudes where seasonal transitions are more highly pronounced (White *et al*., 1999). However, obtaining reliable measurements of T_{air} across the landscape is often hindered by missing values due to gaps in the data (Tonini *et al*., 2016). These voids are typically a result of the limited density of meteorological stations distributed across the landscape (Niclòs *et al*., 2014). Spatial interpolation of these data is prone to error because of the distance and fine-scale temperature aberrations between stations, especially in mountainous areas where their distribution tends to be even sparser (Hais and Kucera, 2009; Neteler, 2010; Lin *et al*., 2012). Remote sensing of land surface temperature (LST) helps to resolve this issue by providing an inherently spatialized gridded surface that covers even the most remote regions. The Moderate Resolution Imaging Spectroradiometer (MODIS) has proven invaluable for monitoring year-round global temperature in high temporal detail (Soudani *et al*., 2008). MODIS LST data is particularly popular because of its high level of post-processing which produces accuracies of ≤1°C (Wan, 2008). MODIS LST has successfully been used to predict T_{air} (e.g. Colombi *et al*., 2007; Sun *et al*., 2014), however T_{air} recordings are commonly made in open areas or high above the forest canopy from eddy covariance flux towers (e.g. Sims *et al*., 2008; Jang *et al*., 2014). With observations at heights in excess of 30 m, the relationship between MODIS LST and air temperature in the understory (T_{ust}) is relatively unknown.

Radiometers do not measure air temperature directly, rather the LST estimations are obtained through a split-window algorithm which translates thermal infrared (TIR) observations into skin temperature of the observable land surfaces (i.e., bare land, urban areas, forest canopy) (Wan and Dozier, 1996). LST is quite different from T_{air} and they do not generally correlate well (Sun *et al*., 2005). This relationship is improved over vegetated areas, since emitted radiance is affected by surface type (Mildrexler *et al*., 2011). There is a simple and physical relationship between fractional vegetation cover and thermal properties detected by the sensor (Vancutsem *et al*., 2010). The disparity between LST and T_{air} is greater over areas of exposed soil and other surfaces with low emittance (Prihodko and Goward, 1997). As a result, the direct relationship between LST and T_{air} needs to be determined using a supplementary estimation technique.

Variable forest cover types introduce additional complexities by creating irregularities in the latent heat flux and other radiative exchanges (Jin and Dickinson, 1999; Parmentier *et al*., 2014). The prevalent methodologies used to parameterize T_{air} from LST include (i) physical models of the surface energy balance; and (ii) the temperature–vegetation index (TVX) method (Zakšek and Schroedter-Homscheidt, 2009). Energy-balance models are based on physical processes, and require large amounts of radiation and latent heat flux data typically not provided by remote-sensing techniques (Sun *et al*., 2005; Mostovoy *et al*., 2006). The spectral information obtained by the sensor is not able to perceive many of these complex physical variables, such as wind speed and soil moisture (Stisen *et al*., 2007).

The challenge in measuring the processes that govern T_{air} above vegetation leave most models under-parameterized, and this is the main reason for the development of the

temperature–vegetation index (TVX) method (Vancutsem *et al*., 2010). The premise of the TVX method is an established linear and negative correlation between a remotely-sensed vegetation index, often the normalized difference vegetation index (NDVI), and satellite-derived LST (Nieto *et al*., 2011; Zhu *et al*., 2013). The TVX assumes that the radiometric temperature of a fully vegetated canopy is in equilibrium with T_{air} (Nemani and Running, 1989). The premise is that dense vegetation radiates heat so efficiently that it remains close in temperature to the surrounding ambient air (Prihodko and Goward, 1997). In effect, the assumption is that the top-of-canopy temperature is the same as the canopy itself (Sun *et al*., 2014). How this assumption translates to estimating understory temperatures, and the relationship with MODIS LST across different vegetative strata, requires further investigation.

The difference between air temperatures above and below the forest canopy is generally a result of near-surface environmental lapse rates and distance from the ground (Hanes and Schwartz, 2011). The perspective of forests from a space-borne sensor is of the top of the canopy, and the thermal information beneath is hidden from view due to the relative opacity of the forest itself. The boundary layer separating the emissive properties of the understory and the supracanopy air mass is occupied by different types and densities of canopy vegetation. Therefore estimations of T_{ust}, without assuming that it is in equilibrium with the canopy, should incorporate physical characteristics of the canopy in addition to MODIS LST. These characteristics can be acquired in a number of ways. Traditionally, forest attributes have been obtained through mensuration techniques developed by the timber industry (Husch *et al* 2003). Metrics such as tree height, diameter, and canopy closure are generally used to estimate the volume of harvestable timber in a

stand. These methods have since been adapted to characterize forest landscapes for ecosystem management and studies of species ecology (e.g. Nielsen *et al*., 2006). Recently, these conventional mensuration practices have been complemented by the development of airborne laser scanning (LiDAR) data. LiDAR systems procure detailed models of vegetation in three dimensions, with the fundamental benefit of penetrating the canopy to extract additional information from the understory (Bässler *et al*., 2010; Nijland *et al*., 2015). Most of the existing literature emphasizes characteristics of the overstory, with relatively few papers using LiDAR to examine the understory within an ecological context (Peckham *et al*., 2009; Ewald *et al*., 2014; Melin *et al*., 2014). Nijland *et al*. (2014) compared LiDAR-derived canopy metrics with more conventional climate and land cover based variables to model the distribution of various understory species with mixed success.

The importance of estimating understory temperature is to increase our understanding of its cause–effect relationship with other natural processes. For example, the timing of phenological events is closely linked to changes in ambient temperature, where the life histories of many species are explicitly adapted to the seasonal environments in which they live (Wiegand *et al*., 2008). Monitoring microclimate dynamics provides insight into species sensitivities to weather anomalies and global trends in temperature from climate change (Badeck *et al*., 2004; Hegland *et al*., 2009). The MODIS LST imagery offers a mechanism to observe this significant driver of ecosystem dynamics over the broad scale, which in turn provides maps as a basis for species conservation, habitat management, or identifying additional environmental responses to climate change (Kerr and Otrovsky, 2003; Parmesan and Yohe, 2003; Hebblewhite *et al*., 2008; Coops *et al*., 2012). The present effort to model T_{ust} is motivated by our involvement in an ongoing grizzly bear (*Ursus*

arctos) research program where we are working to monitor critical habitat for this threatened species in Alberta, Canada. These animals strategically exploit a wide variety of understory plants that provide variable nutrition at differential times of the growing season (Nielsen *et al*., 2003). The eventual goal is to model the bears' response to shifting understory phenology by mapping T_{ust} accumulations, or growing degree days (GDD) (e.g. Post *et al*., 2008; Neteler *et al*., 2011; Zorer *et al*., 2013).

The objective of this study is to predict instantaneous measurements of T_{ust} using daily MODIS LST data and a combination of LiDAR-derived canopy metrics and conventional forest inventory variables. Although MODIS LST has been previously correlated with T_{air} (Benali *et al*., 2012; Williamson *et al*., 2014; Xu *et al*., 2014), estimating T_{ust} has not been studied in detail. There is also an absence of in situ meteorological data measured at comparable resolutions to the remotely sensed imagery with which it is correlated (Hanes and Schwartz, 2011). Using a multivariate statistical approach, we ranked the comparative importance of LiDAR and conventional forest inventory variables in estimating instantaneous T_{ust} at the MODIS pixel-scale. In situ T_{ust} measurements were collected over two seasons using a widespread network of meteorological stations distributed throughout the foothills and Rocky Mountains of western Alberta, Canada. Although it is normally assumed that the vegetated canopy is the same temperature as the surrounding ambient air (Prihodko and Goward, 1997; Nemani and Running, 1989), the understory will experience dissimilar temperatures as a result of the general moderating effect of the canopy (von Arx *et al*., 2012). We hypothesized that based on the interactions between MODIS LST and forest canopies (Mildrexler *et al*., 2011), that supplementary

forest canopy and stand variables would significantly improve model predictions of T_{ust} over those made by LST alone.

3.3 Materials and Methods

3.3.1 Study Area

The study area extends over 700 km along the eastern slopes of the Alberta Rocky Mountains (49°N to 55°N) in western Canada (Figure 3.1). T_{ust} observation plots were placed at near-regular latitudinal intervals along elevational transects covering a gradient from 800 m to 1800 m. The forests of the region are typified by deciduous trembling aspen (*Populus tremuloides*) and balsam poplar (*Populus balsamifera*) in mixed stands with white spruce (*Picea glauca*) at lower elevations. The mountains are dominated by mature conifer forests of lodgepole pine (*Pinus contorta*) and Engelmann spruce (*Picea engelmannii*). Stand composition of the observation plots ranged from 40% being purely coniferous, 40% mixed, and 20% entirely deciduous.

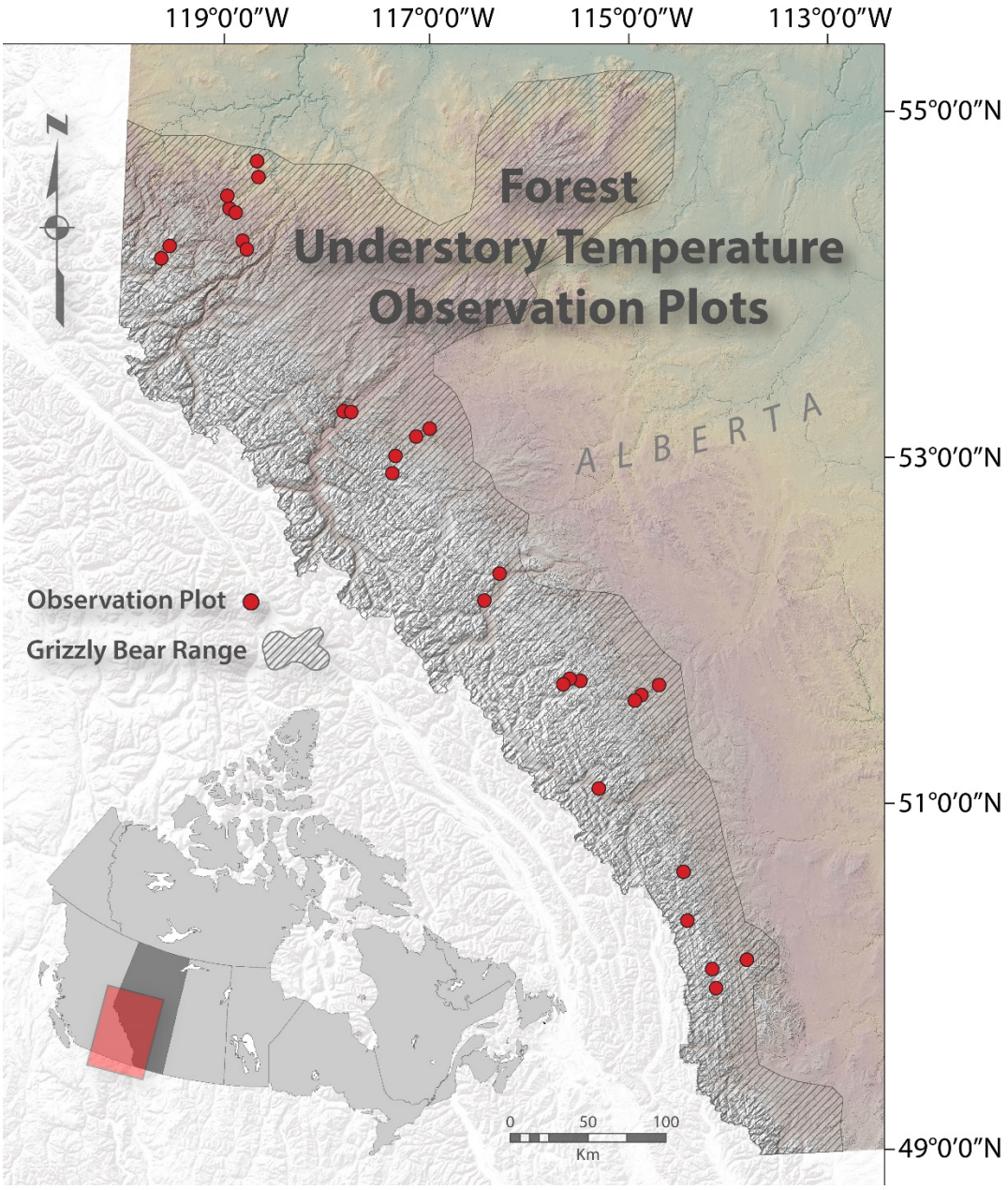

Figure 3.1 Study area extent and understory temperature observation plot locations.

3.3.2 In Situ T_{ust} Observations

Within the study area, twenty-nine broadly dispersed T_{ust} observation plots were selected to obtain a range of temperature regimes, forest composition types, and variability in canopy closure. Each plot was 250 × 250 m (62,500 m^2) in size and located within comparatively homogenous forest stands that extended a minimum of 250 m beyond the edges of the plot. This spatial buffer retained representative temperatures for that particular stand type, minimizing the influence from surrounding divergent cover types. This stand size also corresponds with the areal unit scale of a 1 km MODIS LST pixel (Figure 3.2). Within each plot, four meteorological sensors recorded 8-bit hourly temperature from early spring (pre green-up) until after autumn senescence for two growing seasons: 2011 and 2012. The sensors were enclosed in solar radiation shields 1 m above ground-level, approximating the typical height of shrubby understory vegetation.

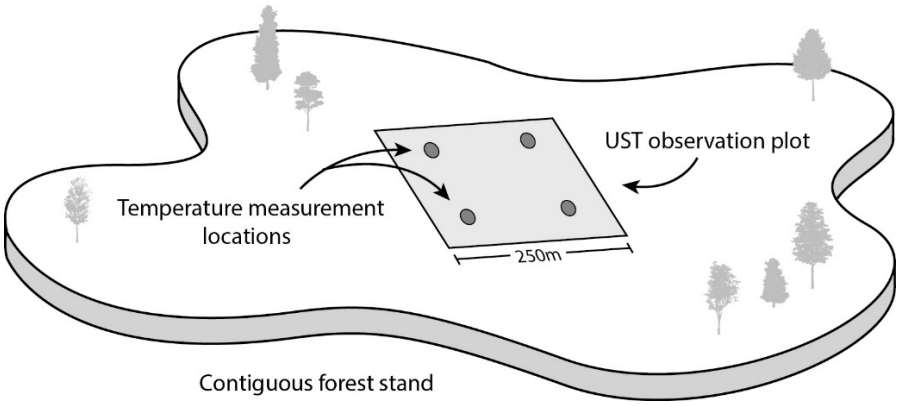

Figure 3.2 Understory temperature (T_{ust}) observation plot and sensor locations.

3.3.3 MODIS Land Surface Temperature Observations

The daily LST product is collected by the sun-synchronous, near-polar orbiting *Terra* (MOD11A1) and *Aqua* (MYD11A1) satellites, with *Aqua* in an ascending orbit and *Terra* in a descending orbit, having two daily equatorial crossings each at 13:30, 01:30, and 10:30, 22:30, respectively (local solar time) (Williamson *et al*., 2013). LST is derived from the MODIS thermal emissivity band channels 31 (10.78–11.28 μm) and 32 (11.77–12.27 μm). Atmospheric effects are corrected using a split-window algorithm that compares the differential thermal radiation absorption between these two bands (Wan *et al*., 2004). Version v005 was the most up-to-date MODIS LST product available, with an accuracy of ≤1°K, and provided significantly improved spatial coverage, stability, and accuracy compared to previous versions (Wan, 2008; Benali *et al*., 2012). Data download and processing was automated using R programming language (R Core Team 2014). The tiled daily LST data were obtained from the NASA Land Processes Distributed Active Archive Center (LP DAAC) for all dates corresponding with the in situ T_{ust} observations. The MODIS Reprojection Tool (Dwyer, 2006) was used to reproject the MOD11A1, MYD11A1, and coincident local solar view time products from Sinusoidal to 1 km gridded geotiff's in Universal Transverse Mercator projection (UTM Zone 11N, NAD83 datum) using nearest-neighbor resampling. Pixel values were then rescaled and converted to degrees Celsius. An abridged methodology is shown in Figure 3.3.

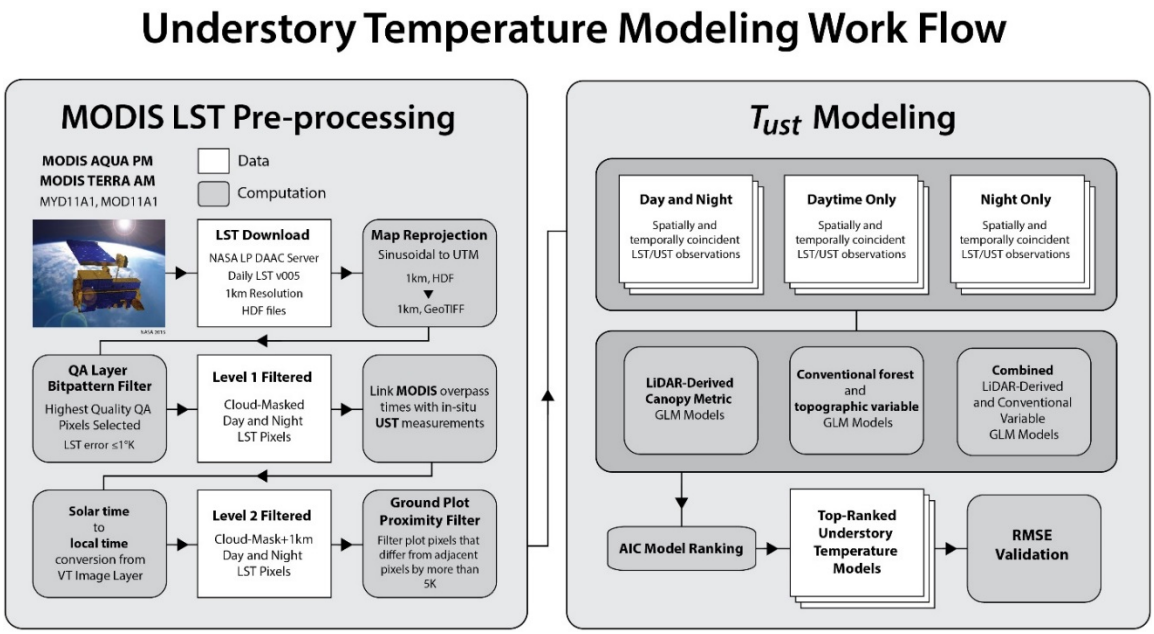

Figure 3.3 Simplified flow chart of the understory temperature modeling process.

Accurate LST measurements are highly dependent on the amount of cloud cover at the time of overpass, therefore a two-step filter process was adapted from Neteler (2010) and Zorer *et al*. (2013) to obtain only the highest quality pixels for each observation plot. The first step used the integrated image bitword quality assessment (QA) flags to mask out cloud or corrupted image pixels. Data were selected with "0" flags in each quality control field, e.g. 00 in "Mandatory QA flags", 00 in "Data quality flag", average emissivity error ≤0.01, average LST error ≤1°K, and view-angle less than 40 degrees from nadir (Yu *et al*., 2011). The second step involved a 1 km proximity search around each observation plot pixel, considering that cloud-contaminated pixels not detected by the QA flags most commonly occur along the edges of clouds (Rizzoli *et al*., 2007; Neteler, 2010). Any adjacent pixel with more than a 5°K difference from an observation plot pixel was

considered corrupted (i.e., from vapor or cloud shadow) and not used in the model. Overall, 1920 MODIS LST images were processed.

To obtain instantaneous measurements of in situ T_{ust}, temporally linking observations with coincident MODIS LST view times was critical. This procedure can be problematic, considering MOD11A1 and MYD11A1 tile data can contain a mosaic of non-sequential and temporally unrelated surface temperatures resulting from multiple daily imaging from adjacent swaths (Williamson *et al*., 2014). Off-nadir viewing is performed to maximize the amount of cloud-free ground surface visible to the sensor during each orbit. To separate the image in to spatially corrected view times, a longitudinal correction was made for each plot and the *equation of time* (Equation 3.1) was applied to the image solar view times to yield local view times (±30 s) with corrections for daylight savings (Equation 3.2) (Huges *et al*., 1989).

$$EOT = 0.258(COSx) - 7.416(SINx) - 3.648(COS2x) - 9.228(SIN2x) \quad \text{(Equation 3.1)}$$

where the angle x is defined as a function of the day of year and produces the difference between mean solar time and true solar time on a given date.

$$Local\ View\ Time = t_s - \frac{EOT}{60} + LC \pm Daylight\ Savings \quad \text{(Equation 3.2)}$$

where t_s is solar time, EOT is the *equation of time*, and LC is the site longitudinal correction from the nearest standard meridian. Once calculated, local LST view times

were then rounded to the nearest hour and coupled with the corresponding hourly T_{ust} plot measurement for every clear sky observation during the study period.

3.3.4 LiDAR-Derived Canopy Metrics

Airborne laser scanning data for the study area were provided by the Government of Alberta's Forest Management Branch. The data were collected between 2003 and 2010 (although the majority is circa 2007 during predominantly leaf-on conditions) using sensors capable of detecting four returns per pulse. Data densities were typically 1–2 returns/m^2. The LiDAR data were normalized to height above ground-level and processed into a suite of height and structure metrics using standard processing routines available in FUSION (McGaughey, 2012). The majority of metrics used first returns in accordance with recommendations in Bater *et al.* (2011), who found that first-return vegetation-height metrics were more stable than those calculated from all-pulse returns. The canopy metrics were averaged over the entire 250 m study plot to approach the areal-unit scale of the MODIS imagery.

Individual LiDAR-derived metrics were selected for use in the models based on their most plausible and intrinsic role in explaining the T_{ust}/LST interface, and also on their predictive success in previous structural understory LiDAR models (e.g. Nijland *et al.*, 2014) (Table 3.1). For example, the ratio pa14 is considered a proxy for canopy closure (1.4 m being the understory height threshold (Nilsson, 1996), while standard deviation of canopy height (stdd) can be thought of as absolute vegetation roughness (Streutker and Glenn, 2006). A number of indices were included because they incorporate all pulse returns. Although being less stable, they potentially provide more information on

subcanopies and understory vegetation than metrics derived from first returns alone (Hudak *et al*., 2009). This was an effort to maximize the utility of the LiDAR data, as it only provides information on vegetation structure, with no additional nuanced ecological information on species assemblies and abundance.

Table 3.1 LiDAR-derived forest canopy metrics/T_{ust} explanatory variables.

Variable Code	Variable Name
h95	95th percentile of height (m)
mean	mean height (m)
stdd	standard deviation of height
skew	skewness of the height distribution
den	density (returns above 1.4 m/all returns)
pa14	percent returns above 1.4 m
Indx14	returns above 1.4 m/1st returns × 100
× lst	interaction term (variable × lst)

3.3.5 Conventional Forest and Topographic Variables

Before the widespread availability of LiDAR and optical remote sensing, forest structure and compositional characteristics were (and still are) traditionally collected by personnel on the ground (Husch *et al*., 2003). These ground data, combined with LST and derived topographic variables, have provided suitable model results for estimating T_{air}. For example, Parmentier *et al*. (2014) used a number of covariates such as forest land cover type, elevation, and aspect to predict monthly average T_{air} to approximately 2.5°C. Variables representing land cover and vegetation type are particularly important since they affect surface emissivity (Wan and Dozier, 1996). Differences between AM and PM LST values have been found to vary between 0.3°C to 3.2°C depending on cover type (Coops *et al*., 2007). Taking into consideration this sensitivity of LST to land cover and canopy density,

forest tree species composition (percent conifer) in each of the 29 observation plots was measured every 50 m along two 250 m stratified-random linear transects (14 subplots per plot). A representative sample of tree species was obtained using a 360° sweep of each subplot using a wedge prism relascope (Figure 3.4). Canopy closure was measured during leaf-on conditions using five hemispherical photographs at each subplot and later processed with WinSCANOPY software (Regent Instruments Inc., 2006) to calculate percent closure. Increased closure was assumed to have insulative properties that provide thermal cover for the ambient understory air mass (Demarchi and Bunnel, 1993; Mildrexler *et al*., 2011).

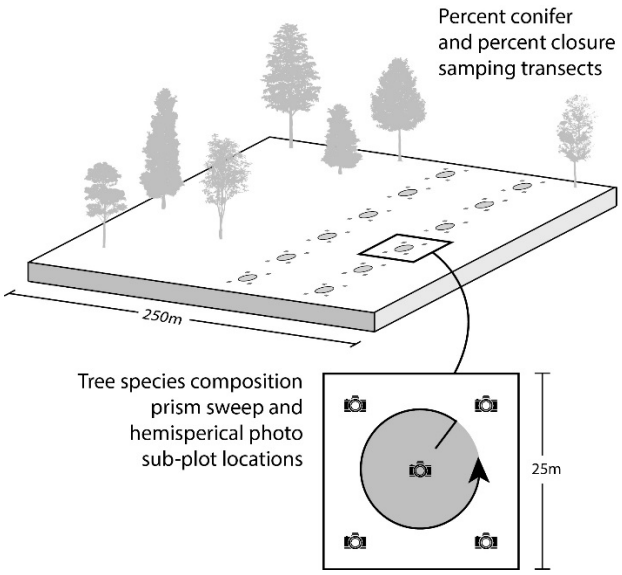

Figure 3.4 Example observation plot sample transects of tree species composition prism sweep sites (percent confer) and hemispherical photography locations (percent closure).

A 10 m photogrammetrically compiled digital elevation model was used to extract topographic variables including elevation, slope, aspect, and annual terrain solar radiation in watt-hours per square meter (WH/m^2) using ArcGIS 10.3 software (ESRI, 2015).

Throughout the year the difference between same-day AM and PM LST observations can vary up to 5°C (Coops *et al*., 2007). Because of this, Julian day was included in the models to account for this variability in the surface energy balance at different times of the growing season. Benali *et al*. (2012) found Julian day to have little predictive effect in their T_{air} models, so the quadratic polynomial of Julian day was used in this study to better represent the seasonal temperature curve (Table 3.2).

Table 3.2 Conventional explanatory variables used for modeling understory temperature.

Variable Code	Variable Name
lst	MODIS land surface temperature (°C)
jday	Julian day
$jday^2$	quadratic of Julian day (jday + $jday^2$)
solar	solar radiation (watts/m^2)
slope	topographic slope (degrees)
asp	aspect (radians)
elev	elevation (meters)
pc	percent coniferous trees
cc	canopy closure (%)
× lst	interaction term (variable × lst)

3.3.6 Statistical Methods and Model Ranking

Regression approaches have previously demonstrated accurate predictions of T_{air} using solely LST or LST associated with ancillary variables (Zorer *et al*., 2013; Jang *et al*., 2014; Metz *et al*., 2014; Niclòs *et al*., 2014; Xu *et al*., 2014). In this application, models were divided into three groupings similar to the organization used by Benali *et al*. (2012), where they modeled instantaneous MODIS LST observations during the (i) daytime; (ii) night; and (iii) using both datasets combined (hereafter referred to as the daytime, night, and day–night models). Separating the dataset in this manner was intended to isolate any effect from

differing diurnal near-surface temperature gradients, insolation variability during the day, and outgoing radiation at night. Within the view-time groupings, candidate models were organized into subgroupings established on explanatory variable type (conventional variables, LiDAR-derived metrics, and both types combined) to assess any marked improvement in model performance between them. Generalized linear models were derived in STATA 13 statistical software (StataCorp, 2013) to estimate instantaneous values of T_{ust}. Random effects (GLS estimator) were used to offset bias from using multiple temperature observations within single sites. A cross-correlation between explanatory variables tested for both linear and monotonic relationships to ensure no collinearity within models. Akaike information criterion (AIC) was used to perform rankings of the candidate models. This procedure seeks to find a balance between model fit (log likelihood) and the number of variables in the model, penalizing those with too much complexity, ranking the best-fit and most parsimonious model as the highest (Wagenmakers and Farrell, 2004). A total of 4153 day and night clear-sky observations were made during the study period (Figure 3.5); 20% of these data were randomly withheld for validation (Willmott, 1981).

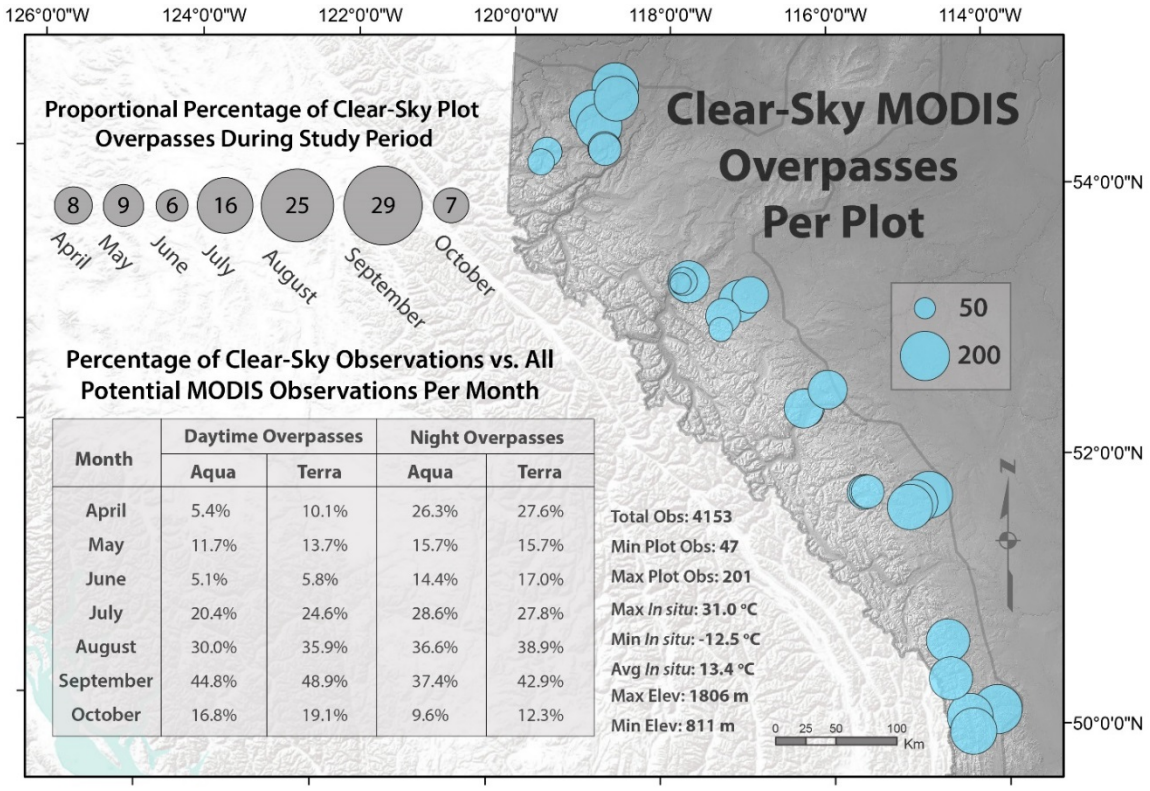

Month	Daytime Overpasses		Night Overpasses	
	Aqua	Terra	Aqua	Terra
April	5.4%	10.1%	26.3%	27.6%
May	11.7%	13.7%	15.7%	15.7%
June	5.1%	5.8%	14.4%	17.0%
July	20.4%	24.6%	28.6%	27.8%
August	30.0%	35.9%	36.6%	38.9%
September	44.8%	48.9%	37.4%	42.9%
October	16.8%	19.1%	9.6%	12.3%

Figure 3.5 Spatial and temporal characteristics of the valid Moderate Resolution Imaging Spectroradiometer (MODIS) overpass dataset including spatial distribution of total clear-sky MODIS overpasses for each observation plot. Also, the proportional percentage of total clear-sky overpasses by month, and the proportional percentage of valid clear-sky observations versus all potential MODIS observations (cloud contamination) for the duration of the study period.

3.4 Results

The quadratic function of Julian day and LST was set as the standard null model, as these two variables were found to explain more than 80% of the variability in T_{ust}. Julian day explained 20% more variability than LST alone, which is considered good for ecological phenomena (Møller and Jennions, 2002). Using all clear-sky observations, separate baseline model rankings of the two variable types (conventional and LiDAR-derived) was performed to get an overview of their relative importance in predicting T_{ust} (Table 3.3).

The delta AIC (Δ_i) is a measure of each model relative to the top-ranked model, where the criterion suggests substantial evidence for models within $\Delta_i < 2$. Values between 3 and 7 indicate that the model has considerably less support, and $\Delta_i > 10$ indicates that the model is very unlikely (Burnham and Anderson, 2007). Akaike weights (w_i) can be interpreted as the probability that the top-ranked model is the best in the set of candidate models (Wagenmakers and Farrell, 2004; Anderson, 2007). Of the conventional metrics, the best model was explained (in addition to the null) by the interaction between LST and percent conifer, which describes the proportion of coniferous trees within a sample unit. The effect of the interaction term in the model can be interpreted as a linkage between these two variables where the influence of forest composition on T_{ust} depends on the coincident LST value at the time of observation. Without the interaction, we are simply trying to predict T_{ust} as solely the unique effect of percent conifer. The top two conventional metric models lead the rankings, each having Akaike weights of 0.50 (percent conifer and the interaction of LST with percent conifer). There was weak support for the addition of elevation, since it is equally ranked with the percent conifer interaction model despite increasing model complexity. By and large, employing conventional variables imparts a major improvement in estimating T_{ust} over using LST alone, which was ranked very poorly.

There was no observed improvement in the prediction of T_{ust} using exclusively LiDAR-derived metrics over the null model (Table 3.3). The best-performing was skewness, although there is some optimism in the strength of the other LiDAR models since they are all within 2 AIC values of the top ranked model (the null). Any LiDAR-derived metric model containing an interaction term had significantly reduced performance which was reflected by a large increase in AIC value.

Table 3.3 Baseline Akaike information criterion (AIC) model rankings (top 10) showing relative performance of conventional and LiDAR-derived variable types, as well as individual variable contributions in estimating T_{ust} using all clear-sky (day–night) observations. Model rank was assessed through difference in AIC values (Δi) and weights (w_i) reflecting model likelihood. Model complexity is characterized by the number of model parameters (K_i).

Conventional Metric Day-Night T_{ust} Model	K_i	**AIC**	Δ_i	w_i
lst + jday + jday² + pc + lst × pc	7	15,903.4	0.0	0.50
lst + jday + jday² + elev + pc + lst × pc	8	15,903.4	0.0	0.50
lst + jday + jday² + elev + cc + lst × cc	8	15,924.4	21.0	0.00
lst + jday + jday² + cc + lst × cc	7	15,926.8	23.4	0.00
lst + jday + jday² + pc + cc	7	15,944.9	41.6	0.00
lst + jday + jday² + pc	6	15,945.1	41.8	0.00
lst + jday + jday² + elev	6	15,945.3	41.9	0.00
lst + jday + jday² + elev + pc	7	15,945.4	42.0	0.00
lst + jday + jday² + elev + cc	7	15,946.4	43.0	0.00
lst + jday + jday² (Standard null model)	5	15,947.7	44.4	0.00
lst	3	16,217.6	314.2	0.00
LiDAR Forest Metric Day-Night T_{ust} Models	K_i	**AIC**	Δ_i	w_i
lst + jday + jday² (Standard null model)	5	15,947.7	0.0	0.17
lst + jday + jday² + skew	6	15,948.5	0.7	0.12
lst + jday + jday² + mean	6	15,949.0	1.3	0.09
lst + jday + jday² + indx14	6	15,949.3	1.5	0.08
lst + jday + jday² + den	6	15,949.58	1.9	0.07
lst + jday + jday² + pa14	6	15,949.59	1.9	0.07
lst + jday + jday² + h95	6	15,949.6	1.9	0.07
lst + jday + jday² + stdd	6	15,949.7	2.0	0.06
lst + jday + jday² + lst × pa14	6	16,296.0	348.2	0.00

The overall top-ranked models from the final groupings (conventional, LiDAR-derived, and both combined) were directly compared to gauge which supplementary variable type best predicts T_{ust}. This comparison was performed for each overpass dataset (daytime, night, and day–night). The combination of conventional variables and LiDAR-derived metrics clearly produced the best models, regardless of view time, as reflected by the large Akaike weights (Table 3.4).

Table 3.4 AIC ranking of the top day-night, night, and daytime models within the candidate groupings of conventional, LiDAR-derived, and the combined metrics to predict T_{ust}.

Top-Ranked Day-Night T_{ust} Models		K_i	AIC	Δ_i	w_i
1. lst + jday + jday^2 + cc + stdd + lst × cc + lst × stdd	Combined metrics	9	15,804.6	0.0	1.00
2. lst + jday + jday^2 + pc + lst × pc	Conventional metrics	7	15,903.4	98.7	0.00
3. lst + jday + jday^2	Standard null	5	15,947.7	143.1	0.00
4. lst + jday + jday^2 + skew	LiDAR-derived metrics	6	15,948.5	143.8	0.00
Top-Ranked Night T_{ust} Models		K_i	AIC	Δ_i	w_i
1. lst + jday + jday^2 + elev + cc + stdd + lst × cc	Combined metrics	9	8367.1	0.0	0.82
2. lst + jday + jday^2 + skew	LiDAR-derived metrics	6	8371.2	4.1	0.11
3. lst + jday + jday^2 + pc	Conventional metrics	6	8372.2	5.1	0.06
4. lst + jday + jday^2	Standard null	5	8375.5	8.3	0.01
Top-Ranked Daytime T_{ust} Models		K_i	AIC	Δ_i	w_i
1. lst + jday + jday^2 + cc + stdd + lst × stdd	Combined metrics	8	6673.4	0.0	0.76
2. lst + jday + jday^2 + cc	Conventional metrics	6	6695.0	3.7	0.12
3. lst + jday + jday^2	Standard null	5	6695.9	4.5	0.08
4. lst + jday + jday^2 + pa14	LiDAR-derived metrics	6	6697.1	5.7	0.04

Percent canopy closure (cc) and the LiDAR-derived metric standard deviation of canopy height (stdd) both appear in all of the top-ranked models. They are often in the form of an interaction term with LST, which is a strong indication of an interrelationship with the forest canopy. At night, the standardized coefficients show that for every percent increase in canopy closure, there will be a 0.06°C increase in T_{ust} (Table 3.5). During the day, for every unit increase in closure, T_{ust} decreases 0.12°C. Also in the top daytime models was the percent returns above 1.4 m (pa14) metric, which is the LiDAR-derived equivalent to canopy closure. This metric had a similar negative daytime influence as closure, where an increase in this variable produces a slight drop in T_{ust}. For both the daytime and day–night models, the interaction term of the LiDAR-derived standard deviation of canopy height was positive, and implies that when LST interacts with increasingly rough canopies, T_{ust} increases, but very little. At night this relationship is inverted, and a higher standard deviation in height results in a cooling of T_{ust}. The percent

conifer coefficient was negative, suggesting that as the percentage of conifers increases, T_{ust} will decrease. Overall, canopy closure and the standard deviation of canopy height were the most influential ancillary variables for estimating T_{ust}.

Table 3.5 Estimated parameters for the top-ranked models from each overpass dataset. Standardized coefficients and standard errors (in parentheses) are presented by model.

	lst	jday	jday²	cc	pc	pa14	skew	elev	stdd	lst × cc	lst × pc	lst × stdd
Day-Night Model												
1. Combined	0.96 * (0.03)	0.83 * (0.05)	−0.83 * (0.05)	−0.06 * (0.02)					−0.09 * (0.02)	−0.30 * (0.03)		0.24 * (0.02)
2. Conventional	0.82 * (0.01)	0.82 * (0.05)	−0.82 * (0.05)		−0.08 * (0.02)						0.08 * (0.01)	
3. LiDAR derived	0.88 * (0.00)	0.85 * (0.05)	−0.85 * (0.05)				−0.02 (0.02)					
Night Model												
1. Combined	0.60 * (0.07)	1.23 * (0.15)	−1.20 * (0.14)	0.06 * (0.03)				−0.1 * (0.03)	−0.11 * (0.03)	0.14 * (0.07)		
2. LiDAR derived	0.75 * (0.02)	1.17 * (0.14)	−1.15 * (0.14)				−0.06 * (0.02)					
3. Conventional	0.74 * (0.02)	1.19 * (0.14)	−1.16 * (0.14)		−0.07 * (0.03)							
Daytime Model												
1. Combined	0.87 * (0.03)	0.81 * (0.08)	−0.79 * (0.08)	−0.12 * (0.04)					0.05 (0.05)			0.07 (0.04)
2. Conventional	0.92 * (0.07)	0.81 * (0.08)	−0.80 * (0.08)	−0.06 (0.04)								
3. LiDAR derived	0.92 * (0.01)	0.81 * (0.08)	−0.80 * (0.08)			−0.03 (0.04)						

* indicates statistical significance at $p < 0.05$.

The daytime model was the best performing overall, with a model fit of $R^2 = 0.89$, and the lowest validation error of mean absolute error (MAE) = 1.4°C. This prediction accuracy parallels estimations of T_{air} (Jang *et al*., 2014; Niclòs *et al*., 2014; Xu *et al*., 2014), which is noteworthy considering the predictions are of temperatures beneath the forest canopy (Table 3.6; Figure 3.6).

Table 3.6 Comprehensive results of the top-ranked T_{ust} models. Coefficient of determination (R^2), mean absolute error (MAE), root mean square error (RMSE).

Top Model	Model Fit	MAE	RMSE	BIAS
Day	$R^2 = 0.89$	1.4 °C	1.9 °C	−0.003 °C
Day-Night	$R^2 = 0.89$	1.9 °C	2.4 °C	0.01 °C
Night	$R^2 = 0.77$	2.1 °C	2.6 °C	0.1 °C

The best day–night model had the same model fit as the daytime model ($R^2 = 0.89$), but had a 0.5°C increase in error (MAE of 1.9°C). Although this model had no overall bias, the validation data show a slight T_{ust} underprediction in cooler temperatures that occur during the very start and end of the growing season (Figure 3.7). The top model derived from night observations had the lowest model fit of the three MODIS view times ($R^2 = 0.77$) and a small error increase over the daytime model in estimation error (MAE = 2.1°C). The model appears to underestimate higher temperatures and overestimate colder temperatures which seem to balance out, producing no predictive bias on average.

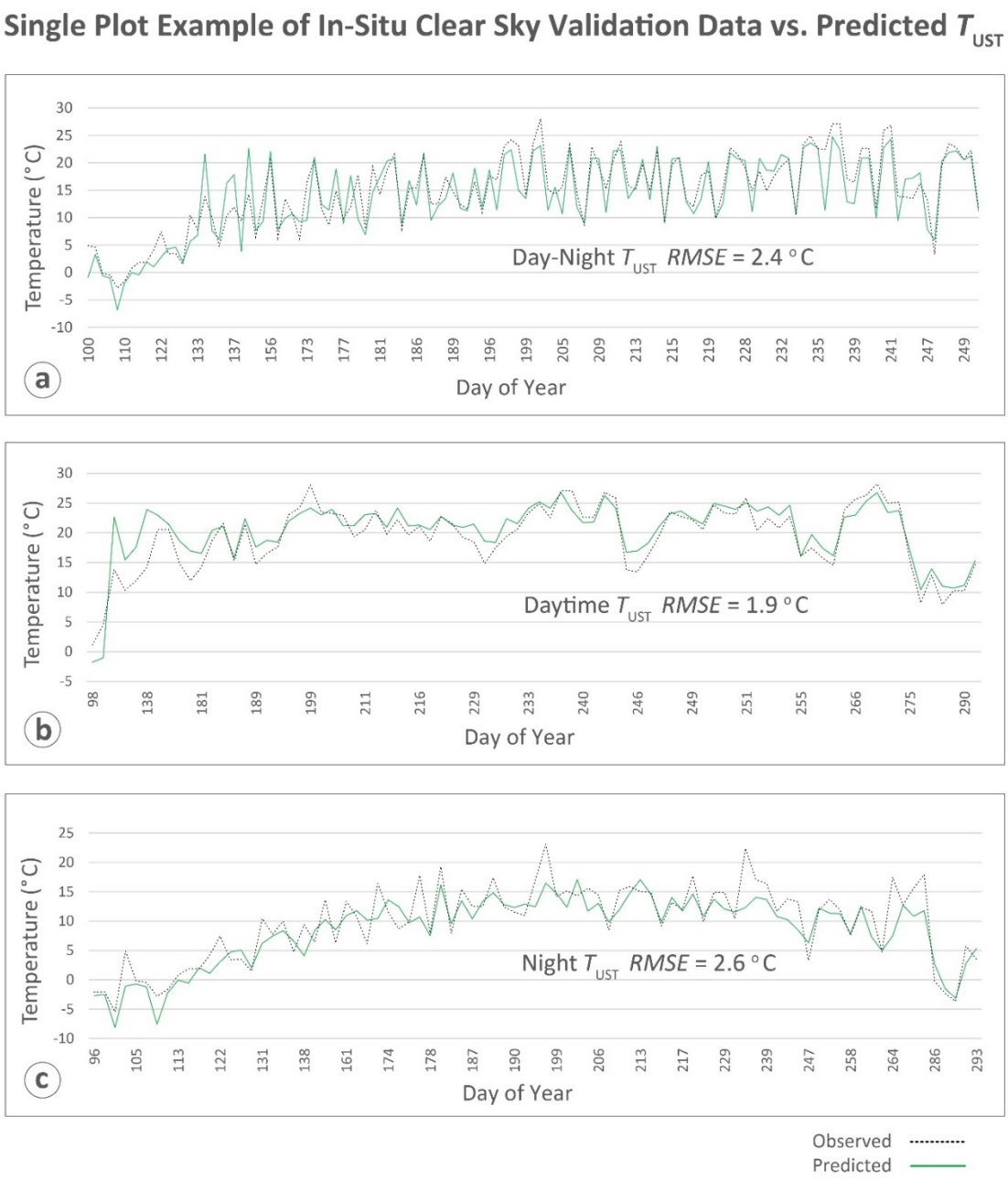

Figure 3.6 In situ understory temperatures vs. predicted T_{ust} values estimated using the top-ranked models for (a) day and night; (b) daytime; and (c) night. These validation data were collected during clear-sky MODIS overpasses within a nearly-deciduous (6% conifer) observation plot with moderate canopy closure (60%) at an elevation of 1330 m.

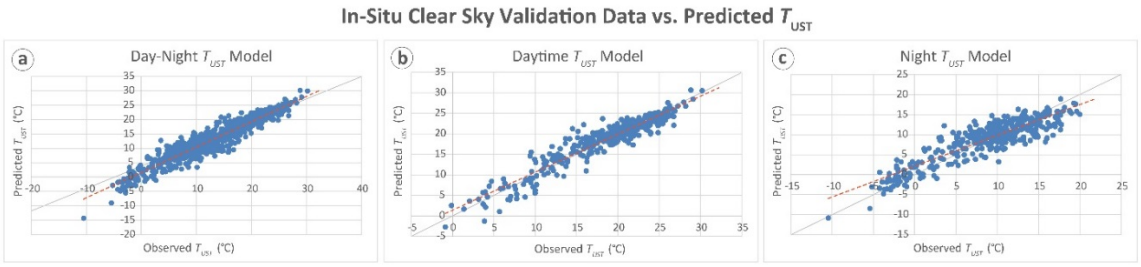

Figure 3.7 In situ understory temperatures vs. predicted T_{ust} values estimated using the top-ranked models for (a) day and night; (b) daytime; and (c) night. Data are the randomly withheld clear-sky MODIS overpasses of the study area over the duration of the study period.

3.5 Discussion

Forest type, density, and canopy structure all have an impact on the relationship between MODIS LST and understory air temperature. In this paper, we examined which metrics coupled with MODIS LST improve estimates of T_{ust}. This is, to our knowledge, the first study of its kind to specifically model air temperatures in the understory using MODIS LST. We statistically predicted instantaneous values of T_{ust} at a 250 m plot-scale to within MAE 1.4°C–2.1°C (depending on the time of day). This is comparable to previous canopy-top T_{air} models that had error ranging from 1.3°C to 3.5°C and similar model fit (Columbi *et al.*, 2007; Benali *et al.*, 2012; Jang *et al.*, 2014; Niclòs *et al.*, 2014). The fit slightly exceeded that obtained by Hanes and Schwartz (2011), who modeled maximum daily T_{air} at the base of a flux tower (1.5 m) ($R^2 = 0.86$).

The T_{ust} estimates were consistently accurate over a range of forest types and densities. This may be a result of the overall effectiveness of the model variables at representing the forest canopy characteristics. This variability could not be explained by LST alone (null model) as demonstrated in the AIC rankings. Despite the cost of increased model complexity, those which contained canopy metrics consistently ranked higher than

the LST null model. A likelihood ratio test was performed to determine if these top-ranked models estimated T_{ust} significantly better than the null. The results found that the addition of canopy metrics produce a significant improvement over the LST null in the day–night combined model ($p < 0.001$), and marginally significant in the daytime and night models ($p = 0.08$; $p = 0.07$).

The improvement of the models through the addition of the canopy metrics implies that there is a distinction between canopy-top (T_{air}) and understory temperatures. The difference is likely a result of moderation from the canopy (von Arx *et al*., 2012; Flerchinger *et al*., 2015). Hanes and Schwartz (2011) found that as canopy vegetation becomes increasingly dense during spring leaf out, MODIS LST values begin to approach air temperatures at 1.5 m above ground. In areas where canopy density is reduced, the influence of the overlying forest is diminished and therefore LST should deviate from T_{air}. However, the T_{ust} estimates across the study area are consistently accurate despite the broad range of forest densities in the plots (10%–70% closure). This finding implies that, unlike T_{air}, the relationship between LST and T_{ust} is likely consistent regardless of canopy closure.

Modeling day and night LST as separate datasets highlighted daytime as the optimal diurnal period to observe T_{ust}. The daytime model was best overall, with a 10% increase in model fit and 0.7°C lower error than at night. The majority of previous T_{air} studies (e.g. Sims *et al*., 2008) have found increased accuracy during the night, which is attributed to less interference from reflected daytime radiation (Rahman *et al*., 2015). The improved daytime accuracy in the T_{ust} models may be owed to modeling entirely within forested sites and the inherent difference of estimating T_{ust} as opposed to T_{air}. Essentially, the radiative exchanges in the understory are sufficiently unique to those above the canopy

resulting in improved daytime T_{ust} observations. In addition, the predominance of conifer trees in the study area may have augmented the performance of the daytime model, since low albedo coniferous canopy absorbs and emits energy more effectively than deciduous (Gao *et al*., 2005); green-needle forest is considered a near-perfect emitter of thermal radiation (Snyder *et al*., 1998). This is supported in a daytime model by the positive interaction between LST and percent conifer. This same interaction term is not present in the night model, perhaps because there is no potential for interaction with sunlight.

Conifer forests are also drier than deciduous, ultimately affecting the latent heat flux between them throughout the diurnal cycle. Williamson *et al*. (2014) and Niclòs *et al*. (2014) found that soil moisture was a significant predictor of T_{air} as it affects surface emissivity. Considering at-site soil moisture was not measured in this study, GIS-derived variables could have been used as proxies for moisture such as a wet area map (Nijland *et al*., 2014). Cresswell *et al*. (1999) explain that since the Earth's skin surface temperature is generally higher than T_{air} during the day and cooler at night, this will lead to overestimation and underestimation of air temperature in diurnal T_{air} models, respectively. However, this estimation bias was not observed between the T_{ust} models, perhaps from the moderating effect of the canopy. At night, there was a positive LST interaction with canopy closure which in turn increased T_{ust}. During the day, this relationship was negative and for every percent increase in closure, T_{ust} decreased 0.12°C. These results corroborate that the canopy shades the understory during the day and insulates it at night (You *et al*., 2013; Melin *et al* 2014). This also implies that the understory microclimate is unique to the overlying canopy and therefore emphasizes the distinction between T_{air} and T_{ust}.

Regarding the performance of the LiDAR-derived metrics, they contributed to all of the top-ranked models, indicating some overall utility. The standard deviation of canopy height was the most predictive either as a solitary variable (at night) or interacting with LST (daytime). It would be more intuitive that average height or canopy density (percent returns above 1.4 m) should explain more variability in T_{ust}; rather it was the roughness of the forest as expressed by the standard deviation of height (Melin *et al*., 2014). During the daytime T_{ust} rises when forest structure becomes increasingly rough, while at night the opposite occurs, where a higher standard deviation results in lower T_{ust}. A rough surface would be characteristic of forest with a strong variation in age structure or disturbance patterns such as trails or cut lines. Although not in the top-ranked models, LiDAR-derived skewness in the distribution of tree heights appeared strongly in many of the models, having a significant yet subtle influence on T_{ust}. Skewness is a similar metric to standard deviation and signifies canopy complexities resulting from variable age structure or directional trends in height across the plot due to soil conditions or slope (Yochum *et al*., 2014). The correlation of this metric with T_{ust} was at all times negative, suggesting that as skewness in height increases, T_{ust} drops slightly. The relative contribution to model improvement using the LiDAR metrics raises the question of the advantage of these data over the conventional and GIS-derived variables. Ultimately, it depends on the scale and objectives of the research; in this T_{ust} analysis, the benefits of the LiDAR metrics were not as substantial as the conventional variables. Conversely, the cost of traditional ground measurements are considerably more than LiDAR surveys (Montaghi *et al*., 2013), especially in contrast to the increasing availability of LiDAR technology and platforms such as unmanned aerial systems (Liesen *et al*., 2014; Paneque-Galvez *et al*., 2014).

Downscaling the 2-pulse-per-meter LiDAR metrics to the 250 m plot-scale could have impacted their effectiveness as explanatory variables of T_{ust}. This was done to match the areal unit scale of the observation plots, however it is unlikely that the effect was significant as averaging would only remove the extreme and outlying values. Tompalski *et al.* (2015) compared stand-level LiDAR estimates of tree volume to individual volume measurements and found them to be very similar. The areal scale of 250 m was conceivably an improvement over point-source temperature measurements made by lone meteorological stations or flux towers. The relatively low root mean square error (RMSE) in the T_{ust} models may be indicative of measuring in situ temperature at a broader 250 m scale instead of discrete points on the landscape. The observation plots were located in the center of more expansive areas of homogeneous forest as a solution to the disparity between the resolutions of the larger MODIS LST pixel and the T_{ust} plots. Olsson and Jonsson (Olsson and Jonsson, 2015) found that different scales of gridded temperature source-data (e.g. MODIS LST) had no significant influence on the accuracy of their forest phenology models.

For this mitigation approach to operate effectively, it was assumed that temperature across the broader homogenous stand was uniform. This assumption was validated over two seasons, by recording in situ air temperature within a 250 m plot placed at the center of a broad expanse (2700 km^2) of perfectly homogenous land cover (native grassland). Employing the identical methodologies as in the forested plots, these data were used to train the LST null model. Air temperature estimates in the validation plot had an average RMSE increase of 2°C over the equivalent null model estimates in the forested plots. Theoretically, the error should have been lower since the validation plot had completely

uniform land cover relative to the principal observation plots. However, this result substantiates that forest cover improves statistical estimates of air temperature using LST (Mostovoy *et al*., 2006).

The tiled and projected M*D11A1 products were chosen for this study based on their ease of use and successful application in previous models (e.g. Neteler, 2010; Zorer *et al*., 2013). The lower-level LST swath data are less modified and unaffected by projection error or temporal adjustments. However, opting for the higher-level product was a tradeoff between these errors versus the benefit of having the obvious cloud-contaminated LST values removed. During pre-processing the LST imagery selected for this study was reprojected and resampled, which introduces geometric error: chiefly the potential to alter the LST pixel value with values from adjacent cover types. We attempted to mitigate this issue by working in forest stands that were much larger than the plots in which observations were made. Some error may have originated from intrinsic uncertainties in the radiometric or geometric precision of the original MODIS LST data (Neteler, 2010), yet this was mitigated by using only the highest quality QA filtered pixels for the analysis. The local time correction made during pre-processing produced times that were truly instantaneous or within 30 minutes of a MODIS overpass. It is unlikely that this period was sufficient to allow any significant change in temperature on the ground, but it cannot be ruled out completely.

Terrain complexity within the study area introduced an assortment topographic and microclimatic factors, but these had little effect on the model results. This was expected since this study was a within-pixel analysis with no broader spatial interpolation. Observation plots with limited topography were intentionally selected as “targets” for

MODIS in an attempt to constrain the variability of T_{ust} solely to forest type and structure. Elevation was the only significant topographic variable in the models because small differences in elevation produce considerable changes in the environmental lapse rate (e.g. Linj *et al*., 2012). The use of aspirated solar radiation shields worked to limit in situ T_{ust} measurement bias. However, variability in canopy cover between plots may have exposed some sensors to slightly more radiation than others, potentially altering the results (Thomas and Smoot, 2013).

Clear-sky overpasses occurred predominantly during the summer and autumn months, however a considerable proportion occurred in autumn. The canopy is mostly intact for the first half of September, but leaf senescence may have introduced some bias in the small proportion of plots that were deciduous. Given the enduring issue of cloud over the mountains, there was a trade-off between increased observations during a reliably clear time of year and the transition in canopy attributes. An extended observation period was required to observe the full phenological progression of the understory and to obtain a range of seasonal temperatures. Other sources of model uncertainty most likely occurred during exceedingly cold times of year. The MODIS LST product is accurate to ±1°C between the temperatures of −10°C and 50°C (Wan, 2008), there were early and late season temperatures during the study period that were approximately −20°C potentially reducing model accuracy. This evidence of seasonal variability affecting model estimates is substantiated by Hanes and Schwartz (2011) who found that differences between T_{air} and MODIS LST are increasingly divergent during colder parts of the year in temperate climates, mainly due to snow cover. However, for the purposes of using T_{ust} for monitoring

vegetation phenology, the accuracy of T_{ust} models is not critical during these colder periods since the plants are still dormant and GDD accumulations have not yet begun.

Overall, the models demonstrate that estimates of T_{ust} using MODIS LST can be refined with additional variables which characterize the interface between the top of the forest canopy and the understory. These results facilitate the next step in this research to monitor understory phenology over the entire study area. This requires spatially extending the models beyond the observation plots across the gridded MODIS LST surface to produce maps of daily T_{ust}. GDD maps derived from T_{ust} should provide improved accuracy in predictions of understory plant phenology than those derived from canopy-top T_{air}. Hanes and Schwartz (2011) found that top-of-flux tower GDD accumulations underpredicted plant phenology opposed to measurements made closer to the ground since lapse rates produce cooler temperatures at height. The instantaneous T_{ust} models derived in this study will ultimately facilitate the development of improved land surface phenology maps.

3.6 Conclusions

Fluctuations in surface air temperature drive a variety of environmental processes which include radiative energy and gas fluxes, species interactions, and vegetation growth. Recently there has been growing importance on collecting thermal data from satellite platforms to estimate T_{air} at regional and global extents (Mildrexler *et al*., 2011; Kloog *et al*., 2014). However, the use of remote sensing for modeling forest understory temperatures has yet to be explored. In this paper we described a methodology for predicting plot-scale T_{ust} using MODIS LST and a combination of conventional forest inventory variables and LiDAR-derived canopy metrics. The objective aimed to identify

which of these ancillary characteristics played a critical role in modifying estimates of the underlying temperatures. T_{ust} was predicted to within 1.4°C across a variety of forest types and elevations. Canopy closure and the LiDAR-derived standard deviation of canopy height metric were found to significantly improve estimations of T_{ust} over MODIS LST alone. These findings confirm that canopy structure and forest stand-type can function to differentiate understory air temperatures from ambient canopy temperature as observed by the sensor overhead.

This study developed a remote sensing procedure that works to uncover detailed microclimatic conditions beneath the forest canopy. This type of mechanistic data is particularly useful for ecological modeling (Nielsen *et al*., 2010), but is normally obtained from solitary weather stations or gridded top-of-canopy temperature surfaces. The T_{ust} models were trained using in situ temperature data collected over a broader ground surface to approximate the pixel size of the MODIS imagery. This effort to align the spatial scale of observations likely improved the results and is recommended for any remote sensing investigations collecting surface temperature at moderate resolutions.

These models provide useful estimations of T_{ust} at the plot-scale, but to fully benefit from the spatial nature of the remotely-sensed datasets it would be essential to develop broad-extent daily maps of T_{ust}. There is a need for such a dataset, but foreseeable challenges include producing maps without spatial or temporal punctuations in the time series. Current trends in global climate necessitate predictions of how ecosystem processes will respond to these changes (Buckley *et al*., 2010; Lambers, 2015), and continuous maps of air temperature are instrumental in answering this question. Future research in this area promises to be rewarding

as space-borne technologies continuously advance alongside ongoing LST product improvements (e.g. the recent release of MODIS collection version 6). These invaluable and freely available data will provide rapid assessments of the earth surface with perpetually increasing accuracy and precision.

3.7 References

Anderson, D. R. (2007). Model Based Inference in the Life Sciences: A Primer on Evidence. Springer, New York.

Badeck, F.-W., Bondeau, A., Bottcher, K., Doktor, D., Lucht, W., Schaber, J., & Sitch, S. (2004). Responses of spring phenology to climate change. *New Phytologist, 162*(2), 295-309.

Bässler, C., Stadler, J., Müller, J., Förster, B., Göttlein, A., & Brandl, R. (2010). LiDAR as a rapid tool to predict forest habitat types in Natura 2000 networks. *Biodiversity and Conservation*, 1-17.

Bater, C. W., Wulder, M. A., Coops, N. C., Nelson, R. F., Hilker, T., & Nasset, E. (2011). Stability of sample-based scanning-LiDAR-derived vegetation metrics for forest monitoring. *Geoscience and Remote Sensing, IEEE Transactions on, 49*(6), 2385-2392.

Benali, A., Carvalho, A. C., Nunes, J. P., Carvalhais, N., & Santos, A. (2012). Estimating air surface temperature in Portugal using MODIS LST data. *Remote Sensing of Environment, 124*(0), 108-121.

Buckley, L. B., Urban, M. C., Angilletta, M. J., Crozier, L. G., Rissler, L. J., & Sears, M. W. (2010). Can mechanism inform species' distribution models? *Ecology Letters, 13*(8), 1041-1054.

Burnham, K. P., & Anderson, D. R. (2007). Model Selection and Multimodel Inference: A Practical Information-Theoretic Approach. Springer, New York.

Colombi, A., De Michele, C., Pepe, M., & Rampini, A. (2007). Estimation of daily mean air temperature from MODIS LST in Alpine areas. *EARSeL eProceedings, 6*(1), 38-46.

Coops, N. C., Duro, D. C., Wulder, M. A., & Han, T. (2007). Estimating afternoon MODIS land surface temperatures (LST) based on morning MODIS overpass, location and elevation information. *International Journal of Remote Sensing, 28*(10), 2391-2396.

Coops, N. C., Hilker, T., Bater, C. W., Wulder, M. A., Nielsen, S. E., McDermid, G., & Stenhouse, G. (2012). Linking ground-based to satellite-derived phenological metrics in support of habitat assessment. *Remote Sensing Letters, 3*(3), 191-200.

Cresswell, M. P., Morse, A. P., Thomson, M. C., & Connor, S. J. (1999). Estimating surface air temperatures, from Meteosat land surface temperatures, using an empirical solar zenith angle model. *International Journal of Remote Sensing, 20*(6), 1125-1132.

Demarchi, M. W., & Bunnell, F. L. (1993). Estimating forest canopy effects on summer thermal cover for *Cervidae* (deer family). *Canadian Journal of Forest Research, 23*(11), 2419-2426.

Dwyer, J., & Schmidt, G. (2006). The MODIS Reprojection Tool. In J. J. Qu, W. Gao, M. Kafatos, R. E. Murphy & V. V. Salomonson (Eds.), *Earth Science Satellite Remote Sensing: Vol. 2: Data, Computational Processing, and Tools* (pp. 162-177). Springer, Berlin Heidelberg.

ESRI. (2015). ArcGIS Desktop: Release 10.3. Redlands, CA: Environmental Systems Research Institute.

Ewald, M., Dupke, C., Heurich, M., Mueller, J., & Reineking, B. (2014). LiDAR Remote sensing of forest structure and GPS telemetry data provide insights on winter habitat selection of European roe deer. *Forests, 5*(6), 1374-1390.

Flerchinger, G. N., Reba, M. L., Link, T. E., & Marks, D. (2015). Modeling temperature and humidity profiles within forest canopies. *Agricultural and Forest Meteorology, 213*, 251-262.

Gao, F., Schaaf, C. B., Strahler, A. H., Roesch, A., Lucht, W., & Dickinson, R. (2005). MODIS bidirectional reflectance distribution function and albedo Climate Modeling Grid products and the variability of albedo for major global vegetation types. *Journal of Geophysical Research-Atmospheres, 110*(D1).

Hais, M., & Kucera, T. (2009). The influence of topography on the forest surface temperature retrieved from Landsat TM, ETM plus and ASTER thermal channels. *ISPRS Journal of Photogrammetry and Remote Sensing, 64*(6), 585-591.

Hanes, J. M., & Schwartz, M. D. (2011). Modeling land surface phenology in a mixed temperate forest using MODIS measurements of leaf area index and land surface temperature. *Theoretical and Applied Climatology, 105*(1-2), 37-50.

Hebblewhite, M., Merrill, E., & McDermid, G. (2008). A multi-scale test of the forage maturation hypothesis in a partially migratory ungulate population. *Ecological Monographs, 78*(2), 141-166.

Hegland, S. J., Nielsen, A., Lazaro, A., Bjerknes, A.-L., & Totland, O. (2009). How does climate warming affect plant-pollinator interactions? *Ecology Letters, 12*(2), 184-195.

Hudak, A. T., Evans, J. S., & Stuart Smith, A. M. (2009). LiDAR utility for natural resource managers. *Remote Sensing, 1*(4), 934-951.

Hughes, D. W., Yallop, B., & Hohenkerk, C. (1989). The equation of time. *Monthly Notices of the Royal Astronomical Society, 238*(4), 1529-1535.

Husch, B., Beers, T. W., & Kershaw, J. A. (2003). *Forest mensuration*. New York: J. Wiley.

Jang, K., Kang, S., Kimball, J. S., & Hong, S. Y. (2014). Retrievals of all-weather daily air temperature using MODIS and AMSR-E data. *Remote Sensing, 6*(9), 8387-8404.

Jin, M. L., & Dickinson, R. E. (1999). Interpolation of surface radiative temperature measured from polar orbiting satellites to a diurnal cycle: 1. Without clouds. *Journal of Geophysical Research-Atmospheres, 104*(D2), 2105-2116.

Kerr, J. T., & Ostrovsky, M. (2003). From space to species: ecological applications for remote sensing. *Trends in Ecology & Evolution, 18*(6), 299-305.

Kloog, I., Nordio, F., Coull, B. A., & Schwartz, J. (2014). Predicting spatiotemporal mean air temperature using MODIS satellite surface temperature measurements across the Northeastern USA. *Remote Sensing of Environment, 150*, 132-139.

Lambers, J. H. R. (2015). Extinction risks from climate change. *Science, 348*(6234), 501-502.

Lin, S., Moore, N. J., Messina, J. P., DeVisser, M. H., & Wu, J. (2012). Evaluation of estimating daily maximum and minimum air temperature with MODIS data in east Africa. *International Journal of Applied Earth Observation and Geoinformation, 18*, 128-140.

Lisein, J., Pierrot-Deseilligny, M., Bonnet, S., & Lejeune, P. (2013). A photogrammetric workflow for the creation of a forest canopy height model from small unmanned aerial system imagery. *Forests, 4*(4), 922-944.

McGaughey, R. J. (2012). FUSION/LDV: Software for LIDAR data analysis and Visualization. Seattle, USA: United States Department of Agriculture, Forest Service, Pacific Northwest Research Station.

Melin, M., Matala, J., Mehtatalo, L., Tiilikainen, R., Tikkanen, O.-P., Maltamo, M., . . . Packalen, P. (2014). Moose (*Alces alces*) reacts to high summer temperatures by utilizing thermal shelters in boreal forests - an analysis based on airborne laser scanning of the canopy structure at moose locations. *Global Change Biology, 20*(4), 1115-1125.

Metz, M., Rocchini, D., & Neteler, M. (2014). Surface temperatures at the continental scale: tracking changes with remote sensing at unprecedented detail. *Remote Sensing, 6*(5), 3822-3840.

Mildrexler, D. J., Zhao, M., & Running, S. W. (2011). A global comparison between station air temperatures and MODIS land surface temperatures reveals the cooling role of forests. *Journal of Geophysical Research-Biogeosciences, 116*.

Møller, A., & Jennions, M. D. (2002). How much variance can be explained by ecologists and evolutionary biologists? *Oecologia, 132*(4), 492-500.

Montaghi, A., Corona, P., Dalponte, M., Gianelle, D., Chirici, G., & Olsson, H. (2013). Airborne laser scanning of forest resources: An overview of research in Italy as a commentary case study. *International Journal of Applied Earth Observation and Geoinformation, 23*(0), 288-300.

Mostovoy, G. V., King, R. L., Reddy, K. R., Kakani, V. G., & Filippova, M. G. (2006). Statistical estimation of daily maximum and minimum air temperatures from MODIS LST data over the State of Mississippi. *Giscience & Remote Sensing, 43*(1), 78-110.

Nemani, R. R., & Running, S. W. (1989). Estimation of regional surface resistance to evapotranspiration from NDVI and thermal-IR AVHRR data. *Journal of Applied Meteorology, 28*(4), 276-284.

Neteler, M. (2010). Estimating daily land surface temperatures in mountainous environments by reconstructed MODIS LST data. *Remote Sensing, 2*(1), 333-351.

Neteler, M., Roiz, D., Rocchini, D., Castellani, C., & Rizzoli, A. (2011). Terra and Aqua satellites track tiger mosquito invasion: modelling the potential distribution of Aedes albopictus in north-eastern Italy. *International Journal of Health Geographics, 10*.

Niclos, R., Valiente, J. A., Barbera, M. J., & Caselles, V. (2014). Land surface air temperature retrieval from EOS-MODIS images. *IEEE Geoscience and Remote Sensing Letters, 11*(8), 1380-1384.

Nielsen, S. E., Boyce, M. S., Stenhouse, G. B., & Munro, R. H. M. (2003). Development and testing of phenologically driven grizzly bear habitat models. *Ecoscience, 10*(1), 1-10.

Nielsen, S. E., McDermid, G., Stenhouse, G. B., & Boyce, M. S. (2010). Dynamic wildlife habitat models: Seasonal foods and mortality risk predict occupancy-abundance and habitat selection in grizzly bears. *Biological Conservation, 143*(7), 1623-1634.

Nielsen, S. E., Stenhouse, G. B., & Boyce, M. S. (2006). A habitat-based framework for grizzly bear conservation in Alberta. *Biological Conservation, 130*(2), 217-229.

Nieto, H., Sandholt, I., Aguado, I., Chuvieco, E., & Stisen, S. (2011). Air temperature estimation with MSG-SEVIRI data: Calibration and validation of the TVX algorithm for the Iberian Peninsula. *Remote Sensing of Environment, 115*(1), 107-116.

Nijland, W., Coops, N. C., Nielsen, S. E., & Stenhouse, G. (2015). Integrating optical satellite data and airborne laser scanning in habitat classification for wildlife management. *International Journal of Applied Earth Observation and Geoinformation, 38*(0), 242-250.

Nijland, W., Nielsen, S. E., Coops, N. C., Wulder, M. A., & Stenhouse, G. B. (2014). Fine-spatial scale predictions of understory species using climate- and LiDAR-derived terrain and canopy metrics. *Journal of Applied Remote Sensing, 8*.

Nilsson, M. (1996). Estimation of tree heights and stand volume using an airborne lidar system. *Remote Sensing of Environment, 56*(1), 1-7.

Olsson, C., & Jonsson, A. M. (2015). Budburst model performance: The effect of the spatial resolution of temperature data sets. *Agricultural and Forest Meteorology, 200*, 302-312.

Paneque-Galvez, J., McCall, M. K., Napoletano, B. M., Wich, S. A., & Koh, L. P. (2014). Small Drones for Community-Based Forest Monitoring: An Assessment of Their Feasibility and Potential in Tropical Areas. *Forests, 5*(6), 1481-1507.

Parmentier, B., McGill, B., Wilson, A. M., Regetz, J., Jetz, W., Guralnick, R. P., . . . Schildhauer, M. (2014). An assessment of methods and remote-sensing derived covariates for regional predictions of 1 km daily maximum air temperature. *Remote Sensing, 6*(9), 8639-8670.

Parmesan, C., & Yohe, G. (2003). A globally coherent fingerprint of climate change impacts across natural systems. *Nature, 421*(6918), 37-42.

Peckham, S. D., Ahl, D. E., & Gower, S. T. (2009). Bryophyte cover estimation in a boreal black spruce forest using airborne lidar and multispectral sensors. *Remote Sensing of Environment, 113*(6), 1127-1132.

Post, E., Pedersen, C., Wilmers, C. C., & Forchhammer, M. C. (2008). Warming, plant phenology and the spatial dimension of trophic mismatch for large herbivores. *Proceedings of the Royal Society B-Biological Sciences, 275*(1646), 2005-2013.

Prihodko, L., & Goward, S. N. (1997). Estimation of air temperature from remotely sensed surface observations. *Remote Sensing of Environment, 60*(3), 335-346.

R Development Core Team. (2012). R: A language and environment for statistical computing. Vienna, Austria: R Foundation for Statistical Computing. Retrieved from http://www.R-project.org

Rahman, M. M., Hay, G. J., Couloigner, I., Hemachandran, B., & Bailin, J. (2015). A comparison of four relative radiometric normalization (RRN) techniques for mosaicing H-res multi-temporal thermal infrared (TIR) flight-lines of a complex urban scene. *Isprs Journal of Photogrammetry and Remote Sensing, 106*(0), 82-94.

Rizzoli, A., Neteler, M., Rosà, R., Versini, W., Cristofolini, A., Bregoli, M., . . . Gould, E. A. (2007). Early detection of tick-borne encephalitis virus spatial distribution and activity in the province of Trento, northern Italy. *Geospatial health, 1*(2), 169-176.

Sims, D. A., Rahman, A. F., Cordova, V. D., El-Masri, B. Z., Baldocchi, D. D., Bolstad, P. V., . . . Xu, L. (2008). A new model of gross primary productivity for North American ecosystems based solely on the enhanced vegetation index and land surface temperature from MODIS. *Remote Sensing of Environment, 112*(4), 1633-1646.

Snyder, W. C., Wan, Z., Zhang, Y., & Feng, Y. Z. (1998). Classification-based emissivity for land surface temperature measurement from space. *International Journal of Remote Sensing, 19*(14), 2753-2774.

Soudani, K., le Maire, G., Dufrene, E., Francois, C., Delpierre, N., Ulrich, E., & Cecchini, S. (2008). Evaluation of the onset of green-up in temperate deciduous broadleaf forests derived from Moderate Resolution Imaging Spectroradiometer (MODIS) data. *Remote Sensing of Environment, 112*(5), 2643-2655.

StataCorp. (2013). Stata Statistical Software: Release 13. College Station, TX: StataCorp LP.

Stisen, S., Sandholt, I., Nørgaard, A., Fensholt, R., & Eklundh, L. (2007). Estimation of diurnal air temperature using MSG SEVIRI data in West Africa. *Remote Sensing of Environment, 110*(2), 262-274.

Streutker, D. R., & Glenn, N. F. (2006). LiDAR measurement of sagebrush steppe vegetation heights. *Remote Sensing of Environment, 102*(1–2), 135-145.

Sun, H., Chen, Y., Gong, A., Zhao, X., Zhan, W., & Wang, M. (2014). Estimating mean air temperature using MODIS day and night land surface temperatures. *Theoretical and Applied Climatology, 118*(1-2), 81-92.

Sun, Y. J., Wang, J. F., Zhang, R. H., Gillies, R. R., Xue, Y., & Bo, Y. C. (2005). Air temperature retrieval from remote sensing data based on thermodynamics. *Theoretical and Applied Climatology, 80*(1), 37-48.

Thomas, C. K., & Smoot, A. R. (2013). An Effective, Economic, Aspirated Radiation Shield for Air Temperature Observations and Its Spatial Gradients. *Journal of Atmospheric and Oceanic Technology, 30*(3), 526-537.

Tompalski, P., Coops, N. C., White, J. C., & Wulder, M. A. (2015). Enriching ALS-derived area-based estimates of volume through tree-level downscaling. *Forests, 6*(8), 2608-2630.

Tonini, F., Dillon, W. W., Money, E. S., & Meentemeyer, R. K. (2016). Spatio-temporal reconstruction of missing forest microclimate measurements. *Agricultural and Forest Meteorology, 218–219*, 1-10.

Vancutsem, C., Ceccato, P., Dinku, T., & Connor, S. J. (2010). Evaluation of MODIS land surface temperature data to estimate air temperature in different ecosystems over Africa. *Remote Sensing of Environment, 114*(2), 449-465.

von Arx, G., Dobbertin, M., & Rebetez, M. (2012). Spatio-temporal effects of forest canopy on understory microclimate in a long-term experiment in Switzerland. *Agricultural and Forest Meteorology, 166*, 144-155.

Wagenmakers, E.-J., & Farrell, S. (2004). AIC model selection using Akaike weights. *Psychonomic bulletin & review, 11*(1), 192-196.

Wan, Z., Zhang, Y., Zhang, Q., & Li, Z. L. (2004). Quality assessment and validation of the MODIS global land surface temperature. *International Journal of Remote Sensing, 25*(1), 261-274.

Wan, Z. M. (2008). New refinements and validation of the MODIS Land-Surface Temperature/Emissivity products. *Remote Sensing of Environment, 112*(1), 59-74.

Wan, Z. M., & Dozier, J. (1996). A generalized split-window algorithm for retrieving land-surface temperature from space. *IEEE Transactions on Geoscience and Remote Sensing, 34*(4), 892-905.

White, M. A., Running, S. W., & Thornton, P. E. (1999). The impact of growing-season length variability on carbon assimilation and evapotranspiration over 88 years in the eastern US deciduous forest. *International Journal of Biometeorology, 42*(3), 139-145.

Wiegand, T., Naves, J., Garbulsky, M. F., & Fernandez, N. (2008). Animal habitat quality and ecosystem functioning: Exploring seasonal patterns using NDVI. *Ecological Monographs, 78*(1), 87-103.

Williamson, S. N., Hik, D. S., Gamon, J. A., Kavanaugh, J. L., & Flowers, G. E. (2014). Estimating temperature fields from MODIS land surface temperature and air temperature observations in a sub-arctic alpine environment. *Remote Sensing, 6*(2), 946-963.

Williamson, S. N., Hik, D. S., Gamon, J. A., Kavanaugh, J. L., & Koh, S. (2013). Evaluating cloud contamination in clear-sky MODIS Terra daytime land surface temperatures using ground-based meteorology station observations. *Journal of Climate, 26*(5), 1551-1560.

Willmott, C. J. (1981). On the validation of models. *Physical Geography, 2*(2), 184-194.

WinSCANOPY canopy structure and solar radiation. (2006). Quebec City, Canada: Regent Instruments Inc.

Xu, Y., Knudby, A., & Ho, H. C. (2014). Estimating daily maximum air temperature from MODIS in British Columbia, Canada. *International Journal of Remote Sensing, 35*(24), 8108-8121.

Yochum, S. E., Bledsoe, B. P., Wohl, E., & David, G. C. L. (2014). Spatial characterization of roughness elements in high-gradient channels of the Fraser Experimental Forest, Colorado, USA. *Water Resources Research, 50*(7), 6015-6029.

You, G., Zhang, Y., Schaefer, D., Sha, L., Liu, Y., Gong, H., . . . Xie, Y. (2013). Observed air/soil temperature trends in open land and understory of a subtropical mountain forest, SW China. *International Journal of Climatology, 33*(5), 1308-1316.

Yu, W., Ma, M., Wang, X., Song, Y., & Tan, J. (2011). Validation of MODIS land surface temperature products using ground measurements in the Heihe River Basin, China. *Remote Sensing for Agriculture, Ecosystems, and Hydrology Xiii, 8174*.

Zakšek, K., & Schroedter-Homscheidt, M. (2009). Parameterization of air temperature in high temporal and spatial resolution from a combination of the SEVIRI and MODIS instruments. *ISPRS Journal of Photogrammetry and Remote Sensing, 64*(4), 414-421.

Zhu, W., Lu, A., & Jia, S. (2013). Estimation of daily maximum and minimum air temperature using MODIS land surface temperature products. *Remote Sensing of Environment, 130*, 62-73.

Zorer, R., Rocchini, D., Metz, M., Delucchi, L., Zottele, F., Meggio, F., & Neteler, M. (2013). Daily MODIS land surface temperature data for the analysis of the heat requirements of grapevine varieties. *IEEE Transactions on Geoscience and Remote Sensing, 51*(4), 2128-2135.

Chapter Four: An Open-Source Method of Constructing Cloud-Free Composites of Forest Understory Temperature Using MODIS

4.1 Abstract

Surface air temperature (T_{air}) is a critical driver of ecosystem processes and phenological dynamics, and can be estimated in near-real time with satellite remote sensing. However, persistent cloud cover often creates large spatial and temporal gaps in our observation records. Previous studies have successfully mapped T_{air}, however, the challenges of mapping forest understory temperatures (T_{ust}) are relatively unexplored. This study describes a methodology for constructing cloud-free composites of T_{ust} at 250 m spatial resolution. We used generalized linear models to correlate daily average T_{ust} with ground-surveyed forest structural characteristics and land surface temperature (LST) obtained from the Moderate Resolution Imaging Spectroradiometer (MODIS). Models were applied to all four daily MODIS overpasses and combined in to a single image to maximize cloud-free spatial coverage. Pixel temperatures within the remaining cloud gaps were estimated using a temporal averaging algorithm that incorporated a novel approach for factoring the relative cloudiness between days. Models predicted T_{ust} to within 1.5°C ($R^2 \sim 0.87$), with an overall final map accuracy having a mean absolute error of 2.2°C. Maps were produced for two growing seasons using in situ observation data from forested sites throughout the Rocky Mountains of Alberta, Canada. By avoiding complex physical models, our procedure is computationally efficient and capable of processing large volumes of data using open-source programming languages and desktop computers.

4.2 Introduction

Surface air temperature (T_{air}) is a fundamental metric for modelling ecosystem processes and monitoring global climate change (Parmesan *et al.*, 2013). For ecological models in particular, T_{air} is essential for explaining niche extents (Morin and Thuiller 2009), vegetation phenology and the timing of species interactions (Nielsen *et al.*, 2010). Ongoing shifts in global climate conditions necessitate predictions of how species will respond to these changes (Buckley *et al*., 2010), and spatially continuous maps of T_{air} are instrumental for making such projections.

Over the past few years, thermal data collected from satellite platforms have been used to estimate T_{air} at regional and global extents (e.g. Kloog *et al.*, 2014). While this remote-sensing approach is both accurate and efficient, it is regularly hampered by cloud cover obscuring the Earth's surface from the sensor (Lu *et al.*, 2011), especially in mountainous regions (Neteler 2010). Furthermore, many temperature-driven ecological events occur beneath the forest canopy, out of view from these space-borne sensors. Because of these challenges, spatially and temporally continuous estimations of understory temperature (T_{ust}) have yet to be realized.

The Moderate Resolution Imaging Spectroradiometer (MODIS) provides thermal-infrared data in the form of Land Surface Temperature (LST) imagery with an accuracy of < 1 K (Wan *et al.*, 2002). The sensor is carried onboard NASA's EOS sun-synchronous, near-polar orbiting *Terra* and *Aqua* satellites; with *Aqua* in an ascending orbit and *Terra* in a descending orbit, having two daily equatorial crossings each at 13:30, 01:30 and 10:30, 22:30, respectively (local solar time) (Williamson *et al.*, 2013). Clouds produce *NoData* gaps in the LST imagery, which create spatially and temporally punctuated datasets.

Because of this, many applications using MODIS imagery tend to be restricted to clear-sky conditions (Jang *et al.*, 2014). The daily LST product is combined in to 8- and 16-day composites to mitigate data loss from clouds, but this aggregation alters the relationship between T_{air} and LST (Willamson *et al.*, 2014). When using LST composites to monitor seasonal temperature accumulations, or growing degree days (GDDs), the intervals may be too coarse to identify brief temperature anomalies or short-lived ecological events such as plant budburst. Therefore, using the daily LST product to estimate T_{air} is often the best temporal resolution for GDD applications (Neteler 2010).

A number of previous studies have attempted to resolve the problem of cloud-gaps in daily LST imagery. For example, Lu *et al.* (2011) used geostationary infrared satellites to measure LST in overcast conditions to obtain a root mean square error (RMSE) of 5°C. Similar accuracies were attained by Jang *et al.* (2014), who used brightness temperature retrievals from the Advanced Microwave Scanning Radiometer for the Earth Observing System to estimate under-cloud temperatures. Crosson *et al.* (2012) estimated sub-cloud-gap temperatures in one MODIS overpass using clear pixels from another overpass that same day. Similarly, Huang *et al.* (2015) used all four daily MODIS overpasses to increase spatial coverage by up to 35%. Perhaps the most comprehensive gap-filling methodology was developed by Neteler (2010) and expanded by Metz *et al.* (2014). This technique uses both spatial and temporal averaging combined with an interpolation of regression residuals to obtain highly accurate reconstructed LST values (mean absolute difference not exceeding 1.41 K) at an enhanced spatial resolution of 250 m. There is an opportunity to combine the finest aspects of these existing methodologies to produce cloud-free composites of T_{ust}: a key microclimate that is rarely explored through remote sensing.

T_{air} is measured at the top of the vegetation surface, above the forest canopy where it exists. The objective of this chapter was to create a mapped time series of average daily sub-canopy T_{ust} uninterrupted by cloud gaps. We employ a methodology that merges all four daily MODIS overpasses into a single image to maximize spatial coverage. The remaining gaps are filled using a weighted temporal-averaging algorithm that features a novel coefficient that adjusts for relative cloudiness between days. To our knowledge, there is no literature that has worked to map T_{ust} using MODIS LST. The entire methodology was automated using the statistical programming language R (R Core Team 2014) and scripts developed in the Python 2.7 environment (van Rossum and Drake 2001). This effort to reconstruct T_{ust} specifically is motivated by our involvement in an ongoing grizzly bear (*Ursus arctos*) research program where we are working to monitor critical habitat for this threatened species (https://friresearch.ca/program/grizzly-bear-program). The resulting T_{ust} maps will ultimately be used to calculate GDDs to model understory plant phenology and the timing of nutrition available for bears.

4.3 Methods

4.3.1 Study Area and T_{ust} Observation Plots

The 125000 km^2 study area is located along the Rocky Mountain foothills of western Alberta, Canada (Figure 4.2). In situ T_{ust} was observed in 29 broadly dispersed observation plots located at near-regular latitude intervals from 49°N to 55°N. These observations were used to derive regression coefficients and to validate the final T_{ust} maps. Plots were placed along an elevation gradient to encompass an array of temperature variability. This distribution also ensured a diverse range of terrain, canopy closure and forest composition

types. Plots were 250 x 250 m in size and located within homogenous forest stands. Within each plot, four sub-canopy Thermochron sensors placed in solar radiation shields recorded hourly temperature over two growing seasons: 2011 and 2012.

4.3.2 MODIS LST pre-processing

The daily 1 km MODIS LST product (Aqua MYD11A1; Terra MOD11A1; level V005) were obtained from the NASA Land Processes Distributed Active Archive Center (LP DAAC) along with their coincident local solar view times and pixel quality assessment flags (QA). MODIS Reprojection Tool software (MRT v4.1) converted the imagery from Sinusoidal to 1 km gridded geotiffs in Universal Transverse Mercator projection using nearest neighbour resampling. Pixels with a LST error less than 3 K and an average emissivity error of less than 0.02 were selected (Benali *et al.*, 2012). Although this is not the highest available pixel quality, it extended the spatial LST coverage, but increased the potential for outliers. These cloud-altered outliers typically appear in the negative degree Celsius range (Metz *et al*., 2014). Using a method similar to Neteler (2010), we eliminated potential outliers by removing pixels that were one standard deviation below the average minimum ground temperature for that month. We then closed new and existing single-pixel *NoData* gaps using a custom local high-pass filter. Each image was converted to binary where all valid LST values equaled 1 and *NoData* pixels equaled 0. A moving window then gave each pixel the sum of its adjacent pixels, therefore any pixel with a value of ‘8’ was identified as a solitary pixel gap. These gaps were then filled with the average of the surrounding original LST values.

4.3.3 Spatially Extending the T_{ust} Models

Regressions are the most popular statistical approach to estimate T_{air} from MODIS LST. Their efficiency is desirable, since it is so difficult to take into consideration all of the complex factors required to formulate a reliable physical model (Mostovoy *et al.*, 2006). The relationship between LST and T_{ust} was established by correlating in situ understory temperatures with all clear-sky instantaneous measurements from MODIS. To obtain exact overpass times a longitudinal correction was made for each ground plot and image solar view times were converted to local view times (±30 s), with corrections for daylight savings (Williamson *et al.*, 2014). We then performed a 1 km proximity search around each observation plot where any adjacent pixel having more than a 5 K difference was considered corrupted (i.e. from cloud vapour) and not used in the model (Neteler 2010). Generalized linear models were used to estimate average daily T_{ust} from each of the four daily MODIS overpasses (StataCorp 2013). Random effects were used to offset bias from using multiple temperature observations within single plots. A crosscorrelation between explanatory variables ensured no collinearity within models. A total of 4153 day and night clear-sky observations were made during the study period, 20% of these data were randomly withheld for validation.

Model covariates were selected based on their recognized influence on understory temperature (Chapter 3; Laskin *et al.*, 2016). Canopy closure and forest stand type (characterized as the proportion of conifer trees) were chosen since both occupy the transitional space between the understory and supracanopy air masses. They were measured in situ every 50 m along two 250 m stratified-random linear transects per plot (14 sub-plots). Canopy closure was quantified using five hemispherical photographs per

sub-plot and later processed with Regent Instruments WinSCANOPY software (Version 2006c). Time-of-year has been found to be important in estimating T_{air} (Coops *et al.*, 2007), therefore Julian day (quadratic polynomial) was used to express growing season duration (Benali *et al.*, 2012). Environmental lapse rate varies substantially with altitude, therefore elevation was added as a covariate (10 m photogrammetrically compiled DEM) (Rhee and Im 2014). All explanatory variables were produced as rasters for the extent of the study area to generate the T_{ust} maps. Canopy closure and percent conifer maps for the study area were previously modelled at 30 m Landsat resolution using nearly 1000 ground-truth locations (Linke *et al.*, 2009). The regression models were extended from the plot level to the study area extent for each of the four daily pre-processed LST images. During this step, the estimates of T_{ust} were spatially enhanced to 250 m using the higher-resolution covariate rasters (i.e. elevation) to augment the 1 km LST data (Zorer *et al.*, 2013). Enhancement through spatial interpolation (Neteler 2010) was considered too computationally intensive for the desktop computers used in this research. The four daily estimations of average T_{ust} at 250 m resolution were then merged into a single image to increase the cloud-free coverage, averaging T_{ust} values wherever there was any overlap.

4.3.4 Temporal Gap Filling

The remaining cloud gaps in the imagery were filled using a temporal-averaging method adapted from Metz *et al.* (2014), who suggested that temporal interpolation is the best option to fill large spatial gaps. Interpolation using neighbouring clear pixels may provide values that are not representative of the landscape directly underlying the cloudy pixels, especially in spatially heterogeneous areas like mountains. Similar to spatial correlation,

days closer in time will tend to have similar temperatures than those more temporally distant (Jin and Dickinson 2000). Based on this concept, an algorithm was developed to search the 7-days preceding and following a date with a cloud gap. A Gaussian average was then used to impart more weight to dates closer in time to the gap being filled.

Metz *et al.* (2014) state that persistent cloud cover is the main source of inaccuracy in reconstructed LST maps because lower temperatures beneath persistent cloud cover will always be overestimated. This is because temporal averaging will fill gaps using values from days usually having much less cloud cover. Therefore we developed a novel and straightforward method to factor the relative cloudiness between days during temporal averaging. A *cloudiness* coefficient was derived from a simple regression correlating the average cloudiness over the study area at the time of overpass with the in situ daily maximum T_{ust} using the AQUA 13:30 dataset. This midday dataset was chosen because of the increased likelihood of interaction between irradiance and cloud cover. The coefficient modifies the temporal average based on the comparative cloudiness of days within the ±7 day window to avoid overestimating the reconstructed cloud-gap temperatures.

In some cases, the temporal window of ±7 days was not enough to fill gaps created by persistent cloud. This only occurred in small areas at the beginning and end of the growing season in the high alpine. These were filled by determining the elevation of a particular *NoData* pixel and allocating it the average value of all other T_{ust} pixels at that same elevation. If there were no other usable pixels at that elevation, another search was made 100 m lower or until available pixels were found. Adjustments for the difference in lapse rates were performed using an average of the dry and wet rates, or 0.8°C/100 m. The procedural flow is summarized in Figure 4.1.

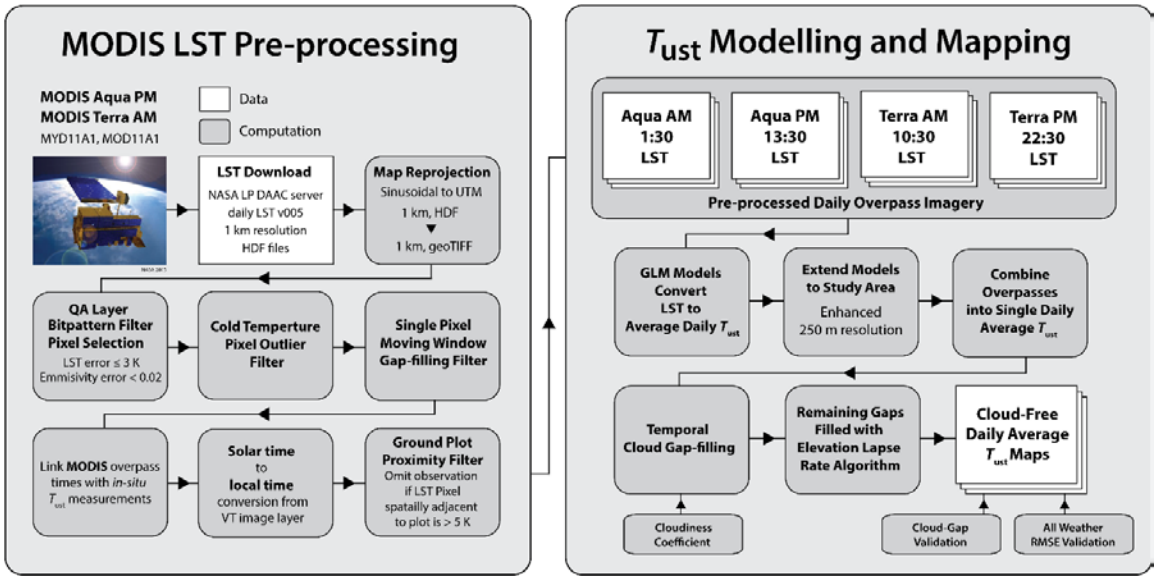

Figure 4.1 Simplified flow chart of the understory temperature (T_{ust}) composite mapping procedure.

4.4 Results

The T_{ust} models for each overpass produced a mean absolute error (MAE) of less than 1.5°C (Table 4.1). This accuracy exceeds many previous pixel-scale T_{air} estimates (e.g. Xu *et al.*, 2014, MAE = 2.41°C) and is similar to others (e.g. Vancutsem *et al.* 2010, MAE = 1.73°C). Model fit expressed by the coefficient of determination (R^2 = 0.85 – 0.88) was also comparable to previous studies such as Niclos *et al.* (2014, R^2 = 0.88) and Zhu *et al.* (2013, R^2 = 0.86). There was very low bias in all of the models suggesting that any estimation error likely arises from the quality of the original LST product. LST and the quadratic polynomial of Julian day explained the majority of variability in average daily T_{ust}. Canopy closure worked to predict daytime overpasses while percent conifer was more significant at night – likely due to slight diurnal changes between latent and sensible heat flux and forest type (Parmentier *et al.*, 2014).

Table 4.1 **Plot-scale regression estimates of average daily T_{ust}.**

Model	R^2	MAE (°C)	RMSE (°C)	Bias (°C)	LST β	Jday β	Jday^2 β	Elev β	CC β	PC β
AQUA 13:30	0.85	1.39	1.79	0.03	0.56 (0.15)*	0.24 (0.15)*	-0.0006 (<0.0000)*	-0.0018 (0.0005)*	0.005 (0.01)	
AQUA 1:30	0.89	1.40	1.79	0.39	0.75 (0.023)*	0.13 (0.02)*	-0.0004 (<0.0000)*	-0.001 (0.0007)		-0.008 (0.005)
TERRA 10:30	0.87	1.37	1.76	0.03	0.56 (0.01)*	0.24 (0.01)*	-0.0006 (<0.0000)*	-0.002 (0.0005)*	-0.009 (0.01)	
TERRA 22:30	0.88	1.48	1.99	-0.12	0.72 (0.02)*	0.12 (0.01)*	-0.0003 (<0.0000)*	0.0007 (0.0005)		-0.01 (0.004)*

Coefficients (β) and Standard errors (in parentheses) are presented by model for MODIS LST (LST), Julian day (Jday), elevation (Elev), canopy closure (CC), and conifer percentage (PC). Coefficient of determination (R^2), Mean absolute error (MAE), Root mean square error (RMSE). Standard null: LST+Jday+Jday^2. *Statistical significance at $p < 0.05$.

The correlation between cloudiness and T_{ust} was attenuated for all overpass times except AQUA 13:30 with a model fit of $R^2 = 0.37$. Between April and September a 10% increase in cloud cover will decrease maximum in situ T_{ust} by approximately 1°C (Coefficient $\beta = 0.09$). A validation of the cloud-gap algorithm was performed on 10% of the imagery by randomly selecting locations where all four daily T_{ust} images overlap. A 10 km diameter hole was clipped out of each image to simulate a cloud gap, filled using the temporal average algorithm, and then compared with the original pixel values. The *cloudiness* coefficient worked well in some situations but not others which ultimately produced slight improvement in T_{ust} estimates opposed to using no factor for relative cloudiness between days at all.

The final cloud-free T_{ust} maps (Figure 4.2) for both growing seasons were validated using 1500 randomly selected, all-weather in situ observations (20% of the total) to produce an overall map accuracy of MAE = 2.2°C (RMSE = 3.0°C, BIAS = -1.1°C).

Comparing the daily map T_{ust} estimates against the corresponding in situ values shows consistent correlation over a broad range of temperatures and elevations throughout the study area (Figure 4.3).

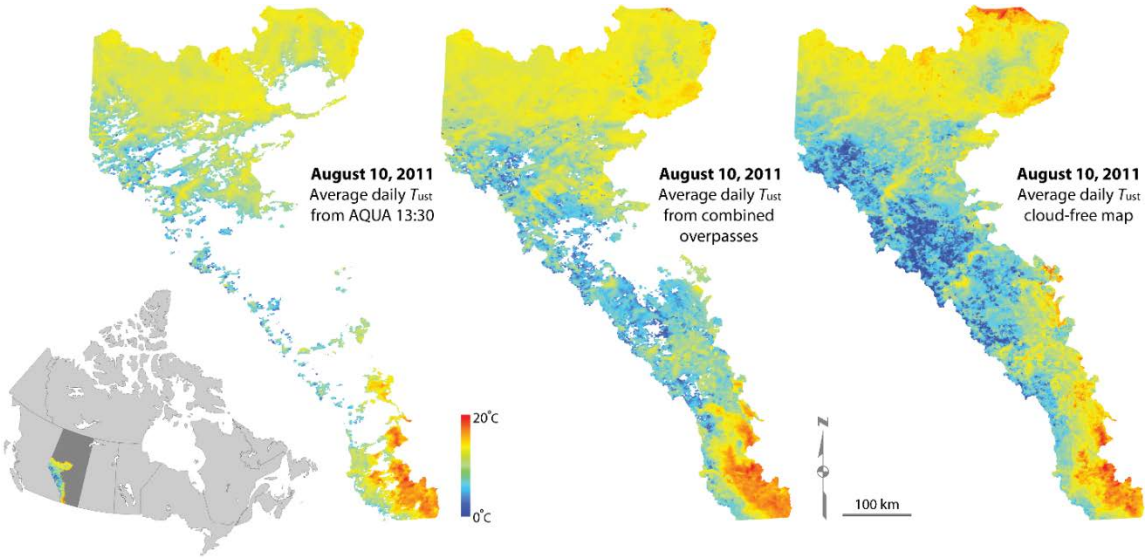

Figure 4.2 Example of removing cloud gaps beginning with a single overpass image (left), increasing coverage by combining all four daily overpasses (centre), and lastly the gap-filled, cloud-free average T_{ust} map. Study area extent shown in inset. Cool regions of the map correspond with high alpine areas.

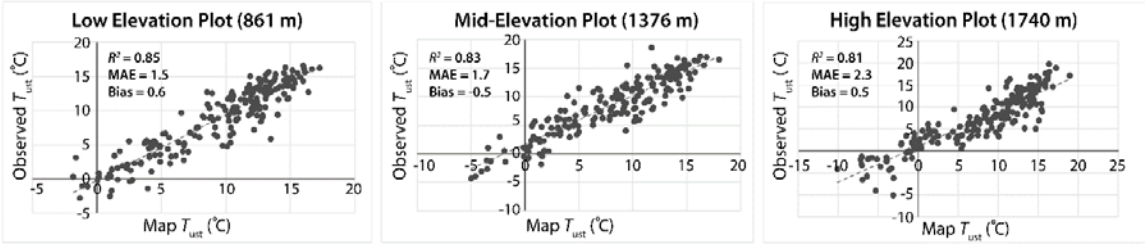

Figure 4.3 Correlation between average daily in situ T_{ust} observations vs. map T_{ust} values at three representative elevations for a single growing season.

4.5 Discussion and Conclusion

This study demonstrates a procedure to create cloud-free maps of daily average understory temperature. The methodology expands upon the previous work of others, chiefly Metz *et al.* (2014) and Neteler (2010), but with the intention of using these maps to monitor ecosystem processes specifically beneath the forest canopy. The overall accuracy of the final T_{ust} maps is analogous to Huang *et al.* (2015) who used a similar method of merging four daily images combined with spatio-temporal gap-filling to produce a T_{air} map accuracy of MAE = 1.84°C and RMSE = 2.41°C. Direct comparisons of different study results can be potentially misrepresentative due to disparities in land cover and topographic complexity. The mountainous landscape of this study area introduced numerous mapping challenges, notably up to 2 weeks of unabating cloud cover in certain areas – considering this obstacle, our estimations of T_{ust} were remarkably accurate.

The novel *cloudiness* coefficient used to improve the temporal averaging estimates worked very well during single site trials, but over larger extents and time periods produced inconsistent results. It was highly effectual at increasing the weighted average temperature from very cloudy days to match T_{ust} in the cloud gap, but was too aggressive in decreasing clear-day averages to match gap temperatures on partly cloudy days. This indicates that there are certainly more factors affecting the relationship between cloudiness and T_{ust}, which is likely more temporally contextual than a direct instantaneous correlation. For example, T_{ust} estimates could be biased by an underlying trend in the cloudiness of the imagery stack. Knowing that annual seasonal variation affects T_{air} estimates (Zhang *et al.*, 2011), it would be ideal to produce a coefficient specifically for each month, or better yet, generate one that is effective year-round. Metz *et al.* (2014) stated that surface temperatures

reconstructed from remote-sensing data will always overestimate areas beneath clouds. LST temporal composites also tend to overestimate GDDs because only the clear day temperatures within the composite period are registered (Hassan *et al.*, 2007). However, the T_{ust} maps developed in this study showed a slight underestimation of T_{ust}, indicated by the negative bias of the residuals; an effect of the cloudiness coefficient excessively *cooling* the gap-filled values. Regardless, not overestimating cloud-gap values demonstrates the benefit of adjusting for cloudiness during image reconstruction to improve overall accuracy. It would be worthwhile to strive for an optimal coefficient which produces no estimation bias under all conditions. Correspondingly, it would also be beneficial to perform a sensitivity analysis on the number of days required to calculate the best temporal average for a single date.

This image-reconstruction method was intended to be streamlined by avoiding complex physical models and using open-source programming languages on desktop computers. In a multi-step analysis such as this one, automation increases efficiency while reducing human error (Tuck *et al.*, 2014). The estimated computational time from initially pinging the NASA FTP to having an entire year of reconstructed daily cloud-free imagery is less than 1 week. MODIS LST data are usually made available for download a few days after image acquisition (Wan 2014). This relatively rapid turnover is ideal for 'real-time' seasonal applications such as monitoring phenological response to climate change (Inouye 2008), habitat quality assessments for grizzly bears (Nielsen *et al.*, 2003) or predicting wildfires (Flannigan *et al.*, 2000). This methodology is a successful prototype which can be made more efficient to reduce computational time, and eventually be developed in to a stand-alone toolbox for use in any application where maps of T_{ust} or T_{air} are required.

4.6 References

Benali, A., Carvalho, A. C., Nunes, J. P., Carvalhais, N., & Santos, A. (2012). Estimating air surface temperature in Portugal using MODIS LST data. *Remote Sensing of Environment, 124*(0), 108-121.

Buckley, L. B., Urban, M. C., Angilletta, M. J., Crozier, L. G., Rissler, L. J., & Sears, M. W. (2010). Can mechanism inform species' distribution models? *Ecology Letters, 13*(8), 1041-1054.

Coops, N. C., Duro, D. C., Wulder, M. A., & Han, T. (2007). Estimating afternoon MODIS land surface temperatures (LST) based on morning MODIS overpass, location and elevation information. *International Journal of Remote Sensing, 28*(10), 2391-2396.

Crosson, W. L., Al-Hamdan, M. Z., Hemmings, S. N. J., & Wade, G. M. (2012). A daily merged MODIS Aqua-Terra land surface temperature data set for the conterminous United States. *Remote Sensing of Environment, 119*, 315-324.

Flannigan, M. D., Stocks, B. J., & Wotton, B. (2000). Climate change and forest fires. *Science of the total environment, 262*(3), 221-229.

Hassan, Q. K., Bourque, C. P. A., Meng, F. R., & Richards, W. (2007a). Spatial mapping of growing degree days: an application of MODIS-based surface temperatures and enhanced vegetation index. *Journal of Applied Remote Sensing, 1*(1): 013511-013511.

Huang, R., Zhang, C., Huang, J. X., Zhu, D. H., Wang, L. M., & Liu, J. (2015). Mapping of daily mean air temperature in agricultural regions using daytime and nighttime land surface temperatures derived from TERRA and AQUA MODIS data. *Remote Sensing, 7*(7), 8728-8756.

Inouye, D. W. (2008). Effects of climate change on phenology, frost damage, and floral abundance of montane wildflowers. *Ecology, 89*(2), 353-362.

Jang, K., Kang, S., Kimball, J. S., & Hong, S. Y. (2014). Retrievals of all-weather daily air temperature using MODIS and AMSR-E data. *Remote Sensing, 6*(9), 8387-8404.

Jin, M., & Dickinson, R. E. (2000). A generalized algorithm for retrieving cloudy sky skin temperature from satellite thermal infrared radiances. *Journal of Geophysical Research: Atmospheres (1984–2012), 105*(D22), 27037-27047.

Kloog, I., Nordio, F., Coull, B. A., & Schwartz, J. (2014). Predicting spatiotemporal mean air temperature using MODIS satellite surface temperature measurements across the Northeastern USA. *Remote Sensing of Environment, 150*, 132-139.

Laskin, D., Montaghi, A., Nielsen, S., & McDermid, G. (2016). Estimating understory temperatures using MODIS LST in mixed cordilleran forests. *Remote Sensing, 8*(8), 658.

Linke, J., McDermid, G. J., Laskin, D. N., McLane, A. J., Pape, A., Cranston, J., . . . Franklin, S. E. (2009). A disturbance-inventory framework for flexible and reliable landscape monitoring. *Photogrammetric Engineering and Remote Sensing, 75*(8), 981-995.

Lu, L., Venus, V., Skidmore, A., Wang, T., & Luo, G. (2011). Estimating land-surface temperature under clouds using MSG/SEVIRI observations. *International Journal of Applied Earth Observation and Geoinformation, 13*(2), 265-276.

Metz, M., Rocchini, D., & Neteler, M. (2014). Surface temperatures at the continental scale: tracking changes with remote sensing at unprecedented detail. *Remote Sensing, 6*(5), 3822-3840.

Morin, X., & Thuiller, W. (2009). Comparing niche- and process-based models to reduce prediction uncertainty in species range shifts under climate change. *Ecology, 90*(5), 1301-1313.

Mostovoy, G. V., King, R. L., Reddy, K. R., Kakani, V. G., & Filippova, M. G. (2006). Statistical estimation of daily maximum and minimum air temperatures from MODIS LST data over the State of Mississippi. *Giscience & Remote Sensing, 43*(1), 78-110.

Neteler, M. (2010). Estimating daily land surface temperatures in mountainous environments by reconstructed MODIS LST data. *Remote Sensing, 2*(1), 333-351.

Niclos, R., Valiente, J. A., Barbera, M. J., & Caselles, V. (2014). Land surface air temperature retrieval from EOS-MODIS images. *IEEE Geoscience and Remote Sensing Letters, 11*(8), 1380-1384.

Nielsen, S. E., Boyce, M. S., Stenhouse, G. B., & Munro, R. H. M. (2003). Development and testing of phenologically driven grizzly bear habitat models. *Ecoscience, 10*(1), 1-10.

Nielsen, S. E., McDermid, G., Stenhouse, G. B., & Boyce, M. S. (2010). Dynamic wildlife habitat models: Seasonal foods and mortality risk predict occupancy-abundance and habitat selection in grizzly bears. *Biological Conservation, 143*(7), 1623-1634.

Parmentier, B., McGill, B., Wilson, A. M., Regetz, J., Jetz, W., Guralnick, R. P., . . . Schildhauer, M. (2014). An assessment of methods and remote-sensing derived covariates for regional predictions of 1 km daily maximum air temperature. *Remote Sensing, 6*(9), 8639-8670.

Parmesan, C., Burrows, M. T., Duarte, C. M., Poloczanska, E. S., Richardson, A. J., Schoeman, D. S., & Singer, M. C. (2013). Beyond climate change attribution in conservation and ecological research. *Ecology Letters, 16*, 58-71.

R Development Core Team. (2012). R: A language and environment for statistical computing. Vienna, Austria: R Foundation for Statistical Computing. Retrieved from http://www.R-project.org

Rhee, J., & Im, J. (2014). Estimating high spatial resolution air temperature for regions with limited in situ data using MODIS products. *Remote Sensing, 6*(8), 7360-7378.

StataCorp. (2013). Stata Statistical Software: Release 13. College Station, TX: StataCorp LP.

Tuck, S. L., Phillips, H. R. P., Hintzen, R. E., Scharlemann, J. P. W., Purvis, A., & Hudson, L. N. (2014). MODISTools - downloading and processing MODIS remotely sensed data in R. *Ecology and Evolution, 4*(24), 4658-4668.

van Rossum, G., & Drake, F. L. (2001). Python Reference Manual, PythonLabs, Virginia, USA, 2001. *Available online at:(accessed 1 December 2012).*

Vancutsem, C., Ceccato, P., Dinku, T., & Connor, S. J. (2010). Evaluation of MODIS land surface temperature data to estimate air temperature in different ecosystems over Africa. *Remote Sensing of Environment, 114*(2), 449-465.

Wan, Z. (2014). New refinements and validation of the collection-6 MODIS land-surface temperature/emissivity product. *Remote Sensing of Environment, 140*, 36-45.

Wan, Z. M., Zhang, Y. L., Zhang, Q. C., & Li, Z. L. (2002). Validation of the land-surface temperature products retrieved from Terra Moderate Resolution Imaging Spectroradiometer data. *Remote Sensing of Environment, 83*(1-2), 163-180.

Williamson, S. N., Hik, D. S., Gamon, J. A., Kavanaugh, J. L., & Flowers, G. E. (2014). Estimating temperature fields from MODIS land surface temperature and air temperature observations in a sub-arctic alpine environment. *Remote Sensing, 6*(2), 946-963.

Williamson, S. N., Hik, D. S., Gamon, J. A., Kavanaugh, J. L., & Koh, S. (2013). Evaluating cloud contamination in clear-sky MODIS Terra daytime land surface temperatures using ground-based meteorology station observations. *Journal of Climate, 26*(5), 1551-1560.

Xu, Y., Knudby, A., & Ho, H. C. (2014). Estimating daily maximum air temperature from MODIS in British Columbia, Canada. *International Journal of Remote Sensing, 35*(24), 8108-8121.

Zhang, L. W., Huang, J. F., Guo, R. F., Li, X. X., Sun, W. B., & Wang, X. Z. (2013). Spatio-temporal reconstruction of air temperature maps and their application to estimate rice growing season heat accumulation using multi-temporal MODIS data. *Journal of Zhejiang University-Science B, 14*(2), 144-161.

Zhu, W., Lu, A., & Jia, S. (2013). Estimation of daily maximum and minimum air temperature using MODIS land surface temperature products. *Remote Sensing of Environment, 130*, 62-73.

Zorer, R., Rocchini, D., Metz, M., Delucchi, L., Zottele, F., Meggio, F., & Neteler, M. (2013). Daily MODIS land surface temperature data for the analysis of the heat requirements of grapevine varieties. *IEEE Transactions on Geoscience and Remote Sensing, 51*(4), 2128-2135.

Chapter Five: A Remote Sensing Framework for Mapping the Phenology of Plant Resources Used by Grizzly Bears and Projecting the Impacts of Climate Change

5.1 Abstract

Bottom-up trophic linkages in seasonal latitudes are largely driven by the timing of vegetation development, which is in turn controlled by temperature and climate. Monitoring these seasonal processes are invaluable for many applications, including the production of dynamic food-driven species-occurrence models that are based on the availability of plant resources. In addition, the ability to forecast phenological processes is doubly important during this period of rapid global change. Satellite imagery provides an efficient means of obtaining broad-scale phenological data, but forest understories are relatively overlooked because of the difficulty in resolving individual phenophases (e.g. fruiting) from spaceborne platforms. We developed a framework to produce high-temporal-resolution phenology maps of understory plants using satellite-derived understory air temperature (T_{ust}). We used an extensive remote camera network to observe daily phenology of a fruiting perennial shrub (*Shepherdia canadensis*) and a perennial leguminous taproot (*Hedysarum alpinum*) in the southern Rocky Mountains of Canada. These plants are critical sources of nutrition for grizzly bear (*Ursus arctos*) populations in the region. The phenology maps predicted the timing of fully ripe fruit with a mean absolute error (MAE) of 2.4 days, with an average accuracy for all 12 reproductive phenophases of MAE equal to 5.2 days. Our models were used to explore the projected impacts of climate change on the timing of ecologically relevant phenophases within the study area for two end-of-century warming scenarios. There were considerable advances in the timing of peak

fruiting of 6.6 days per °C. These shifts in fruit development were confirmed through experimental warming in climate-controlled growth chambers. With daily global coverage of thermal satellite imagery, our methods provide a framework for near-real-time monitoring of plant-food phenology in understory microclimates nearly anywhere, and a foundation for projecting the spatio-temporal impacts of climate change.

5.2 Introduction

Phenology is an integrative environmental science used to monitor and predict the timing of recurrent biological events related to climate such as wildlife migrations, or the flowering and fruiting of plants (Post and Inouye 2008). Climate is the main factor controlling and regulating phenological events in plants because of their physiological reliance on temperature (Reeves and Coupland 2000). As a result, changes in plant phenology have been one of the first observed impacts of climate change (Root *et al*., 2003). Plants are especially appropriate organisms to examine the effects of climate change because they are sessile and must exhibit a range of phenotypic plasticity to tolerate fluctuating temperatures (MacDonald and Chinnappa 1989; Gordo and Sanz 2010). This adaptation, expressed through changing phenology, is shifting forward under climate change (Paremsan and Yohe 2003; Parmesan 2006). Advance in the timing of spring onset ranges between 2.5 days per °C on average, to over a week per °C in some species (Chmielewski and Rötzer 2002; Walther *et al*., 2002; Badeck *et al*., 2004; Menzel *et al*., 2006). The anticipated impacts of changing vegetation phenology include shifts in floral and faunal species distributions (Pearson and Dawson 2003; Thomas *et al*., 2004), altered habitat-use and movement of large mobile fauna (Hebblewhite *et al*., 2008; Post *et al*.,

2008; Middleton *et al*., 2013), and the decoupling of trophic interactions known as trophic mismatch (Blois *et al*., 2013; Edwards and Richardson 2004). With these changes already underway and projected warming to be as high as +7°C by the end of this century (IPCC 2014), representations of vegetation phenology in present-day and future ecosystem models is essential (Chuine and Beaubien 2001; Richardson *et al*., 2012; Morellato *et al*., 2016).

The majority of species occurrence models currently rely almost entirely on static habitat-quality indices, such as landscape pattern, and do little to incorporate species movement and dynamic mechanistic variables such as the timing of critical food resources (Benz *et al*., 2016). It is crucial to incorporate phenological information into these models that coincides with the inherently dynamic habitat-use of mobile species (Nielsen *et al*., 2010). This need becomes more important in response to current environmental change, providing insight into inter-seasonal vegetation phenology patterns, species interactions, and trends over time. Forecasts of climate change impacts are critical for species conservation and management (Buckley *et al*., 2010). However, for most terrestrial biomes, there is no detailed knowledge of how climate change will affect the scale and interaction of phenological processes (Garcia *et al*., 2014). To determine the extent of these impacts, modeling efforts need to integrate future projections of spatial shifts in plant species distributions and temporal shifts in their phenology (Chuine 2010; Kearney *et al*., 2010).

As a model variable, broad-scale phenological metrics related to land-surface phenology can now be efficiently acquired through time-series satellite remote sensing (Zhang *et al*., 2003). The combination of inclusive ground coverage and regularly repeated observations provide global phenological monitoring that is not possible by any other

means (Cleland *et al*., 2007). When examining bottom-up drivers of habitat use by herbivores and omnivores, food availability is a key predictor of species occurrence (Nielsen *et al*., 2016). General vegetative food abundance can be inferred through satellite-derived vegetation indices such as the Normalized Difference Vegetation Index (NDVI) (Pettorelli *et al*., 2006). This approach works well for predicting fundamental phenophases such as spring onset, end of season, and seasonal maximums for a given location (Coops *et al*., 2012; Kobayashi *et al*., 2016). However, these metrics are generally quite coarse and linking these indices to discrete, species-specific phenophases on the ground remains a challenge (Nijland *et al.*, 2016). This becomes even more of a challenge when attempting to discriminate phenology in forest understories, which cannot be directly observed by the sensor overhead. One approach to this problem is to use a thermal-based index to exploit the linkage between temperature and plant development (Hassan *et al*., 2007). Temperature accumulations, or growing degree days (GDD) have been extensively applied in agriculture to predict crop development (McMaster and Wilhelm 1997), but their functionality in forest understory phenology is relatively unexplored.

Surface air temperature (T_{air}) is a driver of phenological timing and related ecosystem processes, especially in seasonal latitudes (White *et al*. 1999). T_{air} can be estimated from remotely sensed thermal imagery at regional and global extents (e.g. Kloog *et al*., 2014). The Moderate Resolution Imaging Spectroradiometer (MODIS) acquires thermal infrared imagery in the form of Land Surface Temperature (LST) with an accuracy of < 1 K (Wan *et al*., 2002). This sensor makes four daily overpasses aboard two satellite platforms, the rapid temporal resolution makes MODIS suitable for deriving detailed seasonal temperature accumulations for broad-scale phenology mapping (e.g. Hanes and

Schwartz 2011). Unfortunately cloud cover creates spatially and temporally punctuated datasets (Jang *et al*., 2014). As a result, the daily LST imagery is combined into 8- and 16-day composites to mitigate this data loss. These composite periods are often too temporally coarse to distinguish short-lived phenological events common to mountainous regions and temperate latitudes (de Beurs and Henebry 2010; Coops *et al*., 2007). Capturing the exact date of these events, such as the sudden appearance of fruit, requires daily observations during the growing season (Crimmins and Crimmins 2008).

LST is the temperature of the surfaces directly visible to the sensor overhead. Therefore the relationship between LST and T_{air} needs to be determined using a supplementary estimation technique, which is commonly statistical (e.g. Niclos *et al*., 2014; Vancutsem *et al*., 2010). This modeling process requires corroborating in situ observations of T_{air} on the ground, which are commonly obtained by standard meteorological stations or atop eddy covariance flux towers (e.g. Sims *et al*., 2008). De Frenne and Verheyen (2016) explain that although climate warming is clearly evident from weather station data, we know very little of how temperatures are changing beneath the forest canopy. This is because nearly all weather stations follow the World Meteorological Organization's guidelines that sensors should be placed a certain distance away from trees (Jarraud 2008). Canopy modified temperatures in the understory drive phenological processes at different rates than the macroclimates beyond the forest (De Frenne *et al*., 2013). Given the predicted sensitivity of North American forests to climate change (Charney *et al*., 2016), added consideration should be given to the dynamics occurring within them.

5.2.1 Grizzly Bear Plant Foods

The forests of western Canada provide cover and forage for an abundance of species, including the grizzly bear (*Ursus arctos*). These large mammals have generalist life histories predicated to omnivory, however the populations in the southern Rocky Mountains have diets comprised predominantly of vegetation (Hildebrand *et al*., 1999; McLellan 2011). Their habitat-use is spatially and temporally diverse, as they strategically exploit a wide variety of plant species that provide peak nutrition at differential times of the growing season (Nielsen *et al*., 2003). Of the broad number of seasonal plant species on which grizzly bears forage, some are more critical food sources than others. Canada buffaloberry (*Shepherdia canadensis*) is a widespread perennial shrub that fruits in late summer, providing grizzlies with a significant amount of calories necessary for winter denning (Pearson 1975; Hamer and Herrero 1987) (Figure 5.1). Alpine sweet vetch (*Hedysarum alpinum*) is a herbaceous legume with a nutrient-rich perennial taproot that offers quality forage for bears soon after waking from hibernation (Coogan et al., 2012).

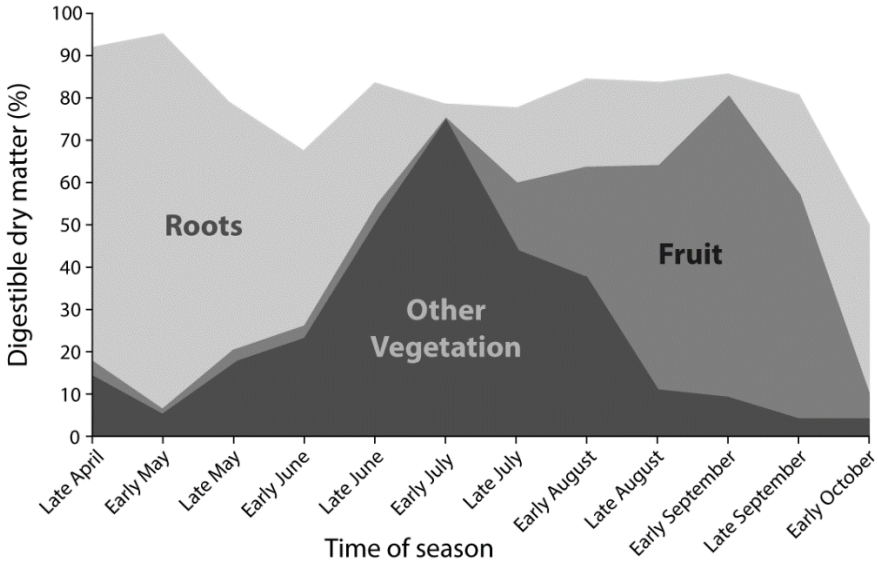

Figure 5.1 Typical seasonal progression of vegetation consumed by grizzly bears in the central Rocky Mountains of Alberta represented by percent digestible dry matter derived from scat samples. Perennial taproots such as *H. alpinum* are critical in early spring while fruits, such as the berries of *S. canadensis*, are a significant caloric source in late summer and early autumn. (Figure adapted from Bater *et al*. (2011) using data from Munro *et al*. (2006), Table 2).

Grizzly bears are listed as a threatened species in Alberta, Canada, as a result of reduced population numbers due to increased anthropogenic mortality, elevated long-term stress, and habitat loss through fragmentation (Festa-Bianchet and Kansas 2010; MacBeth 2010; Clark and Slocombe 2011). These stresses may be exacerbated as climate change portends to disrupt their precise foraging regimen by altering the timing and distribution of nutrition across their habitat, particularly in confined mountainous regions (Roberts *et al*., 2014; Lambers 2015). Food availability is a critical component of grizzly bear habitat quality (Braid *et al*., 2016), therefore phenology maps of critical bear foods will assist managers in developing food-driven occurrence models for this threatened population of bears (Nielsen *et al*., 2003). Temporal heterogeneity in the arrival of food resources has

been shown to be potentially more important to consumer energy gain than overall resource abundance (Armstrong *et al*., 2016). This phenological *schedule* is directly applicable to reducing bear-human conflict or the creation of ecological traps by anticipating the arrival of bears in food-rich areas (e.g. Lamb *et al*., 2016).

5.2.2 Objectives

The emphasis of landscape phenology research has largely been on the timing of spring onset and budburst, since these events are effective indicators of climate change (Schwartz *et al*., 2012; Ryu *et al*., 2014; White *et al*., 2014). However, there has been little attempt to map the complete phenological progression of understory species over large areas. An approach is required for monitoring daily phenological development of understory plants using satellite-derived understory temperature. Mapping temporally discrete phenophases provides a mechanism for isolating ecologically critical events on the landscape such as nutrition availability.

The primary research objective was to develop a framework for mapping the individual phenophases of understory plant species using understory air temperature (T_{ust}) derived from MODIS LST. For a focal species, we selected the fruiting shrub *S. canadensis*, with a discussion on the extensibility of the framework using *H. alpinum*, which is less discrete in its phenology and therefore more challenging to characterize. The maps were validated by comparing predictions of peak nutrition availability against in situ observations on the ground. Our secondary objective involved projecting the effects of climate change on phenophase timing in *S. canadensis* and *H. alpinum* under future warming scenarios. With the broad availability of thermal satellite imagery, this framework

provides near-real-time monitoring of vegetation phenology in understory microclimates nearly anywhere, and a strategy for projecting the spatiotemporal impacts of climate change.

5.3 Materials and Methods

5.3.1 Study Area

The study area extends along the front ranges of the Rocky Mountains in western Alberta, Canada. It encompasses the extent of grizzly bear range within the province, covering nearly 125,000 km^2 of predominantly forested land cover from 49°N to 55°N. The region is comprised of three distinct natural subregions: the foothills, montane, and subalpine (Figure 5.2). These ecological units are defined by landscape pattern, notably vegetation, as a result of the combined influence of climate, topography, and geology (Downing and Pettipiece 2006). The lower foothills have deciduous stands of trembling aspen (*Populus tremuloides*), balsam poplar (*Populus balsamifera*) and mixed forests with white spruce (*Picea glauca*). The upper foothills and subalpine are dominated by mature conifer forests of lodgepole pine (*Pinus contorta*) and Engelmann spruce (*Picea engelmannii*). The montane is located along low front-range slopes and the bottom of major river valleys which provide critical movement corridors for grizzly bears and many other species. Here, trembling aspen, lodgepole pine, and Douglas fir (*Pseudotsuga menziesii*) stands occur at lower elevations, while the upper montane is covered by mixed and lodgepole pine forests. In situ phenology was observed in 45 broadly distributed plots at near-regular latitudinal intervals throughout the study area. Plots were placed along an elevation gradient to

encompass an array of temperature variability and to capture a range of terrain, canopy closure, and forest composition types (Lessard-Therrien *et al*., 2014).

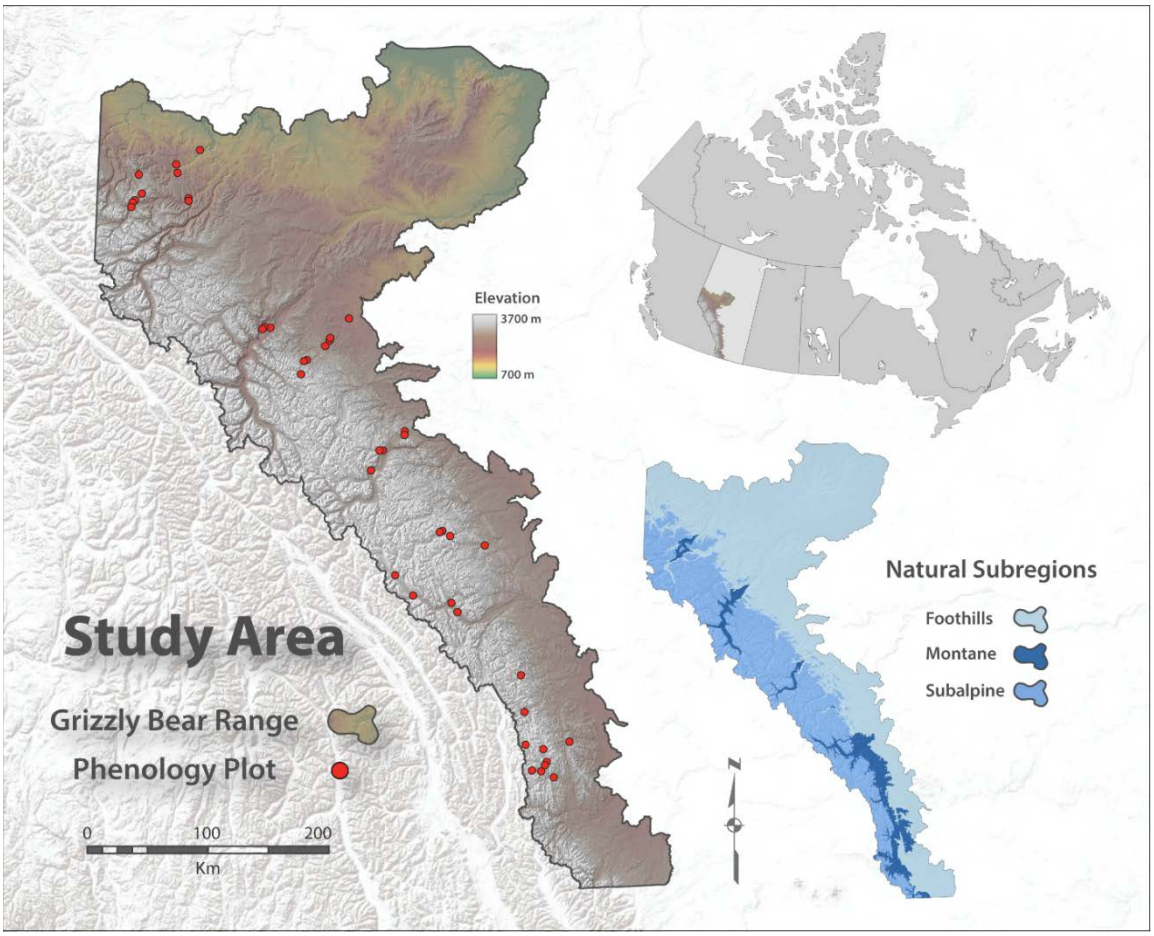

Figure 5.2 The study area is defined by the present-day extent of grizzly bear range in Alberta, Canada. It encompasses three unique ecological subregions: the foothills, montane, and subalpine.

5.3.2 Phenology Observations

A digital camera network of 85 Wingscapes PlantCams® was distributed throughout the study area for two growing seasons in 2011 and 2012. Within each plot at least one plant (female) was imaged three times daily at solar noon by one or two cameras. The focus

species was *S. canadensis* because of its critical nutritional importance for bears, widespread distribution, and visually distinct phenophases. Observations were made of the structural-physical reproductive phenology and assigned a discrete designation based on the current stage of development (Table 5.1). The phenophases were based on those developed by Dierschke (1972), but modified to better-suit the purposes of this framework.

Table 5.1 Reproductive phenophases of Canada buffaloberry (*Shepherdia canadensis*), adapted from Dierschke (1972).

Reproductive Phenophases of *S. canadensis*	
1. Beginning to flower	7. First ripe fruit
2. 50% in bloom	8. 25% ripe fruit
3. Full bloom	9. 50% ripe fruit
4. Fading	10. Fully ripe fruit
5. Completely faded	11. Bearing overripe fruit
6. Bearing green fruit	12. Dispersal

Sub-canopy air temperature accumulations were recorded at hourly intervals using Thermochron® temperature loggers (Maxim Integrated Products, Sunnyvale, CA, USA) placed within solar radiation shields 1 m above ground; the approximate height of shrubby vegetation. Twenty nine of the 45 plots were 250 x 250 m (6.25 ha) in size in an attempt to unify observation scales on the ground with the satellite imagery (Misra *et al*., 2016). These plots were located within broad homogenous forest stands, with four additional sensors placed in a grid to record the average temperature within the stand. Field visits were made by personnel at 10-day intervals to corroborate the camera imagery and to make phenological observations of the surrounding 6.25 ha plots. Previous analysis found that there was no significant difference between the phenophase of a single camera-plant

pairing and plants of the same species in the surrounding plot (Chapter 2; Laskin and McDermid 2016).

5.3.3 The Phenology Mapping Framework

A procedural flow chart of the complete phenology mapping framework is presented in Figure 5.3. The framework is comprised of three major methodological components which are outlined here and described in detail in the following subsections. The first and most extensive being the *air temperature modeling* component which works to bridge the gap between canopy-top observations of LST and the underlying T_{ust}. When LST is used to estimate air temperature, what is typically derived is T_{air} which is the temperature of the air mass directly above the surface visible to the sensor, in this case the forest canopy. There is a difference between T_{air} and T_{ust} because of the modifying effects of the canopy structure, forest type, near-surface environmental lapse rates, and distance from the ground (Hanes and Schwartz 2011). A more comprehensive modeling approach is required to incorporate these canopy and forest characteristics in order to accurately estimate T_{ust} (Chapter 3; Laskin *et al*., 2016a). This air temperature modeling component also includes a methodology to extend estimates of T_{ust} across the study area by incorporating a procedure to effectively remove cloud contamination from the imagery time-series (Chapter 4; Laskin *et al*., 2016b).

The next major component of the framework undertakes the *baseline phenology mapping* which translates the thermal accumulations, required to transition the target species from one phenophase to the next, in to the T_{ust} maps. These accumulations are compiled through the T_{ust} map times-series of the study area to derive the present-day, or

baseline, understory phenology maps. The final component derives the *climate scenario maps* by modifying the baseline maps using two current Intergovernmental Panel on Climate Change (IPCC) emissions scenarios to project the impacts of warming onto existing patterns of understory phenology. The two scenarios encompass the expected range of temperature variability anticipated between the years 2080-2100. The moderate warming scenario (B1) has a projected average temperature increase of 1.8°C, and the aggressive warming scenario (A2) projects an increase of 3.4°C. Experimental warming of *S. canadensis* was also undertaken in this component of the framework to determine the calculable phenological response of this species to climate warming.

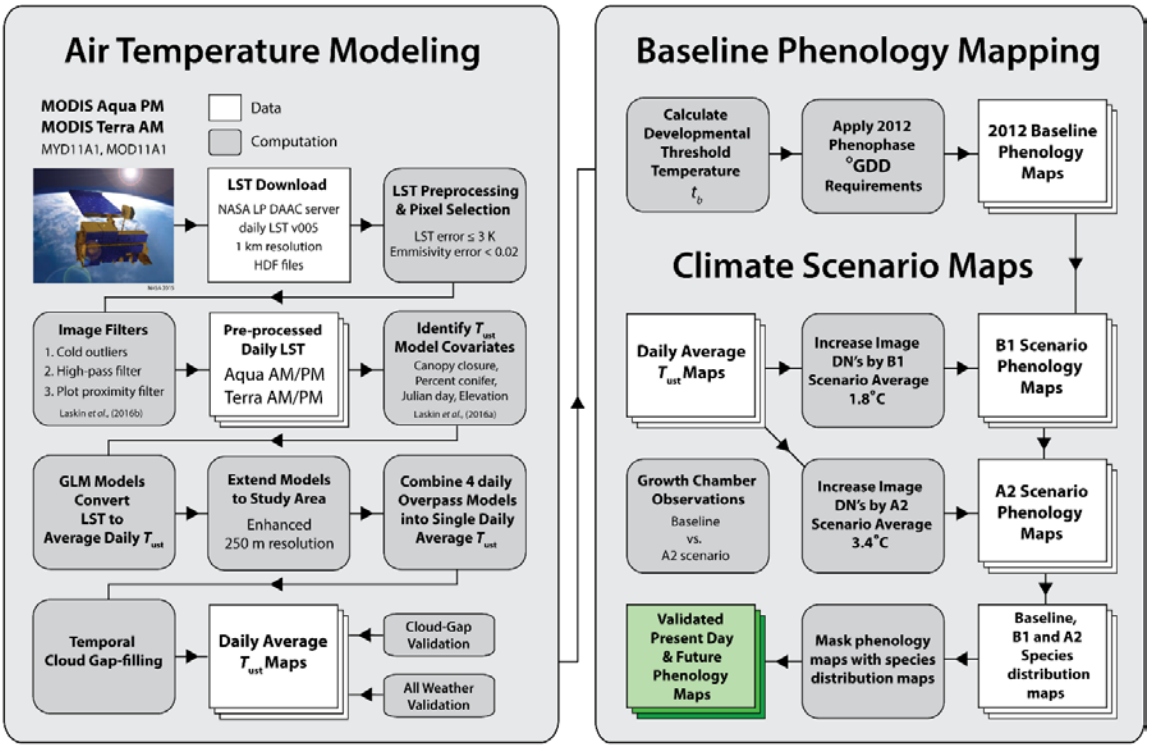

Figure 5.3 Procedural flow chart of the phenology mapping framework. The methodology is comprised of three major components: (i) modeling understory air temperature (T_{ust}), (ii) deriving present-day baseline phenology maps, and (iii) deriving projected phenology maps based on two future warming scenarios, moderate B1 and aggressive A2 (IPCC 2014).

5.3.4 Air Temperature Modeling Using MODIS LST

MODIS LST imagery (Terra MOD11A1; Aqua MYD11A1) does not measure T_{air} directly, but rather the skin temperature of the surfaces visible to the sensor (Sun *et al.*, 2005). The relationship between LST and T_{air} is consequently determined using a supplementary estimation technique (Mostovoy *et al.*, 2006). LST is sensitive to land cover and vegetation density, with more accurate LST estimations occurring in areas of dense vegetation (Vancutsem *et al.*, 2010; Mildrexler *et al.*, 2011). Regressions have been used to accurately model T_{air} (e.g. Zorer *et al.*, 2013; Niclos *et al.*, 2014; Xu *et al.*, 2014), and more recently

T_{ust} (Chapters 3, 4; Laskin *et al*., 2016a, 2016b). The central modeling challenge being that the microclimates in which *S. canadensis* predominantly inhabit are below the forest canopy out of view from the sensor. Laskin *et al*. (Chapter 3; 2016a) was an initial endeavor in estimating T_{ust} using instantaneous measurements of LST at the plot scale (at the exact moment of MODIS overpass). Here generalized liner models (GLM) were derived in STATA 13 statistical software (StataCorp 2013) to estimate values of T_{ust}. Random effects were used to offset bias from repeated temperature observations within single sites. The daily 1 km LST product is collected by NASA's EOS sun-synchronous, near-polar orbiting Terra and Aqua satellites; with Aqua in an ascending orbit and Terra in a descending orbit, having two daily equatorial crossings each at 13:30, 01:30, and 10:30, 22:30, respectively (local solar time) (Williamson *et al*., 2013). In addition to LST, model covariates included: Julian day, elevation above sea level (10 m DEM), canopy closure (%), forest stand type (characterized as the proportion of conifer trees), and a suite of LiDAR-derived canopy metrics. Canopy closure and the proportion of conifer were measured in situ every 50 m (14 sub-plots) along two 250 m stratified-random linear transects within the 6.25 ha plots. Canopy closure was measured during leaf-on conditions using five hemispherical photographs at each sub-plot and later processed with WinSCANOPY software (Version 2006c). A representative sample of trees species was obtained using a 360° *sweep* of each sub-plot using wedge prism relascopes.

Along with LST, canopy closure and proportion of conifer explained a significant portion of variability in T_{ust} since they occupy the transitional space between the understory and supracanopy air masses. Time-of-year, expressed by the quadratic polynomial of Julian day, explained over 20% of the variability in T_{ust}. Elevation was also a significant variable

since environmental lapse rates vary substantially with altitude. The highest elevation a plant species can occupy is usually limited by fulfilling fruit maturation before encountering a killing frost, but this is likely to change under future climates (Morin *et al*., 2007). A LiDAR-derived standard deviation of canopy height metric was also found to improve estimations of T_{ust} over LST alone, however this variable was sporadically available across the study area and could not be used for spatially extending the models. A total of 4153 day and night clear-sky observations were made during the study period and 20% of these data were randomly withheld for validation. Understory temperature within the observation plots, during clear skies, was predicted to within a mean absolute error (MAE) of 1.4°C with an overall model fit of $R^2 = 0.89$.

Laskin *et al*. (Chapter 4; 2016b) developed a procedure to extend these instantaneous estimates into spatially continuous, cloud-free daily average T_{ust} maps over the entire study area. Generalized linear models were again used to estimate average daily T_{ust} from each of the four daily MODIS overpasses (within 1.5°C, $R^2 \sim 0.87$). Firstly within the plots to estimate the model coefficients and then these were extended to the study area. All of the explanatory variables existed as raster surfaces for the extent of the study area allowing the extension of these models into wall-to-wall phenology maps. Canopy closure and percent conifer maps for the study area were previously modelled at 30 m Landsat resolution using nearly 1000 ground-truth locations (Linke *et al*., 2009). During this step, the estimates of T_{ust} were spatially enhanced to 250 m using the higher-resolution covariate rasters (i.e., elevation) to augment the 1 km LST data (Zorer *et a*l., 2013). The four daily estimates of average T_{ust} at 250 m resolution were then merged into a single image to increase cloud-free coverage, averaging T_{ust} values wherever there was any overlap. On

average, only 23% of the site overpasses occurred in clear-sky conditions. Haung *et al*. (2015) found that merging all four daily overpasses can increase useable pixel coverage by approximately 35%. The remaining cloud-gaps were filled using a Gaussian weighted temporal interpolation using clear-sky values from the ±7 days preceding and following the current image (Neteler 2010; Metz *et al*., 2014). The final daily T_{ust} averages were compared to 20% randomly selected daily in situ averages from all weather conditions to produce a final map accuracy of 2.2°C.

5.3.5 Growing Degree Days and Developmental Threshold Temperature Calculation

Temperature accumulation provides a common reference for phenological development, this is because the amount of heat required to advance from one life cycle stage to the next generally does not change (Reáumur 1735). Thermal time is often expressed in growing degree days (GDD), which are much better for predicting phenological events compared to other approaches such as time-of-year or number-of-days (Hunter and Lechowicz 1992; Cesaraccio *et al*., 2001). Plant species have unique minimum and maximum base temperatures below or above which physiological development does not occur. Once these thresholds are determined it is then possible to establish a reference point to commence GDD accumulations (AGDD) (Wang 1960; Miller *et al*., 2001; Črepinšek *et al*., 2006). After the base temperature has been surpassed, there is a direct relationship between air temperature and the rate of plant development (Snyder *et al.*, 1999). There are a variety of techniques for calculating GDD (Snyder 1985; Roltsch *et al.*, 1999), but the principle form of the equation is as follows (McMaster and Wilhelm 1997) (Equation 5.1):

$$°\text{GDD} = \left[\frac{T_{\max} + T_{\min}}{2}\right] - t_{\text{b}} \qquad \text{(Equation 5.1)}$$

where T_{max} and T_{min} are the temperature extremes reached in a single 24-hour period, and t_b is the base temperature, or minimum physiological temperature threshold. It is typical to choose a base temperature of either 0°C or 5°C average daily temperature, however this is variable between species (Wielgolaski 1999). For this study, threshold temperatures were derived using a statistical approach recommended by Yang *et al.* (1995) called the *regression method*, originally developed by Hoover (1955). A statistical threshold temperature is derived by minimizing the standard deviation in AGDD between phenophases over a series of observations. The regression method was used to obtain the developmental threshold using observations from across the study area and within the growth chambers. The methodology employed by Yang *et al*. (1995) as described by Snyder *et al*. (1999) begins by defining one season of phenological observations of a single plant as a *case*, and the total GDD, or $[f_i(t_b)]$, as a function of the threshold temperature (t_b) for the i_{th} case as (Equation 5.2):

$$f_i(t_b) = (T_i - t_b)d_i \qquad \text{(Equation 5.2)}$$

here, T_i is the sum of the daily mean temperatures divided by the number of days in the i_{th} case (d_i), and t_b is the base threshold temperature. The resulting GDD values are plotted against the daily mean temperatures during the corresponding phenophases. The threshold value is found by iterating until the slope of the regression equals zero and solving for t_b (Equation 5.3):

$$t_b = \frac{\sum T_i \sum d_i T_i - n \sum d_i T_i^2}{\sum d_i \sum T_i - n \sum d_i T_i} \qquad \text{(Equation 5.3)}$$

The threshold temperature was calculated to be 0°C ± 0.6°C in both the field and growth-chamber case observations. The AGDD were then quantified for each discrete phenophase start date in the seasonal progression (Figure 5.4).

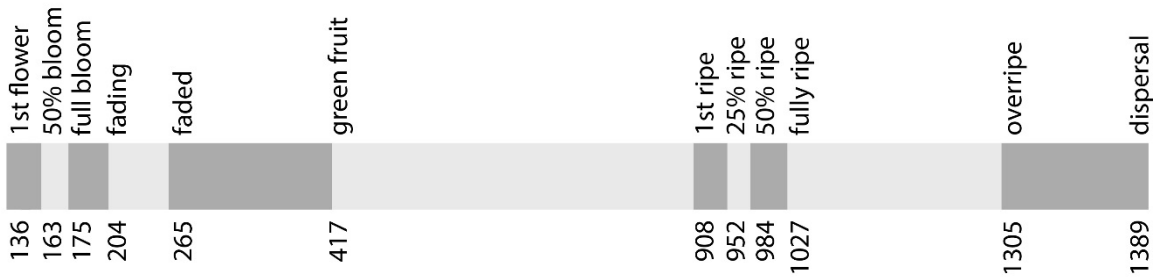

Figure 5.4 The t_b (threshold temperature) = 0° AGDD requirements for reproductive phenophases of *Shepherdia canadensis* shown against the relative average temporal phenophase duration.

5.3.6 Phenology Map Development

The baseline year of 2012 was selected to characterize the present-day phenological timing within the study area and represents the baseline climate scenario. Of the two years of field observations, 2012 was also closest in average temperature to the 35-year study area average (within 0.33°C). This was confirmed using spatially continuous monthly temperature from NOAA's North American Regional Reanalysis (NARR) dataset. Daily average T_{ust} maps were produced from the beginning of February, well before any location reached average temperatures above freezing, until the end of October. The production of the phenology maps was semi-automated using scripts developed in the statistical programming language R (R Core Team 2014) and the Python 2.7 environment (Van

Rossum and Drake 2001). The GDD equation (5.1) was applied to a T_{ust} map producing an output of the daily accumulations above the threshold temperature up to that date (Figure 5.5). These maps were then classified based on the AGDD required to begin each phenophase. The final product being a time series of the complete phenological progression of *S. canadensis* across the study area.

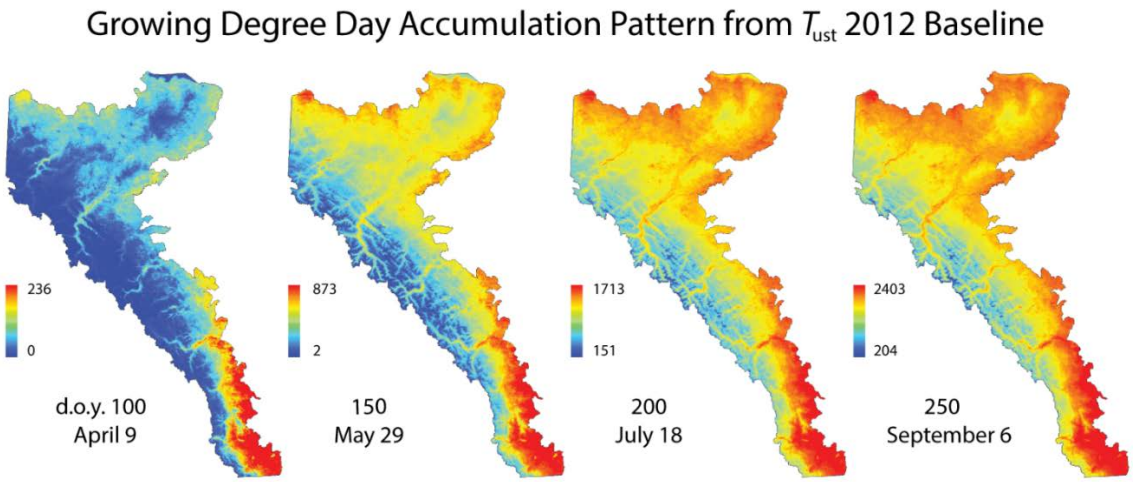

Figure 5.5 Example intervals (day of year) of the seasonal accumulated growing degree days (AGDD) derived from the daily average understory temperature (T_{ust}) imagery at 250 m spatial resolution. Cool regions of the map correspond with high-relief alpine and subalpine regions.

5.3.7 Map Validation

The phenology maps were derived using GDD accumulations calculated from field observations in 2011 and validated using a separate dataset of observations made at 16 new plots in 2012. The maps were validated by calculating the MAE between the map-predicted start date of each phenophase and the actual start date observed at each individual plant (pixel-scale). A paired t-test was used to determine if there was a significant

difference between the map predictions and observed in situ phenophases. Average phenophase start dates were calculated for the entire study area and for each natural subregion to derive regional comparisons between predicted start dates and observations on the ground.

5.3.8 Future Climate Scenarios

The IPCC Fifth Assessment Report (AR5) currently provides the most comprehensive scenarios of global future climate. However, some uncertainty still persists in these model given the inherent variability within the climate system itself, and particularly at local scales (Knutti and Sedlácek 2013). The study area is expected to become warmer and drier in the south and wetter in the north along the boreal boundary. How these changes will manifest in the mountains is difficult to project due to confounding factors such as topography and elevation. These multivariate regional complexities, including precipitation irregularities, are difficult to incorporate into the phenology projections. Since the framework assumes temperature as the controlling factor of plant phenology, only temperature variability was considered in the projections. Two IPCC emission scenarios were selected to bracket the projected range of future warming. The moderately warming B1 scenario and the aggressively warming A2 scenario have anticipated average increases of 1.8°C and 3.4°C respectively by the year 2100 (IPCC 2014). In order to investigate the potential effects of warming on the development of *S. canadensis*, these values were added to the baseline T_{ust} time series imagery to create the corresponding scenarios within the study area. The AGDD were recalculated for both scenarios using the same developmental threshold temperature (t_b = 0°C), and reclassified using the same phenophase GDD

requirements. Future warming is expected to alter phenological timing, but also the spatial distribution of the plants themselves as they exploit new niches made available by novel climates (Elith and Leathwick 2009). Present and future species habitat distribution maps for *S. canadensis* were developed by Roberts *et al*. (2014) by merging eight individual ecological niche models in to an averaged ensemble. The models were based on a future climate grid over the study area derived from 14 general-circulation model outputs averaged across the years 2071 to 2100. The phenology maps were masked using the corresponding distribution maps for all three scenarios: the 2012 baseline, B1, and A2. It is assumed that *S. canadensis* is not in a state of transition or adaptation, but that observed patterns in the projections reflect the species full biotic potential by occupying all environmentally suitable areas (Barry and Elith 2006).

5.3.9 Growth Chamber Observations

Phenological response to temperature changes can be confounded by other factors such as photoperiod cues (Clark *et al*., 2014). Experimental warming can be used to forecast the effects of climate change while reducing these sources of uncertainty (e.g. Norby *et al*., 2003; Sherry *et al*., 2007; Kopp and Cleland 2015). Warming experiments establish an observable phenological response in an otherwise hypothetical future climate. Marchin *et al*. (2016) found that growth chambers produced identical phenological timing to what plants expressed naturally through interannual temperature variation. This implies that species phenology in the future will likely be equivalent to what can be observed through experimental warming. Fully enclosed climate-controlled growth chambers were used to simulate future warming and monitor shifts in the timing of peak nutrition (fully ripe

berries) in *S. canadensis*. The temperature profile set as the control was established on 30 year averages from an Environment Canada weather station located near the center of the study area at 1100 m elevation. The warming profile was based on the A2 scenario with a projected warming range between 2.0°C - 5.2°C which was added to the control profile with a maximum difference of 5°C by mid-season.

Two observation 'seasons' were performed using 20 plants in 2013 and 26 in 2014 proportionately divided and assigned randomly into the *baseline control* and *A2 scenario* chambers. Each plant was monitored daily by a PlantCam® and additional intermittent digital SLR imagery. Four visually distinct phenophases were selected for observation to maximize temporal precision and bookend the critical reproductive phenology of this species: first flower, full bloom, first ripe, and fully ripe. To ensure fruit production, male plants were placed in each chamber and used to hand-pollenate each flower in lieu of insects during full bloom. All plants were simultaneously cold-stratified for five months preceding chamber observations at a constant temperature of -5°C. Lighting intensity was calibrated and kept constant within the chambers with diurnal and seasonal photoperiod corresponding to mid-latitude of the study area (Way 2015). Moisture levels and watering schedules were also kept as consistent as possible.

5.4 Results

5.4.1 Baseline Phenology Maps

The framework effectively worked to accurately map the complete daily phenological development of *S. canadensis* across the study area (Figure 5.6). The maps estimated all phenophase start dates, on average, with an accuracy of less than two days (Table 5.2). The

average difference in timing of peak nutrition (fully ripe berries) in the study area was approximately one day. At the pixel scale, the maps predicted peak nutrition in individual plants with a mean absolute error (MAE) of 2.4 days. There was no significant difference between the phenophase timing in the maps and ground observations for *S. canadensis* (t = -0.08; p = 0.937; Correlation = 0.986).

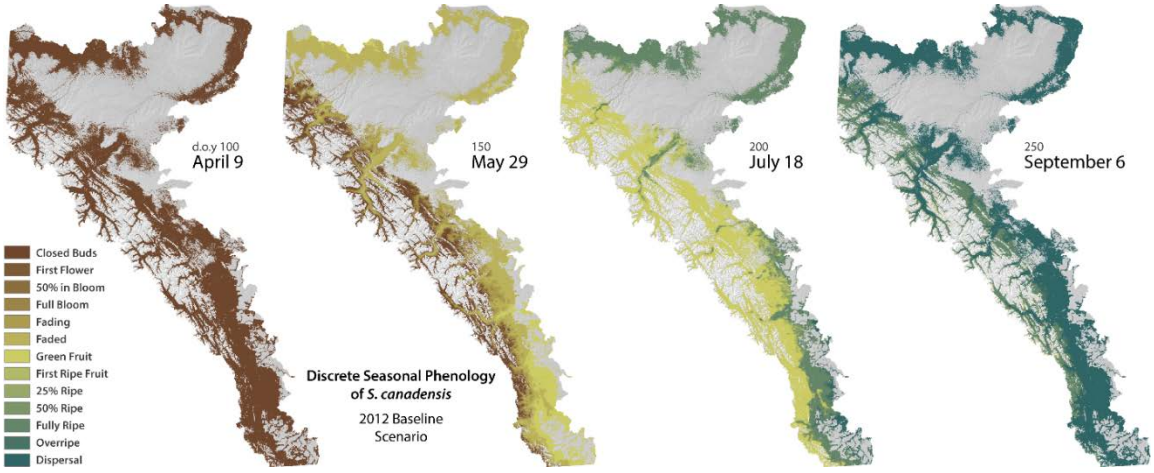

Figure 5.6 Distribution and seasonal progression of discrete phenophases of *Shepherdia canadensis* across the study area in the baseline year 2012, or present day scenario. Arbitrary intervals used to portray developmental rate over time (day of year).

The accuracy of the maps is consistent through the natural subregions with the highest overall variability in average phenophase onset being in the foothills at 5.2 days and the lowest in the subalpine at 2.3 days. The difference in duration between the first observable phenophase, first flower, and fully ripe was 1.9 days, and remained consistently accurate through the individual subregions. Overripe and dispersal had relatively poor accuracies (Table 5.2), suggesting that our current understanding of the drivers of senescence is limited and likely extends beyond air temperature (Keenan and Richardson

2015). With the exception of these end-of-season phenophases, the overall accuracy of the maps is outstanding.

Table 5.2 *Shepherdia canadensis* baseline map start dates (day of year) validated against in situ ground observations. Average start dates by phenophase and the difference between them (in days) are shown for the entire study area, individual subregions, and the mean absolute error (MAE) in days at the pixel-scale. Negative values indicate an underestimation by the map. Fully Ripe is highlighted to indicate the timing of peak nutrition. The lowermost row displays the overall duration between the beginning of flowering and peak nutrition.

	Study Area			Foothills			Montane			Subalpine			
	Map	Ground	Difference	Map	Ground	Difference	Map	Ground	Difference	Map	Ground	Difference	Pixel MAE
1st Flower	133.8	134.6	-0.8	125.0	128.0	-3.0	133.5	133.4	0.1	143.3	144.3	-1.0	3.7
50% Bloom	136.9	136.9	0.0	128.0	131.5	-3.5	136.2	134.9	1.3	147.5	147.3	0.3	3.7
Full Bloom	138.4	139.2	-0.7	129.8	134.5	-4.8	137.8	136.4	1.4	148.8	150.8	-2.0	4.1
Fading	142.1	143.4	-1.3	133.3	138.8	-5.5	141.6	140.8	0.8	152.3	154.8	-2.5	3.7
Completely Faded	150.0	149.9	0.8	140.3	145.0	-4.8	149.8	145.8	4.0	160.3	161.8	-1.5	4.3
Green Berries	168.7	174.0	-5.4	153.5	163.8	-10	170.0	174.4	-4.4	181.3	184.0	-2.8	8.3
1st Ripe Berry	206.5	206.0	0.5	191.0	195.7	-4.7	206.8	204.0	2.8	217.8	217.8	0.0	4.0
25% Ripe	209.1	207.7	1.4	193.3	196.3	-3.0	209.4	205.0	4.4	220.3	221.0	-0.8	3.6
50% Ripe	211.4	209.5	1.9	195.3	197.0	-1.7	211.6	207.4	4.1	223.0	222.5	0.5	3.0
★ Fully Ripe	214.4	213.3	1.1	197.7	198.7	-1.0	214.9	212.4	2.4	226.0	225.8	0.3	2.4
Overripe	229.0	224.4	4.6	214.5	218.5	-4.0	230.8	224.5	6.3	247.0	236.0	11	8.6
Dispersal	241.7	239.7	2.0	220.0	235.5	-16	240.5	234.5	6.0	258.7	253.0	5.7	13
1st flower to fully ripe	80.7	78.8	1.9	72.7	70.7	2.0	81.4	79.0	2.4	82.4	81.2	1.2	

5.4.2 Growth Chamber Observations

There was a marked difference in the timing of fully ripe fruit between the baseline and A2 growth chamber scenarios (Figure 5.7). A variance of 32 days separated the timing of fully ripe fruit, and a lesser separation of the preceding phenophases. This gradual increase in

disparity is a result of the temperature profiles being more closely related earlier in the season as the plants transitioned from cold stratification. The earlier onset of phenophases in the warming scenario was proportionately explained by the average chamber temperatures preceding each phenophase. This ratio was calculated to show the average rate of seasonal advance being 7.0 days per every 1°C increase.

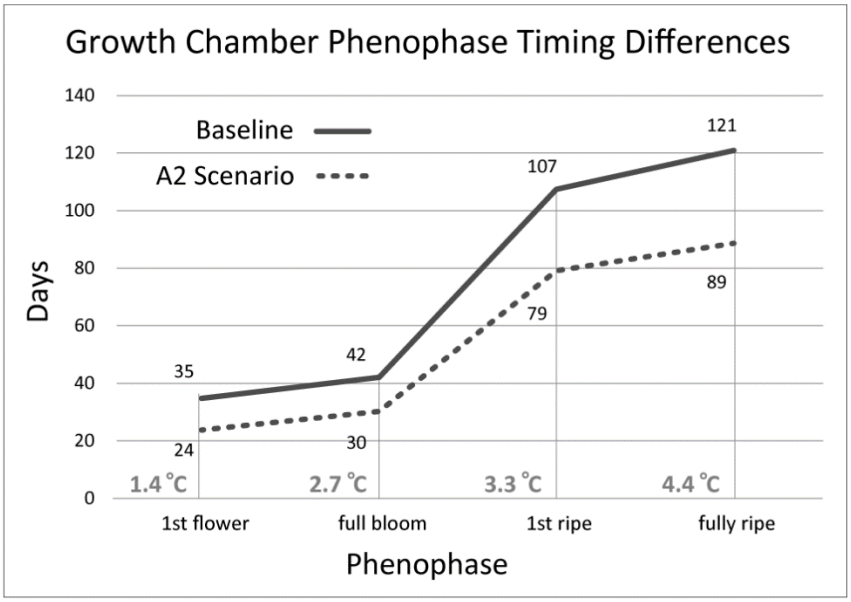

Figure 5.7 Differences in combined observations of developmental phenophase timing between the baseline and A2 warming scenarios for *Shepherdia canadensis*. Temperature values indicate the difference in mean chamber temperatures preceding each phenophase.

5.4.3 Future Climate Scenarios

There is a clear advance in phenophase timing in the study area under both warming scenarios, with the magnitude of phenological shifts corresponding to the temperature increase in each (Figure 5.8). The B1 scenario provides the likely minimal extent of future change across the study area, while the more aggressive A2 the likely upper extent. A

comparison between the baseline and future phenology maps shows a considerable difference in the prevalent phenology at the same time of year. A summary of these changes in timing and distribution are shown in Table 5.3. Temporal shifts were based on the time when maximum spatial coverage of a particular phenophase was reached. For fruit ripening, this was particularly important as it reflects the peak abundance of nutrition available for bears. The timing of fully ripe fruit was advanced by 14 days in the B1 scenario and by 17 days in the A2 (Figure 5.9). This shift in the A2 scenario of 6.6 days per °C is nearly analogous to that observed in the growth chambers of 7 days per °C (derived from the same four phenophases as those observed in the growth chambers). This temporal shift increases with elevation through the montane into the subalpine with a 30 day advance in the timing of peak ripe fruit.

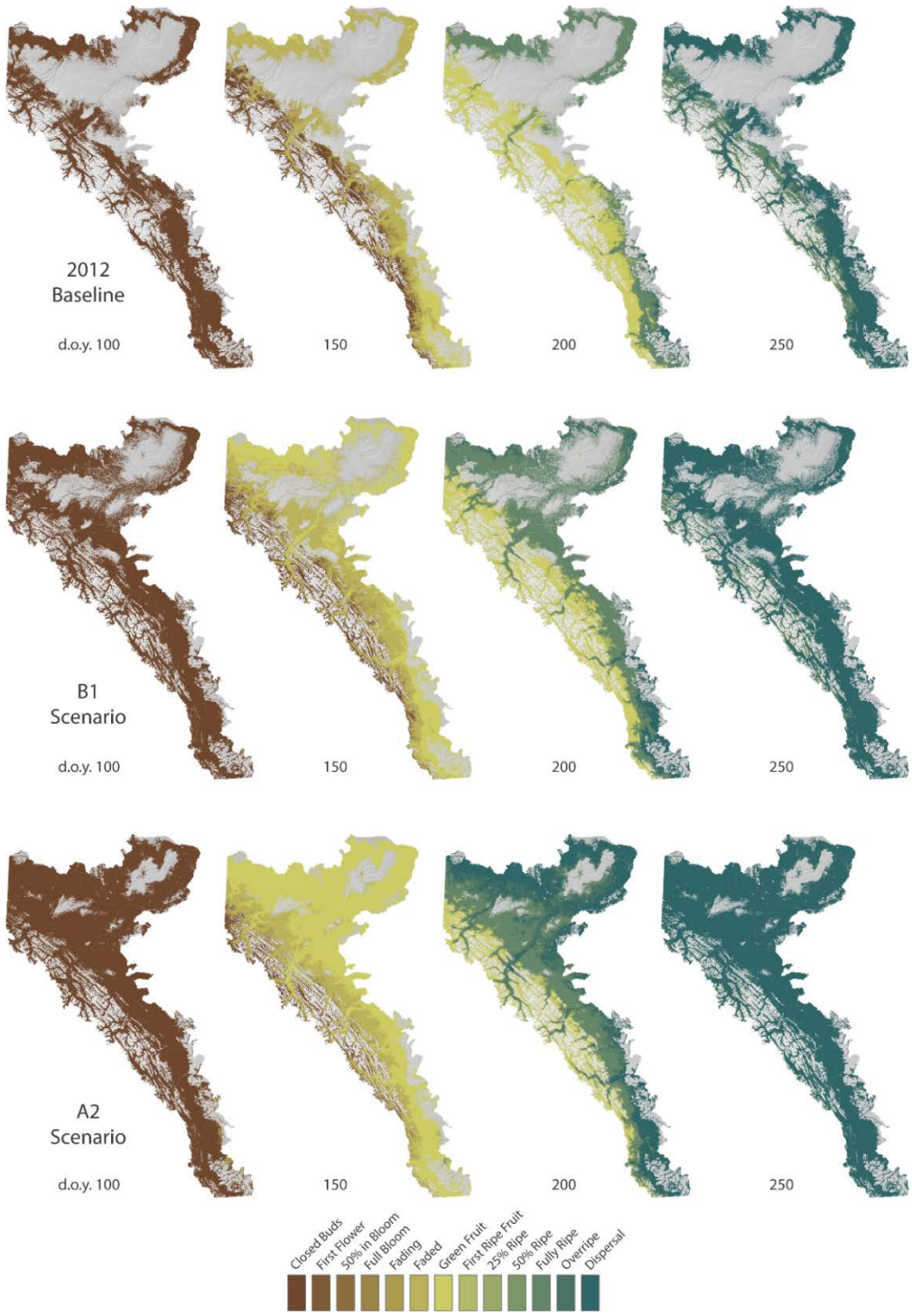

Figure 5.8 Shifts in phenophase timing and habitat distribution of *Shepherdia canadensis* under future warming scenarios B1 (moderate) and A2 (aggressive) relative to the 2012 baseline. Arbitrary intervals to portray seasonal development (day of year). Habitat niche-extent based on models derived by Roberts et al. (2014) for present day and end-of-century forecasts.

Table 5.3 The summary of present day and future spatial and temporal changes in critical *Shepherdia canadensis* phenophases within the study area. The appearance of first flower acts as a proxy for start of season, first ripe represents the beginning of a critical foraging period for grizzly bears, and fully ripe marks the peak of available nutrition. Phenophase start times and the time of peak coverage are day of year, elevation in meters above sea level, extent of peak spatial coverage in square kilometers. Table rows display the baseline scenario values followed by the amount of shift experienced under the B1 (moderate) and A2 (aggressive) warming scenarios.

Phenophase	Scenario	Start Time (d.o.y)	Time of Peak Coverage (d.o.y)	Average Elevation at Peak Coverage (m)	Area at Peak Coverage (km^2)	Change in Coverage (%)
Study Area						
1st Flower	Baseline	102	150	1690	3901	-
	B1	-7	-26	-709	+9173	+235
	A2	-13	-31	-679	+13149	+337
1st Ripe	Baseline	163	191	842	5168	-
	B1	-10	-5	+181	+2461	+48
	A2	-19	-14	+151	+5747	+111
Fully Ripe	Baseline	171	208	993	22537	-
	B1	-11	-10	+24	+12656	+56
	A2	-20	-17	+37	+24046	+107
Foothills						
1st Flower	Baseline	102	150	866	7631	-
	B1	-7	-6	+64	+4033	+53
	A2	-13	-11	+105	+7985	+105
1st Ripe	Baseline	163	191	770	4564	-
	B1	-10	-5	+201	+2013	+44
	A2	-19	-14	+186	+5345	+117
Fully Ripe	Baseline	171	207	885	18030	-
	B1	-11	-9	69	11999	+67
	A2	-20	-17	+70	23176	+129
Montane						
1st Flower	Baseline	112	129	1357	1283	-
	B1	-7	-7	-2	+26	+2
	A2	-13	-15	+12	+155	+12
1st Ripe	Baseline	175	196	1343	1060	-
	B1	-10	-10	-3	-44	-4
	A2	-19	-20	1	-69	-7
Fully Ripe	Baseline	183	214	1383	5115	-
	B1	-11	-12	+3	+13	+0.1
	A2	-20	-22	0	-58	-1
Subalpine						
1st Flower	Baseline	122	151	1729	3577	-
	B1	-6	-9	+22	-116	-3
	A2	-10	-17	-29	+523	+15
1st Ripe	Baseline	192	220	1682	2571	-
	B1	-10	-13	+22	-41	-2
	A2	-19	-24	-16	+275	+11
Fully Ripe	Baseline	199	243	1737	12340	-
	B1	-10	-16	+46	+692	+6
	A2	-19	-30	-3	+2148	+17

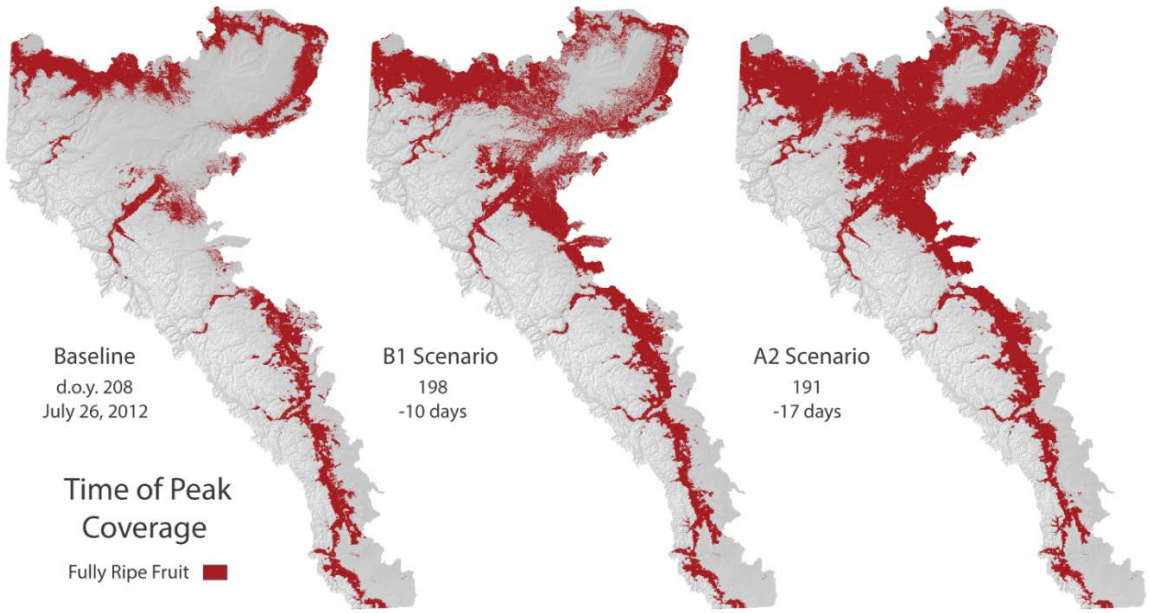

Figure 5.9 The timing of maximum spatial coverage of fully ripe *Shepherdia canadensis* under the baseline, B1 (moderate), and A2 (aggressive) warming scenarios. Dates of peak coverage in the warming scenarios clearly advance compared to the baseline by 10 (+1.8°C) and 17 (+3.4°C) days respectively.

The appearance of the first flower is the earliest observable phenophase in *S. canadensis*, preceding leaf-out by approximately two weeks. The shift in flowering dates was not as dramatic as berry ripening; beginning a week earlier in the B1 scenario and 13 days earlier in the A2 (Table 5.3). This shift is consistent through the study area, with a smaller disparity in the subalpine of 10 days earlier in the A2. First ripe fruit marks the beginning of the critical berry foraging period for bears, and precedes full ripening by one week on average. This duration from first ripe to fully ripe remains consistent across both warming scenarios, producing no observable change in the rate of maturation. In addition to the advance in timing, future warming substantially increases *S. canadensis* habitat extent. As a result, there is a 56% increase in peak coverage by ripe fruit in the B1 scenario and over double the baseline in the A2 scenario (Figure 5.10). This is largely attributed to

niche expansion into the foothills, where the montane and subalpine show proportionately little change in habitat extent. Despite large increases in the coverage of ripe fruit across the study area, there is little change in average elevation during peak coverage. There is a general trend of movement into higher elevations, but rarely exceeding 100 m in any subregion. The only substantial change was an average drop in elevation of approximately 700 m across the study area at the peak of first flower.

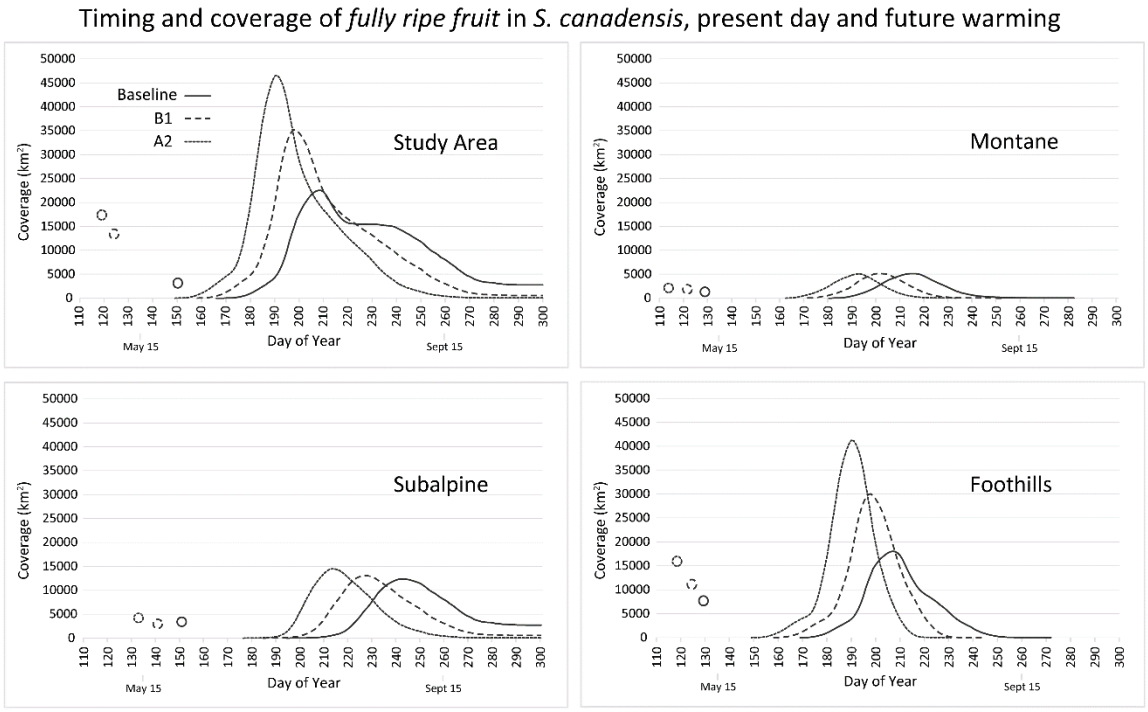

Figure 5.10 Curves illustrate the area of the landscape (km^2) covered by fully ripe *Shepherdia canadensis* across the growing season for the baseline, B1, and A2 scenarios. The circles indicate the timing of peak coverage for the appearance of first flowers as a gauge of developmental start dates. There is a clear seasonal advance in timing that increases proportionately with the amount of projected warming.

5.5 Discussion

5.5.1 Baseline Phenology Maps

This study developed a framework to accurately map present day understory phenology and then project the impacts of future warming scenarios. The framework expands on existing phenology mapping approaches by using thermal satellite imagery to discern individual phenophases of specific understory plant species. It used enhanced resolution T_{ust} maps to discern fine microclimatic characteristics that could not typically be derived from interpolated weather station data (Neteler *et al*., 2011). The first ten developmental phenophases of *S. canadensis* were estimated across the study area to within 1.39 days, on average, and the final two senescing phenophases at 3.3 days. At the image-pixel scale, the developmental phenophases of individual plants were estimated with an MAE of 4.1 days and the senescing phenophases at 10.8 days. The phenophase most critical in terms of nutrition for grizzly bears had the lowest MAE of 2.4 days, fully ripe fruit. Direct comparisons of these results with other studies is challenging since they have different objectives framed within different spatial and temporal scales. The accuracy of this thermal approach is similar to Yu *et al*. (2016), who used in situ temperature measurements to predict 24 discrete stages of developmental phenology of a deciduous tree species with a MAE of 3.6 days. However these were site-specific predictions made using AGDD calculated from in situ temperature measurements, not from satellite imagery. Most land surface phenology predictions from satellite infer the timing of ground events from a seasonal curve based on a spectral index (e.g. Beck *et al*., 2007; Soudani *et al*., 2008; Kross *et al*., 2011; White *et al*., 2014). These curves works well for dealing with cloud-punctuated datasets and for detecting dramatic spectral shifts during green up and senescence. They

are however less sensitive to discrete changes in mid-season phenology, especially beneath the forest canopy. The approach presented in this chapter provides excellent discrimination of individual phenophases using AGDD. The volume of in situ camera imagery makes manual interpretation an arduous task, however recent developments in the use of citizen science to interpret imagery shows potential to offset this effort (e.g. Delbart *et al.*, 2015; Kosmala *et al.*, 2016). The thermal approach was limited in estimating late season phenophases, but many of the physiological controls of senescence remain ambiguous making them difficult to predict in general (Keenan and Richardson 2015; Nijland *et al.*, 2016).

Overripe fruit and dispersal were challenging to predict for the reason that they are largely uncontrolled by temperature. Temperature will affect the rate at which berries desiccate, however dispersal is more mechanical than physiological. Fruit abscission can occur from predation by bears and other animals or simply by a gust of wind. It was observed in the growth chambers that berries will fall from the plant unprovoked by an external factor. Only this discernibly 'natural' dispersal was used for calculating AGDD, and obvious predation detected in the imagery was avoided. Predictions of late season phenology could be improved by incorporating chilling degree-days (ACDD) (Schwartz and Reiter 2000; Ruiz *et al.*, 2007). ACDD are essentially the inverse of AGDD, where accumulations begin in mid-summer when the temperature drops below an established threshold temperature (i.e. 20°C). Yu *et al.* (2016) found late-season ACDD an important predictor of leaf coloration and senescence.

Map accuracy was subject to a few factors, the main influence being cloud cover. Portions of the study area could be obscured by persistent cloud cover for periods lasting

over two weeks. The slight underestimation of start times in the foothills was likely due to prevalent cloud cover in the mountains and more clear, warmer days in the foothills. The cloud gap-filling algorithm used in preprocessing (Chapter 4; Laskin *et al*., 2016b) produces slightly cooler pixels in an attempt to reduce a warming bias found in other interpolation algorithms (e.g. Metz *et al*., 2014). This difference between timing in subregions could also be a result of using standard AGDD start date values on plants that have variable genetics. Some plants may be better conditioned to handle colder weather (Primack *et al*., 2015; Liang et al., 2016), in the subalpine versus the lower foothills for example. Even within a single pixel, two plants may not have identical development rates due to phenotypic expression, age, or other factors like shade or sun flecks. One of the major assumptions of this framework is that temperature controls the rate of phenological development in plants. This is largely true in regions with marked seasonal climates (White *et al*., 1999), but the map predictions omitted many mechanistic refinements such as soil quality, available nutrients, humidity – all things known to have an impact on phenology (Wielgolaski 1999; Spano *et al*., 1999; Rötzer *et al*., 2004). The map accuracy was still very good despite these omissions, and a benefit of the framework is the relative simplicity of using temperature as the main covariate. That being said however, there is opportunity to refine the methodology.

Liang *et al*. (2012) found that understory plant phenology was strongly affected by day-to-day changes in humidity. Therefore a repeated measure ANOVA was performed to investigate whether there was any regional effect on in situ plot humidity and found a statistically significant difference across the study area (2011: $F = 52.1$, $p < 0.01$; 2012: $F = 340.8$, $p < 0.01$). However the practical variance in humidity was only 3% in 2011 and

10% in 2012, this slight variability could still potentially have affected plant development. The original T_{ust} models may have accounted for some of this variance in humidity through the covariates of species composition (forest type) and crown closure indirectly acting as proxies of humidity. In the future, site moisture could be added to the framework by deriving it from the MODIS thermal bands (Zhang *et al*., 2014). This is an especially important factor to consider since most warming models predict an increase in future precipitation (Mendelsohn *et al*., 2016).

5.5.2 Extensibility of the Framework

The advantage of this remote sensing mapping framework is that it is applicable to any plant species that has defined phenology that corresponds to temperature. These species would prospectively reside in regions with distinct seasonality such as the northern temperate, boreal, and Arctic. These high-latitude climates are currently experiencing rates of warming two to three times the global average (Kug *et al*., 2015). We tested the extensibility of the framework by performing a tributary analysis on *H. alpinum*, an important plant for grizzly bears which has a radically different developmental physiology than *S. canadensis*. Nutrition in *H. alpinum* is provided by a perennial taproot that is dug by bears in early spring (Figure 5.1) (McLellan and Hovey 1995; Munro *et al*., 2006). Unlike the ripening of berries, the timing of peak nutrition from *H. alpinum* cannot be directly observed and must be inferred from the above-ground vegetative phenology. Peak crude protein was determined to occur at the earliest stage of leaf development before root energy is depleted from growth and before the bears move on to species that require less effort to forage (Hamer and Herrero 1987; Coogan *et al*., 2012).

There was no significant difference in the timing of *H. alpinum* map phenology and in situ observations on the ground (t = -0.058; p = 0.954; Correlation = 0.964). The results were not as accurate as with *S. canadensis* and there was a similar trend in reduced accuracy predicting leaf coloration and senescence, especially in the subalpine (Table 5.4). Peak crude protein (approximated by *1st leaf unfolding*) was predicted on average across the study area to less than a day, but the pixel-scale variability was six days. The decreased map accuracy most likely results from difficulty in establishing boundaries for the gradual phenophase transitions. The transitions of this plant are very prolonged and can often exist in multiple phenophases simultaneously making objective observations difficult (Chapter 2; Laskin and McDermid 2016). This species also may not respond to temperature in the same manner as *S. canadensis*, making estimates using AGDD less effective. These results suggest that certain plants are more suitable than others for observing physical changes in phenology using this framework, and should be taken into consideration when selecting study species. Despite the increased variability in map accuracy, the framework still effectively represented present day phenology patterns (Figure 5.11) and trends under warming in *H. alpinum* (Figure 5.12).

Table 5.4 *Hedysarum alpinum* map start dates (day of year) validated against in situ ground observations. Average start dates by phenophase and the difference between them (in days) are shown for the entire study area, individual subregions, and the mean absolute error (MAE) in days at the pixel-scale. Negative values indicate an underestimation by the map. 1st Leaf Unfolded is highlighted to indicate the timing of peak nutrition. *Snowfall in subalpine.

	Study Area			Foothills			Montane			Subalpine			
	Map	**Ground**	**Difference**	**Map**	**Ground**	**Difference**	**Map**	**Ground**	**Difference**	**Map**	**Ground**	**Difference**	**Pixel MAE**
Shoot Visible	144.2	146.7	**-2.5**	140.2	145.0	**-4.8**	143.8	145.8	**-2.0**	149.8	150.0	**-0.3**	**9.2**
★ 1st Leaf Unfolded	162.6	163.5	**-0.8**	158.6	157.4	**1.2**	163.2	167.6	**-4.4**	170.8	169.8	**1.0**	**6.1**
3 Leaves Unfolded	170.4	171.2	**-0.8**	165.0	164.4	**0.6**	169.8	173.0	**-3.2**	178.0	177.5	**0.5**	**6.2**
Fully Unfolded	184.9	187.0	**-2.1**	180.8	184.6	**-3.8**	180.6	185.8	**-5.2**	195.3	191.5	**3.8**	**7.4**
1st Yellow Leaf	243.6	238.5	**5.1**	237.0	235.2	**1.8**	238.8	243.2	**-4.4**	257.8	236.8	**21**	**15**
50% Yellow	254.6	253.8	**0.8**	246.8	251.3	**-4.5**	256.0	257.0	**-1.0**	267.5	252.5	**15**	**10**
Completely Yellow	260.0	262.1	**-2.1**	259.3	259.5	**-0.3**	257.3	268.7	**-11**	271.0	253.0	**18**	**12**
Abscission	262.3	270.1	**-7.9**	261.8	268.3	**-6.5**	262.8	272.0	**-9.3**	*	*	*	**13**

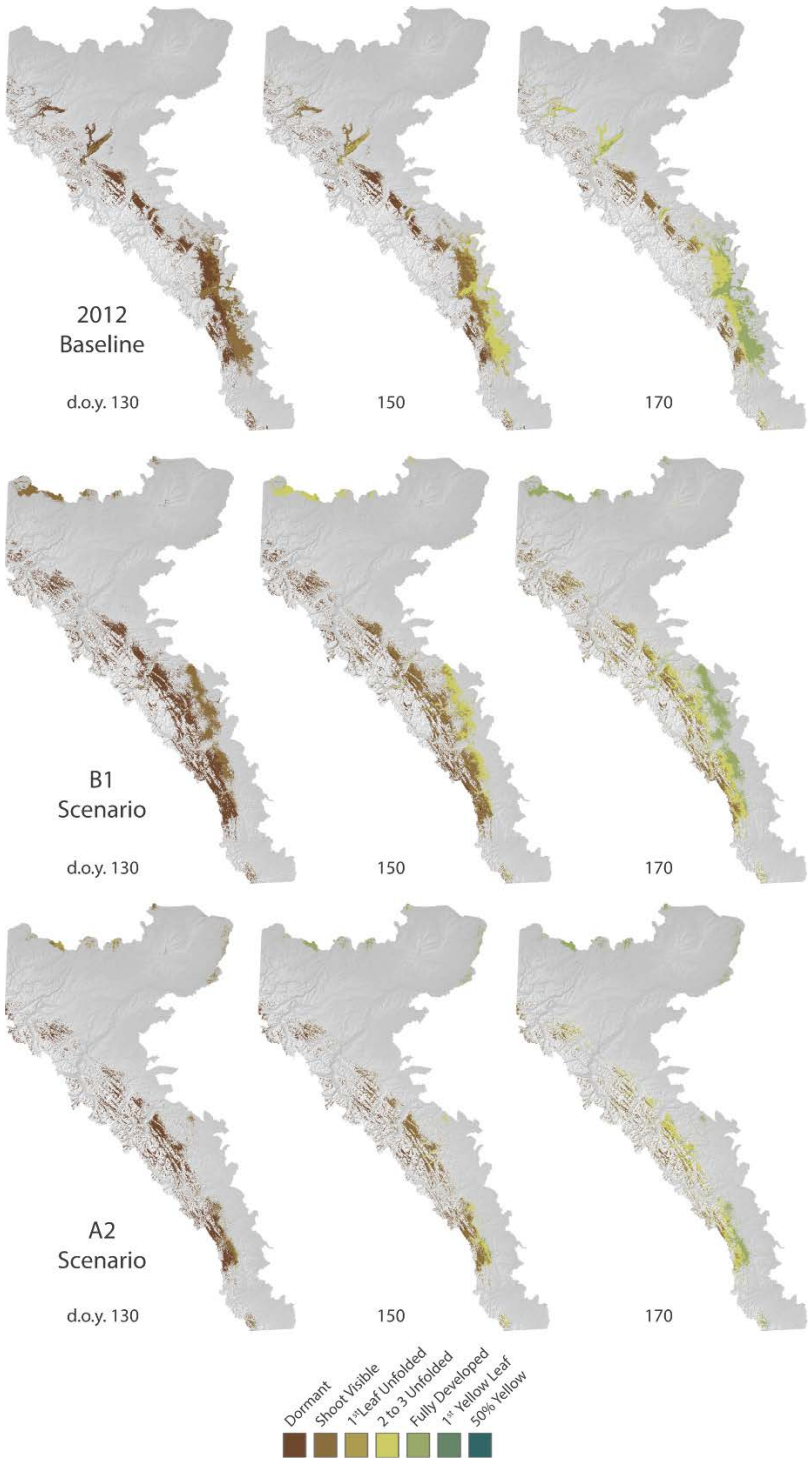

Figure 5.11 Shifts in phenophase timing and habitat distribution of *Hedysarum alpinum* under future warming scenarios B1 (moderate) and A2 (aggressive) relative to the 2012 baseline. Arbitrary intervals to portray early to mid-season development highlighting the period of peak crude protein (day of year). Habitat niche-extent based on models derived by Roberts et al. (2014) for present day and end-of-century forecasts.

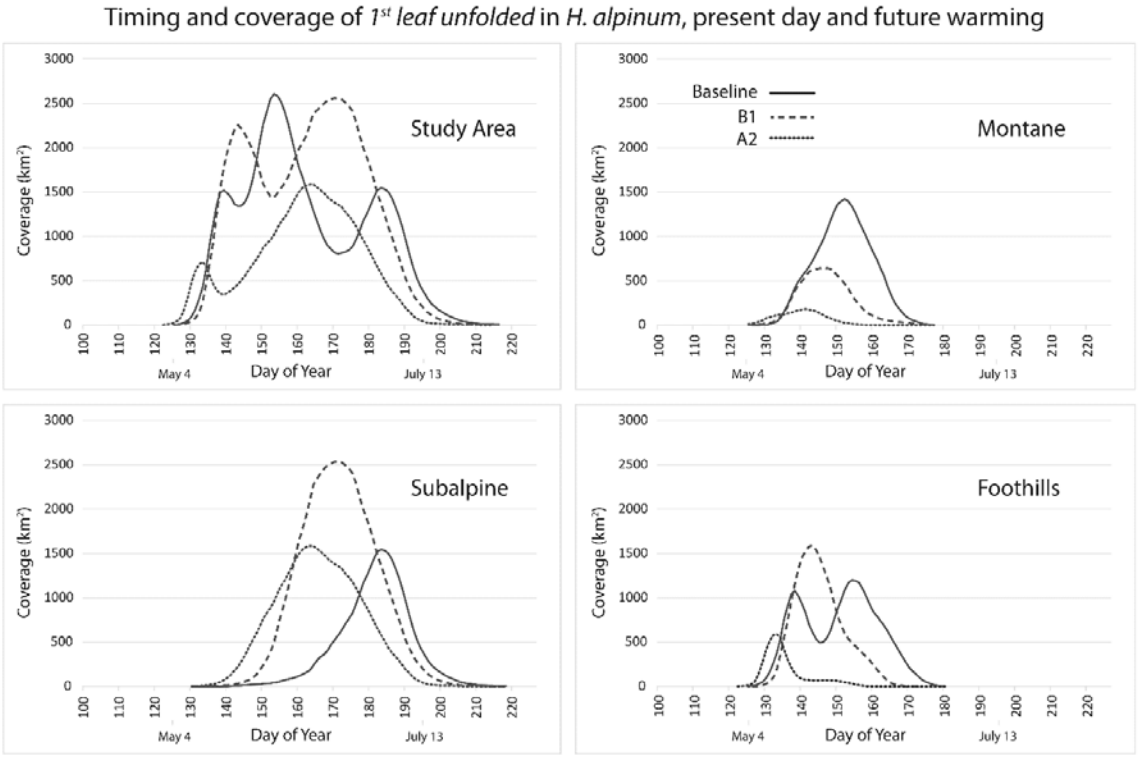

Figure 5.12 Curves illustrate the area of the landscape (km^2) covered by peak crude protein in *Hedysarum alpinum* across the growing season for the baseline, B1, and A2 scenarios. Overall, there is a delayed occurrence in peak coverage in the future scenarios compared to the baseline year as a result of upslope habitat migration to cooler regions.

Across the study area *H. alpinum* is projected to gain 45% in total habitat area in the B1 and lose 15% in A2 (Roberts *et al*., 2014). Both scenarios roughly gain equal amounts of habitat at higher elevations, but some habitat is lost in the A2 along the eastern slopes of the mountains. The multimodal distribution summarized in the timing of peak nutrition is a result of the irregular distribution of habitat in all scenarios (Figure 5.12). Although more projected habitat is available in the B1 scenario, the peak of maximum coverage occurs later in the season since this new habitat is in higher, cooler elevations. The appearance of the first unfolded leaf only advances by two or three days across the study area, with a maximum shift in the subalpine of 10 days earlier in the A2. The B1

scenario produces more coverage in the foothills, but the duration of availability is not as sustained as the baseline which provides more consistent forage for longer. Warming in the A2 scenario provides very insignificant amounts of habitat-gain or availability in the foothills. The montane subregion shows a temporal advance but a reduction in peak coverage with warming. In the subalpine, the phenology is also advanced under warming with the B1 providing significantly more coverage here than the A2. Although there are substantial shifts in phenology for *H. alpinum* in the future, a more pressing concern is the overall reduction in habitat in the A2 scenario.

5.5.3 Growth Chamber Observations

The growth chamber experiments exhibited a clear phenophase advance in response to warming, corresponding with advance the future climate phenology maps. The timing of fully ripe fruit was shifted earlier at a rate of 7.0 days per °C. This response was very similar to the artificial warming of deerberry (*V. stamineum*) by Marchin *et al*. (2015) which flowered 6.3 days earlier per °C. Liu *et al*., (2011) observed florescence rates in subalpine anemones to advance by a week per 1.5°C in open-top chambers. Kopp and Cleland (2015) examined the effects of warming on *Trifolium andersonii*, an alpine clover, and observed an advance in peak flowering of 7.1 days per °C at 3000 m elevation. Price and Waser (1998) found that in a subalpine meadow fruit set was greater in artificially warmed plots for a variety of angiosperms, and concluded that global warming will cause immediate phenological shifts in plant communities at high elevations. A very large-scale study by Wolkovich *et al*. (2012) compared long term observations with experimental warming in 1558 wild plant species. They determined that spring leafing and flowering

will continue to advance at a rate of 5 to 6 days per °C in many regions of the world. They emphasized that experimental warming greatly underpredicts plants phenological response to climate variability, suggesting that *S. canadensis* may be more sensitive to warming than what was observed in the chambers. However they also note that this underprediction may be a result of lower irradiance and drier soils in the growth chambers, which could also be the case in our experiments. Overall, the growth chambers provided control environments to observe physiological changes without the confounding variables found in the study area. The evident developmental parallels between growth chamber and field observations, lead us to assume that the response of *S. canadensis* to warming will be similar across the study area in the future.

5.5.4 Climate Projections and Effects on Grizzly Bears

Climate change is already altering the timing of vegetation phenology and the animals that rely on it (Root *et al*., 2003). The future scenarios produced significant shifts in both the phenology and distribution of *S. canadensis* and *H. alpinum*. Despite their relative magnitudes, it is unlikely these projected changes will result in the collapse of trophic linkages on which grizzly bears depend (Roberts *et al*., 2014). However, they present some concern regarding trophic synchrony and will undoubtedly modify how bears use the landscape. The general delay of leaf-out in *H. alpinum* could extend the critical period between bear den emergence and peak availability of crude protein. The earlier occurrence of flowering in *S. canadensis* by nearly two weeks will increase the risk of spring frost damage especially at higher elevations (Bennie *et al*., 2009). Early season frost can impact floral abundance which in turn will reduce the availability of berries later that year for bears

(Inouye 2008). Hegland *et al*. (2009) observed the onset of flowering and the appearance of pollinators to advance linearly in response to recent warming. However the projected 31 day shift in peak flowering may be substantial enough to produce a mismatch and impact fruit onset. The peak of ripe fruit occurring earlier in the season will produce a larger gap between the availability of this critical nutrition source and the time of hibernation, potentially leading to food deprivation if winter is delayed (Pigeon *et al*., 2016). The forward shift of seasonal phenology can also create compounding effects on the following season's phenology as plants are forced to enter dormancy earlier (Fu *et al*., 2014). If projected warming portends milder winters, a lack of chilling days during dormancy can affect the timing of budburst the following spring (Pletsers *et al*., 2015).

Compared to the foothills subregion, the relatively small expansion of *S. canadensis* habitat in the subalpine and montane is a result of steep topography limiting the rate of expansion (Walther *et al*., 2002). This offers some additional upslope foraging for bears as an alternative to using valley bottoms, which have an increased risk of stress and human conflict (Nielsen *et al*., 2016). In the montane there is little to no change in timing, which is possibly a result of temperature changes being equalized the subregion's variable microclimates. Even small phenological changes in the montane could produce impacts on grizzly bear movement through the spatially restricted habitat corridors (Duke *et al*., 2001; Chetkiewicz *et al*., 2006; Proctor *et al*., 2015).

The largest projected change in the study area is the broad expansion of *S. canadensis* habitat in to the foothills. The distribution models of Roberts *et al*. (2014) assume a perfect dispersal scenario where species are expected to reach all suitable habitats by the end of the century. Where expansion in the mountains is limited by topography, the

more uniform foothills permit rapid dispersal into novel niche extents opened by the slightest warming. In reality this expansion may not be realized due to a human fragmented landscape and the slow dispersal rates of shrubs. However bears themselves are highly mobile foragers that may be capable of dispersing seeds to the extent of the future potential niche (Naoe 2016). Even though there is projected to be more overall peak availability of fruit, it is short-lived compared to the present day scenario which provides more sustained availability over a longer period (figure 5.10). It has been shown that this prolonged duration of phenological heterogeneity across the landscape is more important than the overall abundance of food (Armstrong et al., 2016). The increase in habitat shows that warming is beneficial to *S. canadensis*, however these projections exclude complexities such as competition with other species. With the introduction of newly available niche extents in novel future climates, species competition will be likely (Walker *et al.*, 2006). Kopp and Cleland (2015) found that the phenological response to warming is affected by shading from competing species that can potentially delay phenophases despite it being warmer. In the context of *S. canadensis*, a rapid dispersal into the foothills would be accompanied by overstory shade-producing species such as *P. tremuloides* and *P. glauca*. Shade was also found to suppress flower production which could affect fruit abundance later in the season.

From a wildlife management perspective, these projected changes are likely to draw foraging bears into new areas at different times of year (Nielsen *et al*., 2010). This framework can assist mangers predict when and where these interactions are likely to occur at present and in the future. Macronutrient preferences of grizzly bears are a strong driver of their conflict with humans due to their nutrient-specific foraging behavior (Coogan and

Raubenheimer 2016). The availability of highly localized berry abundance on the landscape will attract bears to those locations (Wilson *et al*., 2005). If these locations are adjacent to human settlements the likelihood of conflict and bear mortality will be increased. These *ecological traps* can be detrimental to an already threatened population of grizzly bears (Doak 1995). Concentrated *S. canadensis* and black huckleberry (*Vaccinium membranaceum*) distributions have created a localized trap adjacent to the study area where the population of grizzly bears has declined to 163 from 271 over an eight-year period (Lamb *et al*., 2016). Using the maps to forecast seasonal onset of ripe fruit could effectively reduce bear mortality by anticipating their arrival; e.g. by proactive trail and campsite closures (Coltrane and Sinnott 2015), or preemptive reductions of vehicular traffic in sinks (Northrup *et al*., 2012). It is assumed that grizzly bear occurrence in the study area is largely driven by the appearance of fruit, however the controls of habitat-use are a considerably more complex combination of bottom-up and top down processes (Nielsen *et al*., 2016).

Within the framework, the projected average temperatures of the warming scenarios were broadly applied to the baseline T_{ust} maps. Although this provided an effective general forecast of future phenological timing, it is highly probable that increases in temperature would not be uniform across the study area. The climate projections would benefit from using spatially enhanced models derived specifically for the region to incorporate the temperature patterns and anomalies unique to this area. In future applications, regional scenarios could be obtained from the CMIP5 models used to calculate the broader IPCC climate simulations (e.g. Su *et al*., 2013). Or alternately apply warming projections derived through the North American Regional Climate Change

Assessment Program (NARCCAP) which produces gridded simulations at 30 km spatial resolution.

5.6 Conclusions

This innovative framework is capable of mapping the daily discrete phenology of understory vegetation in medium spatial resolution over a broad mountainous region typified by frequent cloud cover. The maps predicted average start dates and peak distribution across the study area to within a day for most phenophases. Early developmental phenophases were clearly discerned until after fruit production, when senescence and dispersal introduced more variability. Thus this mapping approach is ideal for observations of flower and fruit development in any species with clearly discernable phenophases. The timing of these particular events are ecologically critical in regard to observing trends in spring onset or the availability of high quality forage for wildlife. The framework also provides a novel look into the combined effects of projected climate change on the timing and distribution of vegetative nutrition used by grizzly bears. Future warming projected up to a 17-day advance in the peak distribution fully ripe berries across the study area, and up to one month earlier in the subalpine. These projected shifts in fruiting phenology corresponded closely to experimental growth chamber observations that exhibited a 7-day advance per °C. These changes will likely produce more availability of berries in the study area, but with a more punctuated duration than what presently exists. There is also an increased risk of early season frost damage during flowering potentially impacting fruit production later on. It is unlikely that these shifts will result in a catastrophic ecosystem cascade, but it may intensify foraging stress on some populations as they

transition their range or encounter abbreviated nutritional windows. A projected abundance of fruit availability in human-populated regions raises concerns of an increased potential for conflict. With large expected shifts in both the distribution and timing of fruit availability, we can anticipate grizzly bears will be found in distinctly new locations at conspicuously different times.

Chuine (2010) describes phenology as one of, if not the most important factors shaping species distribution in temperate and boreal climates. Phenology maps will be the underpinning of dynamic species occurrence and movement models as we move away from static, niche-based models (Nielsen *et al*., 2010). Increasingly efficient access to MODIS LST imagery makes investigations into ecosystem phenology patterns and dynamics a timely benefit during a period of rapid environmental change. This remote sensing approach can functionally examine trends in phenology in response to interannual seasonal differences, as well as intra-season phenological progress to anticipate the arrival of berry crops. The framework provides near-real-time extensibility to determine the precise spatial extent of any phenophases occurring at a given moment. MODIS LST data are usually made available for download a few days after image acquisition (Wan 2014). Combining this mapping methodology with the processing efficiency and extensive image archive within Google Earth Engine (Google Inc. 2016) will at once expand the global extensibility of this framework.

The immediate next steps in this research are applications in grizzly bear feeding ecology within the study area. Understanding food availability is essential for successful management and conservation, since berry abundance can influence body mass, reproductive success, and movement throughout their habitat (Stenset *et al*., 2016). The

objective will be to use coincident GPS telemetry data from bears to detect spatio-temporal synchrony in response to changes in fruiting phenology. A strong movement response has been observed with salmon spawning phenology on the west coast (Armstrong *et al*., 2016). If such signal correlations exist, it will then be possible to forecast bear movements and climate velocities under future warming (Loarie *et al*., 2009). There is much potential to employ the framework in examining additional plant species as well as other ecological phenomena controlled by temperature such as, insect phenology (e.g. Pureswaran *et al*., 2015), wildfire modeling (e.g. Bajocco *et al*., 2010), and landscape pathology (e.g. Gallana *et al*., 2013). This phenology mapping methodology should be employed by others to explore global change, especially in forest ecosystems which encompass relatively underobserved microclimates that are not exempt from the impacts of climate change (De Frenne and Verheyen 2016).

5.7 References

Armstrong, J. B., Takimoto, G., Schindler, D. E., Hayes, M. M., & Kauffman, M. J. (2016). Resource waves: phenological diversity enhances foraging opportunities for mobile consumers. *Ecology*, *97*(5), 1099-1112.

Badeck, F.-W., Bondeau, A., Bottcher, K., Doktor, D., Lucht, W., Schaber, J., & Sitch, S. (2004). Responses of spring phenology to climate change. *New Phytologist, 162*(2), 295-309.

Barry, S., & Elith, J. (2006). Error and uncertainty in habitat models. *Journal of Applied Ecology*, *43*(3), 413-423.

Bater, C. W., Coops, N. C., Wulder, M. A., Hilker, T., Nielsen, S. E., McDermid, G., & Stenhouse, G. B. (2011). Using digital time-lapse cameras to monitor species-specific understorey and overstorey phenology in support of wildlife habitat assessment. *Environmental Monitoring and Assessment, 180*(1-4), 1-13.

Beck, P. S. A., Jönsson, P., Høgda, K. A., Karlsen, S. R., Eklundh, L., & Skidmore, A. K. (2007). A ground-validated NDVI dataset for monitoring vegetation dynamics and mapping phenology in Fennoscandia and the Kola Peninsula. *International Journal of Remote Sensing, 28*(19), 4311-4330.

Benz, R. A., Boyce, M. S., Thurfjell, H., Paton, D. G., Musiani, M., Dormann, C. F., & Ciuti, S. (2016). Dispersal ecology informs design of large-scale wildlife corridors. *Plos One, 11*(9).

Blois, J. L., Zarnetske, P. L., Fitzpatrick, M. C., & Finnegan, S. (2013). Climate change and the past, present, and future of biotic interactions. *Science, 341*(6145), 499-504.

Braid, A. C. R., Manzer, D., & Nielsen, S. E. (2016). Wildlife habitat enhancements for grizzly bears: Survival rates of planted fruiting shrubs in forest harvests. *Forest Ecology and Management, 369*, 144-154.

Buckley, L. B., Urban, M. C., Angilletta, M. J., Crozier, L. G., Rissler, L. J., & Sears, M. W. (2010). Can mechanism inform species' distribution models? *Ecology Letters, 13*(8), 1041-1054.

Cesaraccio, C., Spano, D., Duce, P., & Snyder, R. L. (2001). An improved model for determining degree-day values from daily temperature data. *International Journal of Biometeorology, 45*(4), 161-169.

Charney, N. D., Babst, F., Poulter, B., Record, S., Trouet, V. M., Frank, D., . . . Evans, M. E. K. (2016). Observed forest sensitivity to climate implies large changes in 21st century North American forest growth. *Ecology Letters*. *19*(9), 1119-1128.

Chetkiewicz, C.-L. B., St. Clair, C. C., & Boyce, M. S. (2006). Corridors for conservation: integrating pattern and process. *Annual Review of Ecology, Evolution, and Systematics*, 317-342.

Chmielewski, F. M., & Rotzer, T. (2002). Annual and spatial variability of the beginning of growing season in Europe in relation to air temperature changes. *Climate Research, 19*(3), 257-264.

Chuine, I. (2010). Why does phenology drive species distribution? *Philosophical Transactions of the Royal Society B-Biological Sciences, 365*(1555), 3149-3160.

Chuine, I., & Beaubien, E. G. (2001). Phenology is a major determinant of tree species range. *Ecology Letters, 4*(5), 500-510.

Clark, D. A., & Slocombe, D. S. (2011). Grizzly Bear conservation in the Foothills Model Forest: appraisal of a collaborative ecosystem management effort. *Policy Sciences, 44*(1), 1-11.

Clark, J. S., Salk, C., Melillo, J., & Mohan, J. (2014). Tree phenology responses to winter chilling, spring warming, at north and south range limits. *Functional Ecology, 28*(6), 1344-1355.

Cleland, E. E., Chuine, I., Menzel, A., Mooney, H. A., & Schwartz, M. D. (2007). Shifting plant phenology in response to global change. *Trends in Ecology & Evolution, 22*(7), 357-365.

Coltrane, J. A., & Sinnott, R. (2015). Brown bear and human recreational use of trails in Anchorage, Alaska. *Human-Wildlife Interactions, 9*(1), 132.

Coogan, S. C. P., Nielsen, S. E., & Stenhouse, G. B. (2012). Spatial and temporal heterogeneity creates a Brown Tide in Root Phenology and Nutrition. *ISRN Ecology, 2012*, 10.

Coogan, S. C. P., & Raubenheimer, D. (2016). Might macronutrient requirements influence grizzly bear-human conflict? Insights from nutritional geometry. *Ecosphere, 7*(1).

Coops, N. C., Duro, D. C., Wulder, M. A., & Han, T. (2007). Estimating afternoon MODIS land surface temperatures (LST) based on morning MODIS overpass, location and elevation information. *International Journal of Remote Sensing, 28*(10), 2391-2396.

Coops, N. C., Hilker, T., Bater, C. W., Wulder, M. A., Nielsen, S. E., McDermid, G., & Stenhouse, G. (2012). Linking ground-based to satellite-derived phenological metrics in support of habitat assessment. *Remote Sensing Letters, 3*(3), 191-200.

Crepinsek, Z., Kajfez-Bogataj, L., & Bergant, K. (2006). Modelling of weather variability effect on fitophenology. *Ecological Modelling, 194*(1-3), 256-265.

Crimmins, M. A., & Crimmins, T. M. (2008). Monitoring plant phenology using digital repeat photography. *Environmental Management, 41*(6), 949-958.

de Beurs, K. M., Henebry, G.M. (2010). Spatio-temporal statistical methods for modeling land surface phenology. . In I. L. Hudson, Keatley, M.R. (Ed.), *Phenological Research: Methods for Environmental and Climate Change Analysis.* (pp. 177-208). Dordrecht: Springer.

De Frenne, P., Rodríguez-Sánchez, F., Coomes, D. A., Baeten, L., Verstraeten, G., Vellend, M., . . Cornelis, J. (2013). Microclimate moderates plant responses to macroclimate warming. *Proceedings of the National Academy of Sciences, 110*(46), 18561-18565.

De Frenne, P., & Verheyen, K. (2016). Weather stations lack forest data. *Science, 351*(6270), 234-234.

Delbart, N., Beaubien, E., Kergoat, L., & Le Toan, T. (2015). Comparing land surface phenology with leafing and flowering observations from the PlantWatch citizen network. *Remote Sensing of Environment, 160*, 273-280.

Delbart, N., Beaubien, E., Kergoat, L., & Le Toan, T. (2016). Combining citizen science phenological observations with remote sensing data. *ESA Living Planet 2016*, May 2016, Prague, Czech Republic. 2016.

Dierschke, H. 1972. *On the recording and presentation of phenological phenomena in plant communities*. 546 1970 International Symposium for Vegetation Science [In German].

Doak, D. F. (1995). Source-sink models and the problem of habitat degradation: general models and applications to the Yellowstone grizzly. *Conservation Biology, 9*(6), 1370-1379.

Downing, D. J. & Pettapiece, W.W. (2006). Natural regions and subregions of Alberta. *Compiled by the Natural Regions Commitee. Government of Alberta. Pub*.

Duke, D. L., Hebblewhite, M., Paquet, P. C., Callaghan, C., & Percy, M. (2001). Restoring a large-carnivore corridor in Banff National Park. *Large mammal restoration. Island Press, Washington, DC*, 261-275.

Edwards, M., & Richardson, A. J. (2004). Impact of climate change on marine pelagic phenology and trophic mismatch. *Nature, 430*(7002), 881-884.

Elith, J., & Leathwick, J. R. (2009). Species distribution models: ecological explanation and prediction across space and time. *Annual Review of Ecology, Evolution, and Systematics, 40*(1), 677-697.

Festa-Bianchet, M., & Kansas, J. L. (2010). *Status of the grizzly bear (Ursus arctos) in Alberta: update 2010*: Government of Alberta.

Fu, Y. S. H., Campioli, M., Vitasse, Y., De Boeck, H. J., Van den Berge, J., Abd Elgawad, H., . . . Janssens, I. A. (2014). Variation in leaf flushing date influences autumnal senescence and next year's flushing date in two temperate tree species. *Proceedings of the National Academy of Sciences, 111*(20), 7355-7360.

Garcia, R. A., Cabeza, M., Rahbek, C., & Araújo, M. B. (2014). Multiple dimensions of climate change and their implications for biodiversity. *Science, 344*(6183), 1247579.

Gordo, O., & Sanz, J. J. (2010). Impact of climate change on plant phenology in Mediterranean ecosystems. *Global Change Biology, 16*(3), 1082-1106.

Hamer, D., & Herrero, S. (1987). Grizzly bear food and habitat in the front ranges of Banff National Park, Alberta. *Bears: their biology and management*, 199-213.

Hansen, M. C., Potapov, P. V., Moore, R., Hancher, M., Turubanova, S., Tyukavina, A., . Loveland, T. (2013). High-resolution global maps of 21st-century forest cover change. *Science, 342*(6160), 850-853.

Hassan, Q. K., Bourque, C. P. A., Meng, F. R., & Richards, W. (2007). Spatial mapping of growing degree days: an application of MODIS-based surface temperatures and enhanced vegetation index. *Journal of Applied Remote Sensing, 1*(1), 013511-013511.

Hegland, S. J., Nielsen, A., Lazaro, A., Bjerknes, A.-L., & Totland, O. (2009). How does climate warming affect plant-pollinator interactions? *Ecology Letters, 12*(2), 184-195.

Hilderbrand, G. V., Schwartz, C., Robbins, C., Jacoby, M., Hanley, T., Arthur, S., & Servheen, C. (1999). The importance of meat, particularly salmon, to body size, population productivity, and conservation of North American brown bears. *Canadian Journal of Zoology, 77*(1), 132-138.

Hoover, M.W. (1955). Some effects of temperature on the growth of southern peas. *Proceedings of the American Society of Horticultural Science,* (66):308 312.

Huang, R., Zhang, C., Huang, J. X., Zhu, D. H., Wang, L. M., & Liu, J. (2015). Mapping of daily mean air temperature in agricultural regions using daytime and nighttime land surface temperatures derived from TERRA and AQUA MODIS data. *Remote Sensing, 7*(7), 8728-8756.

Hunter, A. F., & Lechowicz, M. J. (1992). Predicting the timing of budburst in temperate trees. *Journal of Applied Ecology, 29*(3), 597-604.

IPCC. (2014). Climate Change 2014: Impacts, Adaptation, and Vulnerability. Contribution of Working Group II to the Fifth Assessment Report of the Intergovernmental Panel on Climate Change. Cambridge University Press, Cambridge, United Kingdom and New York, NY, USA.

Inouye, D. W. (2008). Effects of climate change on phenology, frost damage, and floral abundance of montane wildflowers. *Ecology, 89*(2), 353-362.

Jang, K., Kang, S., Kimball, J. S., & Hong, S. Y. (2014). Retrievals of all-weather daily air temperature using MODIS and AMSR-E data. *Remote Sensing*, *6*(9), 8387-8404.

Jarraud, M. (2008). Guide to meteorological instruments and methods of observation (wmo-no. 8). *World Meteorological Organisation: Geneva, Switzerland*.

Kearney, M. R., Wintle, B. A., & Porter, W. P. (2010). Correlative and mechanistic models of species distribution provide congruent forecasts under climate change. *Conservation Letters, 3*(3), 203-213.

Keenan, T. F., & Richardson, A. D. (2015). The timing of autumn senescence is affected by the timing of spring phenology: implications for predictive models. *Global Change Biology, 21*(7), 2634-2641.

Kerby, J. T., Wilmers, C. C., & Post, E. (2012). Climate change, phenology and the nature of consumer–resource interactions: advancing the match/mismatch hypothesis. *Trait-mediated indirect interactions: ecological and evolutionary perspectives*, 508-525.

Kloog, I., Nordio, F., Coull, B. A., & Schwartz, J. (2014). Predicting spatiotemporal mean air temperature using MODIS satellite surface temperature measurements across the Northeastern USA. *Remote Sensing of Environment, 150*, 132-139.

Knutti, R., & Sedlacek, J. (2013). Robustness and uncertainties in the new CMIP5 climate model projections. *Nature Climate Change, 3*(4), 369-373.

Kobayashi, H., Yunus, A. P., Nagai, S., Sugiura, K., Kim, Y., Van Dam, B., . . . Suzuki, R. (2016). Latitudinal gradient of spruce forest understory and tundra phenology in Alaska as observed from satellite and ground-based data. *Remote Sensing of Environment, 177*, 160-170.

Kopp, C. W., & Cleland, E. E. (2015). A range-expanding shrub species alters plant phenological response to experimental warming. *Plos One, 10*(9).

Kosmala, M., Crall, A., Cheng, R., Hufkens, K., Henderson, S., & Richardson, A. D. (2016). Season spotter: Using citizen science to validate and scale plant phenology from near-surface remote sensing. *Remote Sensing, 8*(9), 726.

Kross, A., Fernandes, R., Seaquist, J., & Beaubien, E. (2011). The effect of the temporal resolution of NDVI data on season onset dates and trends across Canadian broadleaf forests. *Remote Sensing of Environment, 115*(6), 1564-1575.

Kug, J.-S., Jeong, J.-H., Jang, Y.-S., Kim, B.-M., Folland, C. K., Min, S.-K., & Son, S.-W. (2015). Two distinct influences of Arctic warming on cold winters over North America and East Asia. *Nature Geosci, 8*(10), 759-762.

Lamb, C. T., Mowat, G., McLellan, B. N., Nielsen, S. E., & Boutin, S. (2016). Forbidden fruit: human settlement and abundant fruit create an ecological trap for an apex omnivore. *Journal of Animal Ecology*.

Lambers, J. H. R. (2015). Extinction risks from climate change. *Science, 348*(6234), 501-502.

Laskin, D. N., & McDermid, G. J. (2016). Evaluating the level of agreement between human and time-lapse camera observations of understory plant phenology at multiple scales. *Ecological Informatics, 33*, 1-9.

Laskin, D., Montaghi, A., Nielsen, S., & McDermid, G. (2016a). Estimating Understory Temperatures Using MODIS LST in Mixed Cordilleran Forests. *Remote Sensing, 8*(8), 658.

Laskin, D. N., Montaghi, A., & McDermid, G. J. (2016b). An open-source method of constructing cloud-free composites of forest understory temperature using MODIS. *Remote Sensing Letters, 8*(2), 165-174.

Lessard-Therrien, M., Davies, T. J., & Bolmgren, K. (2014). A phylogenetic comparative study of flowering phenology along an elevational gradient in the Canadian subarctic. *International Journal of Biometeorology, 58*(4), 455-462.

Liang, L., Schwartz, M. D., & Fei, S. (2012). Photographic assessment of temperate forest understory phenology in relation to springtime meteorological drivers. *International Journal of Biometeorology, 56*(2), 343-355.

Liang, L., Schwartz, M. D., & Zhang, X. (2016). Mapping temperate vegetation climate adaptation variability using normalized land surface phenology. *Climate, 4*(2), 24.

Linke, J., McDermid, G. J., Pape, A. D., McLane, A. J., Laskin, D. N., Hall-Beyer, M., & Franklin, S. E. (2009). The influence of patch-delineation mismatches on multi-temporal landscape pattern analysis. *Landscape Ecology, 24*(2), 157-170.

Liu, Y., Reich, P. B., Li, G., & Sun, S. (2011). Shifting phenology and abundance under experimental warming alters trophic relationships and plant reproductive capacity. *Ecology, 92*(6), 1201-1207.

Loarie, S. R., Duffy, P. B., Hamilton, H., Asner, G. P., Field, C. B., & Ackerly, D. D. (2009). The velocity of climate change. *Nature, 462*(7276), 1052-1055.

Macbeth, B. J., Cattet, M. R. L., Stenhouse, G. B., Gibeau, M. L., & Janz, D. M. (2010). Hair cortisol concentration as a noninvasive measure of long-term stress in free-ranging grizzly bears (*Ursus arctos*): considerations with implications for other wildlife. *Canadian Journal of Zoology-Revue Canadienne De Zoologie, 88*(10), 935-949.

Macdonald, S. E., & Chinnappa, C. C. (1989). Population differentiation for phenotypic plasticity in the stellaria-longipes complex. *American Journal of Botany, 76*(11), 1627-1637.

Marchin, R. M., Salk, C. F., Hoffmann, W. A., & Dunn, R. R. (2015). Temperature alone does not explain phenological variation of diverse temperate plants under experimental warming. *Global Change Biology, 21*(8), 3138-3151.

McLellan, B. N. (2011). Implications of a high-energy and low-protein diet on the body composition, fitness, and competitive abilities of black (*Ursus americanus*) and grizzly (*Ursus arctos*) bears. *Canadian Journal of Zoology-Revue Canadienne De Zoologie, 89*(6), 546-558.

McLellan, B. N., & Hovey, F. W. (1995). The diet of grizzly hears in the Flathead River drainage of southeastern British-Columbia. *Canadian Journal of Zoology-Revue Canadienne De Zoologie, 73*(4), 704-712.

McMaster, G. S., & Wilhelm, W. W. (1997). Growing degree-days: one equation, two interpretations. *Agricultural and Forest Meteorology, 87*(4), 291-300.

McMaster, G. S., Wilhelm, W. W., & Frank, A. B. (2005). Developmental sequences for simulating crop phenology for water-limiting conditions. *Australian Journal of Agricultural Research, 56*(11), 1277-1288.

Mendelsohn, R., Prentice, I. C., Schmitz, O., Stocker, B., Buchkowski, R., & Dawson, B. (2016). The Ecosystem Impacts of Severe Warming. *The American Economic Review, 106*(5), 612-614.

Menzel, A., Sparks, T. H., Estrella, N., Koch, E., Aasa, A., Ahas, R., . . . Zust, A. (2006). European phenological response to climate change matches the warming pattern. *Global Change Biology, 12*(10), 1969-1976.

Metz, M., Rocchini, D., & Neteler, M. (2014). Surface temperatures at the continental scale: Tracking changes with remote sensing at unprecedented detail. *Remote Sensing, 6*(5), 3822-3840.

Middleton, A. D., Kauffman, M. J., McWhirter, D. E., Cook, J. G., Cook, R. C., Nelson, A. A., . . Klaver, R. W. (2013). Animal migration amid shifting patterns of phenology and predation: lessons from a Yellowstone elk herd. *Ecology, 94*(6), 1245-1256.

Mildrexler, D. J., Zhao, M., & Running, S. W. (2011). A global comparison between station air temperatures and MODIS land surface temperatures reveals the cooling role of forests. *Journal of Geophysical Research-Biogeosciences, 116*(G3).

Miller, P., Lanier, W., & Brandt, S. (2001). Using growing degree days to predict plant stages. *Ag/Extension Communications Coordinator, Communications Services, Montana State University-Bozeman, Bozeman, MO*.

Misra, G., Buras, A., & Menzel, A. (2016). Effects of different methods on the comparison between land surface and ground phenology – a methodological case study from south-western Germany. *Remote Sensing, 8*(9), 753.

Morellato, L. P. C., Alberton, B., Alvarado, S. T., Borges, B., Buisson, E., Camargo, M. G. G., . . Leite, P. T. (2016). Linking plant phenology to conservation biology. *Biological Conservation, 195*, 60-72.

Morin, X., Augspurger, C., & Chuine, I. (2007). Process-based modeling of species' distributions: What limits temperate tree species' range boundaries? *Ecology, 88*(9), 2280-2291.

Mostovoy, G. V., King, R. L., Reddy, K. R., Kakani, V. G., & Filippova, M. G. (2006). Statistical estimation of daily maximum and minimum air temperatures from MODIS LST data over the State of Mississippi. *Giscience & Remote Sensing, 43*(1), 78-110.

Munro, R. H. M., Nielsen, S. E., Price, M. H., Stenhouse, G. B., & Boyce, M. S. (2006). Seasonal and diel patterns of grizzly bear diet and activity in west-central Alberta. *Journal of Mammalogy, 87*(6), 1112-1121.

Naoe, S., Tayasu, I., Sakai, Y., Masaki, T., Kobayashi, K., Nakajima, A., . . . Koike, S. (2016). Mountain-climbing bears protect cherry species from global warming through vertical seed dispersal. *Current Biology, 26*(8), R315-R316.

Neteler, M. (2010). Estimating daily land surface temperatures in mountainous environments by reconstructed MODIS LST data. *Remote Sensing, 2*(1), 333-351.

Neteler, M., Roiz, D., Rocchini, D., Castellani, C., & Rizzoli, A. (2011). Terra and Aqua satellites track tiger mosquito invasion: modelling the potential distribution of *Aedes albopictus* in north-eastern Italy. *International Journal of Health Geographics, 10*.

Niclos, R., Valiente, J. A., Barbera, M. J., & Caselles, V. (2014). Land surface air temperature retrieval from EOS-MODIS images. *IEEE Geoscience and Remote Sensing Letters, 11*(8), 1380-1384.

Nielsen, S. E., Boyce, M. S., Stenhouse, G. B., & Munro, R. H. M. (2003). Development and testing of phenologically driven grizzly bear habitat models. *Ecoscience, 10*(1), 1-10.

Nielsen, S. E., Larsen, T. A., Stenhouse, G. B., & Coogan, S. C. (2016). Complementary food resources of carnivory and frugivory affect local abundance of an omnivorous carnivore. *Oikos*.

Nielsen, S. E., McDermid, G., Stenhouse, G. B., & Boyce, M. S. (2010). Dynamic wildlife habitat models: Seasonal foods and mortality risk predict occupancy-abundance and habitat selection in grizzly bears. *Biological Conservation, 143*(7), 1623-1634.

Nijland, W., Bolton, D. K., Coops, N. C., & Stenhouse, G. (2016). Imaging phenology; scaling from camera plots to landscapes. *Remote Sensing of Environment, 177*, 13-20.

Norby, R. J., Hartz-Rubin, J. S., & Verbrugge, M. J. (2003). Phenological responses in maple to experimental atmospheric warming and CO_2 enrichment. *Global Change Biology, 9*(12), 1792-1801.

Northrup, J. M., Pitt, J., Muhly, T. B., Stenhouse, G. B., Musiani, M., & Boyce, M. S. (2012). Vehicle traffic shapes grizzly bear behaviour on a multiple-use landscape. *Journal of Applied Ecology, 49*(5), 1159-1167.

Parmesan, C. (2006). Ecological and evolutionary responses to recent climate change. *Annual Review of Ecology Evolution and Systematics, 37*, 637-669.

Parmesan, C., & Yohe, G. (2003). A globally coherent fingerprint of climate change impacts across natural systems. *Nature, 421*(6918), 37-42.

Pearson, A. M. (1975). The northern interior grizzly bear *Ursus arctos L*: Information Canada.

Pearson, R. G., & Dawson, T. P. (2003). Predicting the impacts of climate change on the distribution of species: are bioclimate envelope models useful? *Global Ecology and Biogeography, 12*(5), 361-371.

Pettorelli, N., Gaillard, J. M., Mysterud, A., Duncan, P., Delorme, D., Van Laere, G., . . . Klein, F. (2006). Using a proxy of plant productivity (NDVI) to find key periods for animal performance: the case of roe deer. *Oikos, 112*(3), 565-572.

Pigeon, K. E., Stenhouse, G., & Côté, S. D. (2016). Drivers of hibernation: linking food and weather to denning behaviour of grizzly bears. *Behavioral Ecology and Sociobiology, 70*(10), 1745-1754.

Pletsers, A., Caffarra, A., Kelleher, C. T., & Donnelly, A. (2015). Chilling temperature and photoperiod influence the timing of bud burst in juvenile *Betula pubescens Ehrh.* and *Populus tremulaL*. trees. *Annals of Forest Science, 72*(7), 941-953.

Post, E. S., & Inouye, D. W. (2008). Phenology: response, driver, and integrator. *Ecology, 89*(2), 319-320.

Price, M. V., & Waser, N. M. (1998). Effects of experimental warming on plant reproductive phenology in a subalpine meadow. *Ecology, 79*(4), 1261-1271.

Primack, R. B., Laube, J., Gallinat, A. S., & Menzel, A. (2015). From observations to experiments in phenology research: investigating climate change impacts on trees and shrubs using dormant twigs. *Annals of Botany, 116*(6), 889-897.

Proctor, M. F., Nielsen, S. E., Kasworm, W. F., Servheen, C., Radandt, T. G., Machutchon, A. G., & Boyce, M. S. (2015). Grizzly bear connectivity mapping in the Canada–United States trans-border region. *The Journal of Wildlife Management, 79*(4), 544-558.

R Core Team (2014). "R: A Language and Environment for Statistical Computing." *R Foundation for Statistical Computing*, Vienna, Austria. URL: R-project.org.

Reáumur, R.A. (1735). Observation du thermometre, faites a Paris pendant I'annee 1735, comparees avec celles qui ont ete faites sous la ligne, a l'Isle de France, a Alger et quelquesunes de nos isles de l'Amerique. Acad. des Sci., Padis, pp. 737-754.

Reeves, P. H., & Coupland, G. (2000). Response of plant development to environment: control of flowering by daylength and temperature. *Current opinion in plant biology, 3*(1), 37-42.

Richardson, A. D., Anderson, R. S., Arain, M. A., Barr, A. G., Bohrer, G., Chen, G. S., . . . Xue, Y. K. (2012). Terrestrial biosphere models need better representation of vegetation phenology: results from the North American Carbon Program Site Synthesis. *Global Change Biology, 18*(2), 566-584.

Roberts, D. R., Nielsen, S. E., & Stenhouse, G. B. (2014). Idiosyncratic responses of grizzly bear habitat to climate change based on projected food resource changes. *Ecological Applications, 24*(5), 1144-1154.

Roltsch, W. J., Zalom, F. G., Strawn, A. J., Strand, J. F., & Pitcairn, M. J. (1999). Evaluation of several degree-day estimation methods in California climates. *International Journal of Biometeorology, 42*(4), 169-176.

Root, T. L., Price, J. T., Hall, K. R., Schneider, S. H., Rosenzweig, C., & Pounds, J. A. (2003). Fingerprints of global warming on wild animals and plants. *Nature, 421*(6918), 57-60.

Rotzer, T., Grote, R., & Pretzsch, H. (2004). The timing of bud burst and its effect on tree growth. *International Journal of Biometeorology, 48*(3), 109-118.

Ryu, Y., Lee, G., Jeon, S., Song, Y., & Kimm, H. (2014). Monitoring multi-layer canopy spring phenology of temperate deciduous and evergreen forests using low-cost spectral sensors. *Remote Sensing of Environment, 149*(0), 227-238.

Schwartz, M. D., Ault, T. R., & Betancourt, J. L. (2012). Spring onset variations and trends in the continental United States: past and regional assessment using temperature-based indices. *International Journal of Climatology, 33*(13), 2917-2922.

Schwartz, M. D., & Reiter, B. E. (2000). Changes in North American spring. *International Journal of Climatology, 20*(8), 929-932.

Sherry, R. A., Zhou, X. H., Gu, S. L., Arnone, J. A., Schimel, D. S., Verburg, P. S., . . . Luo, Y. Q. (2007). Divergence of reproductive phenology under climate warming. *Proceedings of the National Academy of Sciences of the United States of America, 104*(1), 198-202.

Sims, D. A., Rahman, A. F., Cordova, V. D., El-Masri, B. Z., Baldocchi, D. D., Bolstad, P. V., . . . Xu, L. (2008). A new model of gross primary productivity for North American ecosystems based solely on the enhanced vegetation index and land surface temperature from MODIS. *Remote Sensing of Environment, 112*(4), 1633-1646.

Snyder, R. L. (1985). Hand calculating degree days. *Agricultural and Forest Meteorology, 35*(1-4), 353-358.

Snyder, R. L., Spano, D., Cesaraccio, C., & Duce, P. (1999). Determining degree-day thresholds from field observations. *International Journal of Biometeorology, 42*(4), 177-182.

Soudani, K., le Maire, G., Dufrene, E., Francois, C., Delpierre, N., Ulrich, E., & Cecchini, S. (2008). Evaluation of the onset of green-up in temperate deciduous broadleaf forests derived from Moderate Resolution Imaging Spectroradiometer (MODIS) data. *Remote Sensing of Environment, 112*(5), 2643-2655.

Spano, D., Cesaraccio, C., Duce, P., & Snyder, R. L. (1999). Phenological stages of natural species and their use as climate indicators. *International Journal of Biometeorology, 42*(3), 124-133.

Stenset, N. E., Lutnaes, P. N., Bjarnadottir, V., Dahle, B., Fossum, K. H., Jigsved, P., . . . Swenson, J. E. (2016). Seasonal and annual variation in the diet of brown bears *Ursus arctos* in the boreal forest of southcentral Sweden. *Wildlife Biology, 22*(3), 107-116.

Sun, Y. J., Wang, J. F., Zhang, R. H., Gillies, R. R., Xue, Y., & Bo, Y. C. (2005). Air temperature retrieval from remote sensing data based on thermodynamics. *Theoretical and Applied Climatology, 80*(1), 37-48.

Thomas, C. D., Cameron, A., Green, R. E., Bakkenes, M., Beaumont, L. J., Collingham, Y. C., . . . Hannah, L. (2004). Extinction risk from climate change. *Nature, 427*(6970), 145-148.

van Rossum, G. and Drake, F.L. (2001). "Python Reference Manual." *PythonLabs*, Virginia, USA, 2001. URL: http://www.python.org.

Vancutsem, C., Ceccato, P., Dinku, T., & Connor, S. J. (2010). Evaluation of MODIS land surface temperature data to estimate air temperature in different ecosystems over Africa. *Remote Sensing of Environment, 114*(2), 449-465.

Walker, M. D., Wahren, C. H., Hollister, R. D., Henry, G. H. R., Ahlquist, L. E., Alatalo, J. M., . . . Wookey, P. A. (2006). Plant community responses to experimental warming across the tundra biome. *Proceedings of the National Academy of Sciences, 103*(5), 1342-1346.

Walther, G. R., Post, E., Convey, P., Menzel, A., Parmesan, C., Beebee, T. J. C., . . . Bairlein, F. (2002). Ecological responses to recent climate change. *Nature, 416*(6879), 389-395.

Wan, Z. (2014). New refinements and validation of the collection-6 MODIS land-surface temperature/emissivity product. *Remote Sensing of Environment, 140*, 36-45.

Wan, Z. M., Zhang, Y. L., Zhang, Q. C., & Li, Z. L. (2002). Validation of the land-surface temperature products retrieved from Terra Moderate Resolution Imaging Spectroradiometer data. *Remote Sensing of Environment, 83*(1-2), 163-180.

Wang, J.Y. (1960) A critique of the heat unit approach to plant response studies. *Ecology, 41*, 785-790.

Way, D. A., & Montgomery, R. A. (2015). Photoperiod constraints on tree phenology, performance and migration in a warming world. *Plant, cell & environment, 38*(9), 1725-1736.

White, K., Pontius, J., & Schaberg, P. (2014). Remote sensing of spring phenology in northeastern forests: A comparison of methods, field metrics and sources of uncertainty. *Remote Sensing of Environment, 148*(0), 97-107.

White, M. A., Running, S. W., & Thornton, P. E. (1999). The impact of growing-season length variability on carbon assimilation and evapotranspiration over 88 years in the eastern US deciduous forest. *International Journal of Biometeorology, 42*(3), 139-145.

Wielgolaski, F. E. (1999). Starting dates and basic temperatures in phenological observations of plants. *International Journal of Biometeorology, 42*(3), 158-168.

Williamson, S. N., Hik, D. S., Gamon, J. A., Kavanaugh, J. L., & Koh, S. (2013). Evaluating cloud contamination in clear-sky MODIS Terra daytime land surface temperatures using ground-based meteorology station observations. *Journal of Climate, 26*(5), 1551-1560.

Wilson, S. M., Madel, M. J., Mattson, D. J., Graham, J. M., Burchfiled, J. A., & Belsky, J. M. (2005). Natural landscape features, human-related attractants, and conflict hotspots: a spatial analysis of human-grizzly bear conflicts. *Ursus, 16*(1), 117-129.

Wolkovich, E. M., Cook, B. I., Allen, J. M., Crimmins, T. M., Betancourt, J. L., Travers, S. E., . . Cleland, E. E. (2012). Warming experiments underpredict plant phenological responses to climate change. *Nature, 485*(7399), 494-497.

Yang, S. S., Logan, J., & Coffey, D. L. (1995). Mathematical formulas for calculating the base temperature for calculating the base temperature for growing degree-days. *Agricultural and Forest Meteorology, 74*(1-2), 61-74.

Yu, R., Schwartz, M. D., Donnelly, A., & Liang, L. (2016). An observation-based progression modeling approach to spring and autumn deciduous tree phenology. *International Journal of Biometeorology, 60*(3), 335-349.

Zhang, F., Zhang, L.-W., Shi, J.-J., & Huang, J.-F. (2014). Soil Moisture Monitoring Based on Land Surface Temperature-Vegetation Index Space Derived from MODIS Data. *Pedosphere, 24*(4), 450-460.

Zhang, X. Y., Friedl, M. A., Schaaf, C. B., Strahler, A. H., Hodges, J. C. F., Gao, F., . . . Huete, A. (2003). Monitoring vegetation phenology using MODIS. *Remote Sensing of Environment, 84*(3), 471-475.

Zorer, R., Rocchini, D., Metz, M., Delucchi, L., Zottele, F., Meggio, F., & Neteler, M. (2013). Daily MODIS Land Surface Temperature data for the analysis of the heat requirements of grapevine varieties. *IEEE Transactions on Geoscience and Remote Sensing, 51*(4), 2128-2135.

Chapter Six: Conclusions

> Phenology affects nearly all aspects of ecology and evolution. Virtually all biological phenomena – from individual physiology to interspecific relationships to global nutrient fluxes – have annual cycles and are influenced by the timing of abiotic events (Forrest and Miller-Rushing 2010).

Plants intricately adjust their life cycles to the seasonality of the environments in which they inhabit. Shifts in the timing of their phenology will result from natural variations in climate and weather. A steady advance in the onset of spring green-up provides convincing evidence that plant species are being influenced by anthropogenic climate change (Cleland *et al*., 2007). As a bottom-up driver of numerous ecosystem processes, shifts in phenology will affect the trophic linkages that have some reliance on plants. Within this research program, a reliable remote sensing framework was developed to monitor phenological dynamics in near-real-time for use in broad-scale ecosystem monitoring with applications in wildlife management. Grounded in the concept that *air temperature is the main environmental factor that regulates phenology in temperate and boreal forests* (White *et al*., 1999; Linkosalo *et al*., 2006); The framework successfully employs a straightforward mechanistic approach in which air temperature is the key predictor of understory phenology. I found that thermal data was pivotal in resolving discrete phenophases in the target species, in particular the ecologically significant phases such as *fruiting* which are too subtle to detect spectrally. The mapped output provides clearly defined spatiotemporal patterns of understory phenology, estimating fruiting times of *S. canadensis* to within 2.4

days throughout western Alberta. Under climate change, the temporal shifts in nutritional availability provided by these plants are projected to be substantial – almost a three-week seasonal advance on average. The predictive accuracy of these phenology maps are invaluable for monitoring variability within seasons and across space, and provide a basis for assessing the long term effects of climate change on plant-animal interactions. The remote sensing framework developed through this research ultimately provides an environmental-modeling foundation that corresponds with the inherent seasonal dynamics of forest ecosystems.

6.1 Research Objectives Summary

The overall motivation of this research was to develop a remote sensing framework for monitoring distinct phenophases in understory vegetation, and to investigate the projected effects of climate change on phenological timing. The research objectives were as follows:

1. Evaluate the level of agreement between multi-scale field observations and time-lapse camera imagery for identifying phenophases in understory species.
2. Establish if understory air temperature can be estimated using MODIS land surface temperature imagery.
3. Determine the high-resolution spatiotemporal patterns of understory phenology throughout western Alberta using understory air temperatures.
4. Explore the effects of experimental warming on phenophase timing and project how this shift will alter phenology patterns on the landscape.

Summary descriptions of the significant outcomes of each objective are provided below; highlighting their incremental contributions towards a cohesive, overarching phenology monitoring framework.

1. The preliminary inquiry into the scope of broad-scale climate controls on regional phenology, summarized in Chapter 1, pointed to the need for more intensive, high-frequency observations of both temperature and plant development. The obvious research direction was to use satellite imagery as a means of capturing landscape-scale phenological patterns using plot-level observations on the ground. Comprehensive observations over such a large study area required autonomous observations using a remote camera network. Given their effectiveness in discerning seasonal phenology, it was important to determine if cameras could resolve individual phenophases by directly detecting the physical changes in a plant rather than the emitted spectral fluctuations over the course of a growing season. It was also important to discern, rather than assume, that camera observations were equivalent to those made by humans. Considering that these observations provided the foundation for the entire research program, an investigation was carried out to determine the phenological relationships across different scales in space. This effort was designed to evaluate the scales of observation undertaken in this work, and to reconcile the point-to-pixel problem so prolific in remote sensing research (Fisher *et al.*, 2006; Cleland *et al.*, 2007; Melaas *et al.*, 2016). The results revealed no significant difference between phenophase observations made by cameras and those made by field personnel. There was a slight temporal underestimation by the cameras, potentially a result of their limited field of view. It was also found that there is no significant difference between the phenology of an individual plant and the broader region up to 6.25 ha, which corresponds to a typical

MODIS product image pixel. The high confidence in detection accuracy of the cameras ensured that a camera network would provide reliable observations on which the framework could be based. Without the use of cameras, the broad regional extent of this research would have been prohibitive. Identifying the robust correlation of plant phenology over multiple-scales would later become essential when attempting to scale from the plot to the landscape.

2. Establishing a strategy for estimating understory air temperature from satellite observations posed a major research hurdle, and is the keystone of this research. Using MODIS LST and a suite of canopy structural metrics, forest characteristics, and topographic variables, instantaneous measurements of understory temperature within the observation plots were estimated to within 1.4°C. The modeling process highlighted a distinct difference between temperatures in the understory and those above the canopy observed directly by MODIS. Canopy structure and forest stand-type functioned to differentiate temperatures in these disparate regions of the forest, with LST explaining the largest proportion of variability in T_{ust}.

The next major obstacle was extending plot-level observations to the full spatial extent of the satellite imagery within the study area. The MODIS composite products were developed to mitigate cloud contamination by coalescing all of the clear pixels over a multi-day period into a single image. Since the finest composite period of 8 days was too coarse to identify short-lived phenophases in the understory, a procedure was required to remove cloud contamination from the daily LST imagery. A compound methodology derived from existing procedures (e.g. Metz *et al*., 2014; Huang *et al*., 2015) was adapted to effectively remove these cloud gaps. The missing values were estimated using

temporally adjacent clear imagery. This was preferred to the common method of statistically estimating values from long term averages, since it deviates from the overriding objective of providing near-real-time phenology monitoring. The result was cloud-free maps of daily average T_{ust} covering the extent of the study area with an all-weather accuracy of 2.2°C. The final product was generated at an enhanced resolution of 250 m, corresponding with the unit scale of the in situ plot observations.

3. Mapping the spatiotemporal pattern of understory plant phenology was pivotal in synthesizing the preceding methodological advancements into an overall mapping framework capable of delivering high- spatiotemporal-resolution estimates of understory phenology throughout western Alberta. The groundwork had been established through the production of the temporally continuous T_{ust} maps. Based on the effectiveness of thermal accumulations applied in agriculture, it was theorized that the GDD approach of predicting species life cycle stages would also work in an ecological context. The resulting phenology maps were accurate in predicting the appearance of fully ripe fruit on *S. canadensis* to within 2.4 days. Overall, the maps estimated the timing of all 12 reproductive phenophases with an average accuracy of 5.2 days. The mapping framework was highly successful except in the estimation of late-season phenology, which is likely controlled by factors beyond temperature. The extensibility of the framework was demonstrated on *H. alpinum*, whose unique morphology created observation challenges which were reflected in the results: the best estimates of peak crude protein were about 6 days from the in situ observations. For both plant species, there was no significant difference between estimates of phenophase start dates in the maps and those observed on the ground. The maps clearly express the timing and availability of plant nutrition for grizzly bears throughout the season

and across the study area. Correspondingly, these maps provide the foundation for food-driven species occurrence models, pinpointing critical habitat, identifying ecological sinks, reducing human-bear conflict, and moving away from static environmental mapping approaches.

4. The framework was designed to accommodate future climate scenarios, and to make projections on the impact of anthropogenic warming on understory plant phenology. This final objective explored the projected future impacts of climate change on the phenology of critical grizzly bear food-plants, principally *S. canadensis*. The projections were based on the IPCC emissions scenarios for moderate warming (B1) of 1.8°C, and aggressive warming (A2) of 3.4°C to capture the likely range of increased average temperature at the end of this century. Both scenarios produced considerable advances in phenological timing, the largest being under the A2 scenario with a shift in peak fruiting of 6.6 days per °C across the study area. These temporal shifts were corroborated through two seasons of experimental warming in climate-controlled growth chambers, which directly observed an advance in fully ripe fruit of 7 days per °C. The temporal changes were accompanied by large shifts in habitat extent across the study area, as these species exploit new niches under novel future climates. Species distribution models for *S. canadensis* and *H. alpinum* (derived by Roberts *et al*., 2014) were merged with the phenology maps to obtain the most plausible understanding of future climate change impact. The range of *S. canadensis* is projected to expand eastward into the foothills, bringing bears into areas of increased human use. Also, the duration of peak berry abundance will be reduced from that which currently exists. *Hedysarum alpinum* was found to lose habitat and migrate upslope to maintain ideal growing temperatures. This migration

to higher elevations may present early season foraging challenges for bear populations in the foothills. Future changes in the timing and distribution of food resources were found to be substantial. In the next few decades, we can expect to find grizzlies in areas where they are previously absent, or missing from areas of current habitat on account of denuded food resources. Using the phenology maps to monitor current trends may show that these changes may already be underway.

To conclude, the research objectives posed in this thesis were successfully realized and a remote sensing framework for producing accurate phenology maps of ecologically critical understory plant species has been developed. The extensibility to observe past, present, and future phenological patterns serves as a powerful tool for dynamic ecosystem modeling, and provides a strategy that can aid management decisions for species conservation at present and in the future.

6.2 Research Contributions

The research undertaken in this thesis has resulted in a number of methodological and theoretical contributions to the fields of remote sensing, forest ecology, vegetation phenology, and ecosystem management. Species interactions, seasonal phenology, and climate change are all dynamic processes; the major contribution of the framework is to provide phenology outputs that express the day-to-day changes in vegetation that drive these processes and correspond with the inherent dynamics of nature. The effort to recontextualize the thermal-physiological approach to understory phenology has made the remote sensing framework readily extensible for use elsewhere. The endeavor to limit complex process-based modeling and focus primarily on temperature makes the approach

both reliable and flexible for a variety of applications. This approach also provides a direct connection between the satellite sensor and very fine phenological developments in the understory. The development of a framework to explore forest ecology is a direct contribution to the pressing need for more intensive research into the effects of climate change within the understory. A letter published recently in the journal Science (De Frenne and Verheyen 2016) stressed the importance of focusing global attention to the lack of microclimate analysis within forest understories. The rationale is that only 27% of terrestrial land masses are covered in forest, yet two-thirds of global biodiversity resides beneath the canopy. The mapping framework therefore provides a mechanism to help expand ecological research into relatively underobserved forest microclimates.

The immediate contribution of this research is toward grizzly bear ecology and conservation within the western-Alberta study area. The primary catalyst of undertaking this research was to define the patterns of phenology and potential impacts of climate change within the ongoing Foothills Research Institute Grizzly Bear Program. It is within this scope that these maps will be applied in support of phenology and food-driven species occurrence models (Nielsen *et al*., 2003, 2010, 2016). The phenology maps provide a lucid perspective on present-day grizzly bear habitat variability, and also allow managers to anticipate future habitat-use dynamics as a result of climate change. The expectation is that the maps ultimately contribute to mitigating bear-human conflict and sustaining viable grizzly bear populations throughout the entirety of their present range.

In pursuit of the research objectives, a number of methodological contributions were derived in the process. The initial exploration into the effectiveness of the phenology cameras resulted in the development of an effective field protocol. This protocol works to

increase accuracy in phenophase detection by functioning to reduce subjectivity in field observations and imagery interpretations. This approach is also supported by the added knowledge that observations of a single camera effectively represents the phenology of a 6.25 ha region, at least for these particular species. This increases confidence in deploying a camera network in place of dedicated field crews which ultimately reduces overall effort and research costs. This protocol has been acquired by a USGS research project examining vegetation dynamics across the northwestern United States. This research is looking at the phenology and productivity of huckleberries (*Vaccinium membranaceum*) as a food source for grizzly bears and other species. The study will incorporate a variety of factors affecting berry productivity, including fire disturbance, insect defoliation, pollination ecology, and extreme weather events linked to climate change.

Other contributions include:

i. Confirmation of the theoretical hypothesis that climate change will significantly alter phenology in *S. canadensis*. This was accomplished through implementing the experimental warming scenarios within the climate-controlled growth chambers;

ii. The development of a semi-automated 'cloud removal' procedure derived in Chapter 4 provides a solution, at least in the context of this research, to the long-standing issue of cloud contamination in remotely sensed time-series imagery;

iii. Selected content of this research has been presented at the 6th International Conference on Climate Change: Impacts and Responses, and the Alberta BearSmart annual workshop;

iv. The overall research project was synopsized as part of the TED-Ed educational program which contributes to the general awareness of the unique and wide-ranging applications of remote sensing; and

v. The published manuscripts are formal contributions to the literature and the broader body of knowledge.

6.3 Recommendations for Future Research

While this thesis illustrates a number of substantial research contributions, there remains a large number of potential applications and some specific issues that require further analysis. The research issues and applications deemed most relevant are suggested below.

The immediate and obvious next step in the research is to explore the direct interaction between grizzly bears and the availability of digestible energy from plants across their range. It would be interesting to test support for a bottom-up hypothesis that grizzly bear movement corresponds to the *wave* of fruit availability. The intent is to pursue work similar to that of Cole *et al*. (2015), who discovered that the vegetation green-up signal uncovered spatial variation in phenological synchrony between birds (*Parus* spp.) and their environment. Or Armstrong *et al*. (2016), who detected population-level shifts in habitat-use as grizzly bears exploit resource waves of protein availability corresponding to salmon phenology. They suggest that phenological diversity in the arrival of food-resources is more important to mobile foragers than overall food abundance. There is a comprehensive dataset of existing GPS telemetry data for a sizeable number of grizzly bears in the study area, as well as coincident *S. canadensis* berry sugar content (°Bx) measurements that correspond with the phenology maps. The combination of these data

with models of shrub abundance will provide the next level of multi-scale species occurrence modeling for grizzly bears in the study area. Detecting a signal response to fruiting phenology is the first step in predicting areas of increased use by grizzly bears, identifying optimal foraging windows in critical habitat, and anticipating areas of heightened conflict. Nielsen *et al.* (2016) and Thackeray (2016) illustrate that species responses to food availability are controlled by a combination of factors and cannot be simplified by a bottom-up food chain paradigm. As species occurrence modeling becomes increasingly complex to include top-down controls and multi-trophic interactions, species phenology will provide a critical component in exploring ecosystem scale food-web dynamics.

One of the strategic abilities of the mapping framework is the capacity to forecast the effects of climate change. The scenarios explored in this research were defined by the projected increases in global annual average temperature, with variability between 1.8°C and 3.4°C. The framework incorporates these values by blanketing them on the baseline temperature patterns across the study area. This maintains the explicit values of the underlying T_{ust} and increases them equally given the selected scenario. This technique provides practical insight into the phenological changes to be expected in general. However, considering the complexity of climate systems and their impact on local weather, this projection analysis would benefit from spatially refined scenario inputs. Climate models specific to the study area would capture the anomalies, variability, and regionally specific temperature structures that are unique to the mountains of western Alberta. These scenarios can be obtained from the existing regional CMIP5 models used to calculate the broader IPCC climate simulations (e.g. Dirmeyer *et al*., 2013; Su *et al*., 2013). Another

option would be using projections derived through the North American Regional Climate Change Assessment Program (NARCCAP) which produce simulations at 30 km spatial resolution. Spatially refined future scenarios can be effectively integrated into forthcoming phenology research using these existing gridded models developed specifically for investigating uncertainties in regional scale climate projections.

The emphasis of future research will adhere to the objective of using the framework to explore new regions, investigate new plant species, and employ different sensors. The framework was developed to be portable and applicable anywhere in the world with marked seasonality. This flexibility relies on the broad coverage and rapid acquisition of time-series thermal imagery from Earth observing sensors. The conversion of this imagery to T_{air} or T_{ust} maps provides the amenable structure in which the AGDD functionality can be applied. Calculating the thermal developmental requirements of a plant species is attainable through a single season of observation, so long as that particular species has distinct phenology. This process can be repeated for any number of species existing within the study area extent; similar to the derivation of the *S. canadensis* and *H. alpinum* maps, both of which were simultaneously derived from the same underlying air temperature time-series. Therefore limitations of mapping extent and location are effectively constrained by the distribution and developmental traits of a species in response to seasonal temperature.

The research scale is also restricted by the computational power required to process the relatively dense image time-series. Where most comparable studies task multi-node, high performance computing systems with the processing burden (e.g. Neteler 2010; Metz *et al*., 2014), this framework was developed to be executed using top-of-the-line desktop computers. Understandably, as study areas reach continental scales and time-series' extend

beyond two years, the processing demands become immense. The framework can be adapted for use in Google Earth Engine (GEE), which is currently the most advanced cloud-based geospatial processing platform available. It provides a petabyte-scale imagery archive which includes MODIS LST. The highly extensible programming interface permits algorithm development at a global scale. Ultimately it will reduce processing times by orders of magnitude compared to desktop computation. As it stands, there is a perceivable slowdown in the workflow when the MODIS imagery stack is enhanced to 250 m, increasing the resolution to 20 million pixels per image. Such steep increases in processing demand would be imperceptible if the framework were migrated to the GEE platform. This does not immediately imply that the MODIS imagery be replaced with an ultra-high-resolution equivalent because of the intrinsic physical bounds of thermal radiation. The long wavelengths of thermal emissivity necessitate larger pixels to accurately resolve surface temperatures, therefore spatial resolution will always be moderate compared to visible-spectrum sensors. However, the Visible Infrared Imaging Radiometer Suite (VIIRS) is an example of the advancement in remotely-sensed thermal imaging. Launched in 2011, VIIRS has 750 m thermal resolution that improves on the MODIS 1 km product and has similar radiometric accuracy. VIIRS scan and orbit geometries provide global coverage every two days, but is only affixed to a single platform. Ingestion of the VIIRS dataset into the GEE platform has yet to occur but is expected to take place in the near future. With the advent of such an immensely capable processing environment, GEE promises to rapidly accelerate research in global phenological dynamics.

Fully automated cloud-based workflows unlock the potential of phenology mapping at the ecosystem-scale. Future applications of the framework will move toward

exploring the spatial responses of mobile foragers to vegetation phenology waves, with a focus on landscape connectivity and movement through critical habitat corridors. This research is particularly crucial as climate change alters animal movements as they seek optimal foraging habitat across increasingly fragmented landscapes. For example, the Yellowstone to Yukon Conservation Initiative is a continental-scale conservation effort in which phenological data could work to identify seasonal and trending changes affecting habitat connectivity; thereby determining which phenological factors contribute to the design of effective transboundary wildlife corridors (Beier *et al*., 2011; Chester 2015). Advances in GPS positioning technologies capture animal locations at very high spatial and temporal granularities. The daily phenology maps provide spatiotemporal intervals that correspond to these fine-scale changes in animal movement. Systems such as the Environmental-Data Automated Track Annotation (*Env-Data*) can be used to develop linkages between these datasets while incorporating other factors affecting movement such as topography and landscape disturbances (Dodge *et al*., 2013). This will likely be the approach used for the proposed research of tracing grizzly bear movements in response to *S. canadensis* phenology. There are numerous other ecological phenomena driven by temperature and seasonality that can be investigated in the future. Some examples include predicting wildfire activity (Westerling *et al*., 2006; Bajocco *et al*., 2010), wildlife pathology and vector-borne diseases (Jones *et al*., 2008; Harvell *et al*., 2009), and detecting invasive plant dispersal under climate change (Wolkovich *et al*., 2012). Along with a continued effort to illuminate species ecology in forest understories, there is a wealth of exciting research directions to be explored. ❧

6.4 Bibliography

Alessandri, A., Gualdi, S., Polcher, J., & Navarra, A. (2007). Effects of land surface-vegetation on the boreal summer surface climate of a GCM. *Journal of Climate, 20*(2), 255-278.

Araujo, M. B., & Guisan, A. (2006). Five (or so) challenges for species distribution modelling. *Journal of Biogeography, 33*(10), 1677-1688.

Ault, T. R., Macalady, A. K., Pederson, G. T., Betancourt, J. L., & Schwartz, M. D. (2011). Northern hemisphere modes of variability and the timing of spring in western North America. *Journal of Climate, 24*(15), 4003-4014.

Badeck, F.-W., Bondeau, A., Bottcher, K., Doktor, D., Lucht, W., Schaber, J., & Sitch, S. (2004). Responses of spring phenology to climate change. *New Phytologist, 162*(2), 295-309.

Barr, A., Black, T. A., & McCaughey, H. (2009). Climatic and phenological controls of the carbon and energy balances of three contrasting boreal forest ecosystems in western Canada *Phenology of ecosystem processes* (pp. 3-34): Springer.

Bater, C. W., Coops, N. C., Wulder, M. A., Nielsen, S. E., McDermid, G., & Stenhouse, G. B. (2011). Design and installation of a camera network across an elevation gradient for habitat assessment. *Instrumentation Science & Technology, 39*(3), 231-247.

Beaubien, E. G., & Freeland, H. J. (2000). Spring phenology trends in Alberta, Canada: links to ocean temperature. *International Journal of Biometeorology, 44*(2), 53-59.

Bennie, J., Kubin, E., Wiltshire, A., Huntley, B., & Baxter, R. (2009). Predicting spatial and temporal patterns of bud-burst and spring frost risk in north-west Europe: the implications of local adaptation to climate. *Global Change Biology*.

Bokhorst, S., Bjerke, J. W., Bowles, F. W., Melillo, J., Callaghan, T. V., & Phoenix, G. K. (2008). Impacts of extreme winter warming in the sub-Arctic: growing season responses of dwarf shrub heathland. *Global Change Biology*.

Brown, T. B., Hultine, K. R., Steltzer, H., Denny, E. G., Denslow, M. W., Granados, J., . . SanClements, M. (2016). Using phenocams to monitor our changing Earth: toward a global phenocam network. *Frontiers in Ecology and the Environment, 14*(2), 84-93.

Busetto, L., Colombo, R., Migliavacca, M., Cremonese, E., Meroni, M., Galvagno, M., . . Pari, E. (2010). Remote sensing of larch phenological cycle and analysis of relationships with climate in the Alpine region. *Global Change Biology, 16*(9), 2504-2517.

Butt, N., Seabrook, L., Maron, M., Law, B. S., Dawson, T. P., Syktus, J., & McAlpine, C. A. (2015). Cascading effects of climate extremes on vertebrate fauna through changes to low-latitude tree flowering and fruiting phenology. *Global Change Biology, 21*(9), 3267-3277.

Campbell, R. K. (1974). Use of phenology for examining provenance transfers in reforestation of Douglas-fir. *Journal of Applied Ecology, 11*(3), 1069-1080.

Carlson, T. N., & Ripley, D. A. (1997). On the relation between NDVI, fractional vegetation cover, and leaf area index. *Remote Sensing of Environment, 62*(3), 241-252.

Chuine, I., & Beaubien, E. G. (2001). Phenology is a major determinant of tree species range. *Ecology Letters, 4*(5), 500-510.

Cleland, E. E., Chuine, I., Menzel, A., Mooney, H. A., & Schwartz, M. D. (2007). Shifting plant phenology in response to global change. *Trends in Ecology & Evolution, 22*(7), 357-365.

Cook, B. I., Smith, T. M., & Mann, M. E. (2005). The North Atlantic Oscillation and regional phenology prediction over Europe. *Global Change Biology, 11*(6), 919-926.

Coops, N. C., Duro, D. C., Wulder, M. A., & Han, T. (2007). Estimating afternoon MODIS land surface temperatures (LST) based on morning MODIS overpass, location and elevation information. *International Journal of Remote Sensing, 28*(10), 2391-2396.

Coops, N. C., Hilker, T., Bater, C. W., Wulder, M. A., Nielsen, S. E., McDermid, G., & Stenhouse, G. (2012). Linking ground-based to satellite-derived phenological metrics in support of habitat assessment. *Remote Sensing Letters, 3*(3), 191-200.

Crimmins, M. A., & Crimmins, T. M. (2008). Monitoring plant phenology using digital repeat photography. *Environmental Management, 41*(6), 949-958.

Davis, H., Weir, R. D., Hamilton, A. N., & Deal, J. A. (2006). Influence of phenology on site selection by female American black bears in coastal British Columbia. *Ursus, 17*(1), 41-51.

de Beurs, K. M., & Henebry, G.M. (2010). Spatio-temporal statistical methods for modeling land surface phenology. In: Hudson, I.L., & Keatley, M.R. (Ed.), *Phenological Research: Methods for Environmental and Climate Change Analysis.* (pp. 177-208). Dordrecht: Springer.

De Frenne, P., & Verheyen, K. (2016). Weather stations lack forest data. *Science, 351*(6270), 234-234.

Deering, D. W. (1978). Rangeland reflectance characteristics measured by aircraft and spacecraft sensors. Ph.D. dissertation, Texas A&M University, College Station, Texas, p. 338.

Defila, C., & Clot, B. (2001). Phytophenological trends in Switzerland. *International Journal of Biometeorology, 45*(4), 203-207.

Demarée, G. R. (2009). The phenological observations and networking of Adolphe Quetelet at the Royal Observatory of Brussels. *Italian Journal of Agrometeorology, 1*, 22-24.

Dubé, P., Perry, L. P., & Vittum, M. (1984). Instructions for phenological observations: lilac and honeysuckle. *Bulletin/Vermont Agricultural Experiment Station* (USA).

Edwards, M., & Richardson, A. J. (2004). Impact of climate change on marine pelagic phenology and trophic mismatch. *Nature, 430*(7002), 881-884.

Ehrlich, P. R. (1986). *The Machinery of Nature*. New York: Simon and Shuster.

Fenner, M. (1998). The phenology of growth and reproduction in plants. *Perspectives in Plant Ecology, Evolution and Systematics, 1*(1), 78-91.

Fisher, J. I., Mustard, J. F., & Vadeboncoeur, M. A. (2006). Green leaf phenology at Landsat resolution: Scaling from the field to the satellite. *Remote Sensing of Environment, 100*(2), 265-279.

Fisher, J. I., Richardson, A. D., & Mustard, J. F. (2007). Phenology model from surface meteorology does not capture satellite-based greenup estimations. *Global Change Biology, 13*(3), 707-721.

Friedrich, T., Timmermann, A., Tigchelaar, M., Elison Timm, O., & Ganopolski, A. (2016). Nonlinear climate sensitivity and its implications for future greenhouse warming. *Science Advances, 2*(11).

Goward, S. N., Markham, B., Dye, D. G., Dulaney, W., & Yang, J. L. (1991). Normalized difference vegetation index measurements from the advanced very high-resolution radiometer. *Remote Sensing of Environment, 35*(2-3), 257-277.

Graham, E. A., Riordan, E. C., Yuen, E. M., Estrin, D., & Rundel, P. W. (2010). Public Internet-connected cameras used as a cross-continental ground-based plant phenology monitoring system. *Global Change Biology, 16*(11), 3014-3023.

Haggerty, B. P., & Mazer, S. J. (2008). The phenology handbook. *University of California, Santa Barbara*, P41.

Hallett, T. B., Coulson, T., Pilkington, J. G., Clutton-Brock, T. H., Pemberton, J. M., & Grenfell, B. T. (2004). Why large-scale climate indices seem to predict ecological processes better than local weather. *Nature, 430*(6995), 71-75.

Hänninen, H. (1995). Effects of climatic change on trees from cool and temperate regions: an ecophysiological approach to modelling of bud burst phenology. *Canadian Journal of Botany, 73*(2), 183-199.

Hanninen, H., & Kramer, K. (2007). A framework for modelling the annual cycle of trees in boreal and temperate regions. *Silva Fennica, 41*(1), 167-205.

He, K. S., Zhang, J. T., & Zhang, Q. F. (2009). Linking variability in species composition and MODIS NDVI based on beta diversity measurements. *Acta Oecologica-International Journal of Ecology, 35*(1), 14-21.

Hilker, T., Wulder, M. A., Coops, N. C., Linke, J., McDermid, G., Masek, J. G., . . . White, J. C. (2009). A new data fusion model for high spatial- and temporal-resolution mapping of forest disturbance based on Landsat and MODIS. *Remote Sensing of Environment, 113*(8), 1613-1627.

Huete, A., Didan, K., Miura, T., Rodriguez, E. P., Gao, X., & Ferreira, L. G. (2002). Overview of the radiometric and biophysical performance of the MODIS vegetation indices. *Remote Sensing of Environment, 83*(1-2), 195-213.

Huete, A., Justice, C., & Van Leeuwen, W. (1999). MODIS vegetation index (MOD13). *Algorithm theoretical basis document, 3*, 213.

Ide, R., & Oguma, H. (2010). Use of digital cameras for phenological observations. *Ecological Informatics, 5*(5), 339-347.

Inouye, D. W. (2008). Effects of climate change on phenology, frost damage, and floral abundance of montane wildflowers. *Ecology, 89*(2), 353-362.

Inouye, D. W., & McGuire, A. D. (1991). Effects of snowpack on timing and abundance of flowering in *delphinium-nelsonii* (*ranunculaceae*) - implications for climate change. *American Journal of Botany, 78*(7), 997-1001.

IPCC. (2014). Summary for Policymakers. In C. B. Field, V. R. Barros, D. J. Dokken, K. J. Mach, M. D. Mastrandrea, T. E. Bilir, M. Chatterjee, K. L. Ebi, Y. O. Estrada, R. C. Genova, B. Girma, E. S. Kissel, A. N. Levy, S. MacCracken, P. R. Mastrandrea & L. L. White (Eds.), Climate Change 2014: Impacts, Adaptation, and Vulnerability. Part A: Global and Sectoral Aspects. Contribution of Working Group II to the Fifth Assessment Report of the Intergovernmental Panel on Climate Change (pp. 1-32). Cambridge, United Kingdom, and New York, NY, USA: Cambridge University Press.

Keeling, C. D., Chin, J. F. S., & Whorf, T. P. (1996). Increased activity of northern vegetation inferred from atmospheric CO2 measurements. *Nature, 382*(6587), 146-149.

Klosterman, S., Hufkens, K., Gray, J., Melaas, E., Sonnentag, O., Lavine, I., . . . Richardson, A. (2014). Evaluating remote sensing of deciduous forest phenology at multiple spatial scales using PhenoCam imagery.

Kudo, G., & Ida, T. Y. (2013). Early onset of spring increases the phenological mismatch between plants and pollinators. *Ecology*, *94*(10), 2311-2320.

Latif, M., & Barnett, T. P. (1994). Causes of decadal climate variability over the north Pacific and North-America. *Science*, *266*(5185), 634-637.

Li, A., Liang, S., Wang, A., & Huang, C. (2012). Investigating the impacts of the North Atlantic Oscillation on global vegetation changes by a remotely sensed vegetation index. *International Journal of Remote Sensing*, *33*(22), 7222-7239.

Lieth, H. (1974) *Phenology and Seasonality Modeling*. Springer-Verlag, Heidelberg, pp. 444.

Linkosalo, T., Lappalainen, H. K., & Hari, P. (2008). A comparison of phenological models of leaf bud burst and flowering of boreal trees using independent observations. *Tree Physiology*, *28*(12), 1873-1882.

Magoon, C., & Culpepper, C. W. (1932). Response of sweet corn to varying temperatures from time of planting to canning maturity: US Department of Agriculture.

Mantua, N. J., Hare, S. R., Zhang, Y., Wallace, J. M., & Francis, R. C. (1997). A Pacific interdecadal climate oscillation with impacts on salmon production. *Bulletin of the American Meteorological Society*, *78*(6), 1069-1079.

McCabe, G. J., Ault, T. R., Cook, B. I., Betancourt, J. L., & Schwartz, M. D. (2012). Influences of the El Niño Southern Oscillation and the Pacific Decadal Oscillation on the timing of the North American spring. *International Journal of Climatology*, *32*(15), 2301-2310.

Meier, U. (2003). Phenological growth stages *Phenology: an integrative environmental science* (pp. 269-283): Springer.

Menzel, A., & Fabian, P. (1999). Growing season extended in Europe. *Nature*, *397*(6721), 659-659.

Misra, G., Buras, A., & Menzel, A. (2016). Effects of different methods on the comparison between land surface and ground phenology – a methodological case study from south-western Germany. *Remote Sensing*, *8*(9), 753.

Morain, S. A. (1974). Phenology and remote sensing. In: *Phenology and seasonality modeling* (pp. 55-75): Springer, Berlin Heidelberg.

Morellato, L. P. C., Alberton, B., Alvarado, S. T., Borges, B., Buisson, E., Camargo, M. G. G., . . Leite, P. T. (2016). Linking plant phenology to conservation biology. *Biological Conservation, 195*, 60-72.

Morisette, J. T., Richardson, A. D., Knapp, A. K., Fisher, J. I., Graham, E. A., Abatzoglou, J., . . . Liang, L. (2009). Tracking the rhythm of the seasons in the face of global change: phenological research in the 21st century. *Frontiers in Ecology and the Environment, 7*(5), 253-260.

Mostovoy, G. V., King, R. L., Reddy, K. R., Kakani, V. G., & Filippova, M. G. (2006). Statistical estimation of daily maximum and minimum air temperatures from MODIS LST data over the State of Mississippi. *Giscience & Remote Sensing, 43*(1), 78-110.

Myking, T. (1997). Effects of constant and fluctuating temperature on time to budburst in *Betula pubescens* and its relation to bud respiration. *Trees-Structure and Function, 12*(2), 107-112.

Myneni, R. B., Hall, F. G., Sellers, P. J., & Marshak, A. L. (1995). The interpretation of spectral vegetation indexes. *IEEE Transactions on Geoscience and Remote Sensing, 33*(2), 481-486.

Nagai, S., Nasahara, K. N., Inoue, T., Saitoh, T. M., & Suzuki, R. (2016). Review: advances in in situ and satellite phenological observations in Japan. *International Journal of Biometeorology, 60*(4), 615-627.

Nemanill, R. (1997). Increased plant growth in the northern high latitudes from 1981 to 1991.

Neteler, M. (2010). Estimating daily land surface temperatures in mountainous environments by reconstructed MODIS LST data. *Remote Sensing, 2*(1), 333-351.

Niclos, R., Valiente, J. A., Barbera, M. J., & Caselles, V. (2014). land surface air temperature retrieval from EOS-MODIS images. *IEEE Geoscience and Remote Sensing Letters, 11*(8), 1380-1384.

Nielsen, S. E., Boyce, M. S., Stenhouse, G. B., & Munro, R. H. M. (2003). Development and testing of phenologically driven grizzly bear habitat models. *Ecoscience, 10*(1), 1-10.

Nijland, W., Bolton, D. K., Coops, N. C., & Stenhouse, G. (2016). Imaging phenology: scaling from camera plots to landscapes. *Remote Sensing of Environment, 177*, 13-20.

Nijland, W., Coops, N. C., Coogan, S. C. P., Bater, C. W., Wulder, M. A., Nielsen, S. E., . Stenhouse, G. B. (2013). Vegetation phenology can be captured with digital repeat photography and linked to variability of root nutrition in Hedysarum alpinum. *Applied Vegetation Science, 16*(2), 317-324.

Parmesan, C. (2006). Ecological and evolutionary responses to recent climate change. *Annual Review of Ecology Evolution and Systematics, 37*, 637-669.

Parmesan, C., Ryrholm, N., Stefanescu, C., Hill, J. K., Thomas, C. D., Descimon, H., . . . Warren, M. (1999). Poleward shifts in geographical ranges of butterfly species associated with regional warming. *Nature, 399*(6736), 579-583.

Parmesan, C., & Yohe, G. (2003). A globally coherent fingerprint of climate change impacts across natural systems. *Nature, 421*(6918), 37-42.

Penuelas, J., Rutishauser, T., & Filella, I. (2009). Phenology feedbacks on climate change. *Science, 324*(5929), 887-888.

Power, M. E. (1992). Top-down and bottom-up forces in food webs - do plants have primacy. *Ecology, 73*(3), 733-746.

Pudas, E., Leppälä, M., Tolvanen, A., Poikolainen, J., Venäläinen, A., & Kubin, E. (2008). Trends in phenology of Betula pubescens across the boreal zone in Finland. *International Journal of Biometeorology, 52*(4), 251-259.

Puppi, G. (2007). Origin and development of phenology as a science. *Ital J Agrometeorol, 3*, 24-29.

Rathcke, B., & Lacey, E. P. (1985). Phenological patterns of terrestrial plants. *Annual Review of Ecology and Systematics, 16*, 179-214.

Redmond, K. T., & Koch, R. W. (1991). Surface climate and streamflow variability in the western United-States and their relationship to large-scale circulation indexes. *Water Resources Research, 27*(9), 2381-2399.

Reed, B. C. (2006). Trend analysis of time-series phenology of North America derived from satellite data. *Giscience & Remote Sensing, 43*(1), 24-38.

Reed, B. C., Brown, J. F., Vanderzee, D., Loveland, T. R., Merchant, J. W., & Ohlen, D. O. (1994). Measuring phenological variability from satellite imagery. *Journal of Vegetation Science, 5*(5), 703-714.

Reed, B. C., Schwartz, M. D., & Xiao, X. (2009). Remote Sensing Phenology. In: A. Noormets (Ed.), *Phenology of Ecosystem Processes: Applications in Global Change Research* (pp. 231-246). Dordrecht: Springer.

Richardson, A., & O'Keefe, J. (2009). Phenological differences between understory and overstory. In: A. Noormets (Ed.), *Phenology of Ecosystem Processes* (pp. 87-117): Springer, New York.

Richardson, A. D., Braswell, B. H., Hollinger, D. Y., Jenkins, J. P., & Ollinger, S. V. (2009). Near-surface remote sensing of spatial and temporal variation in canopy phenology. *Ecological Applications, 19*(6), 1417-1428.

Richardson, A. D., Jenkins, J. P., Braswell, B. H., Hollinger, D. Y., Ollinger, S. V., & Smith, M. L. (2007). Use of digital webcam images to track spring green-up in a deciduous broadleaf forest. *Oecologia, 152*(2), 323-334.

Root, T. L., Price, J. T., Hall, K. R., Schneider, S. H., Rosenzweig, C., & Pounds, J. A. (2003). Fingerprints of global warming on wild animals and plants. *Nature, 421*(6918), 57-60.

Schwartz, M. D. (1997). Spring index models: an approach to connecting satellite and surface phenology. *Phenology in seasonal climates I*, 23-38.

Schwartz, M. D. (1999). Advancing to full bloom: planning phenological research for the 21st century. *International Journal of Biometeorology, 42*(3), 113-118.

Schwartz, M. D. (2003). Phenology: An Integrative Environmental Science. Dordrecht: Kluwer Academic Publishers.

Schwartz, M. D., Ahas, R., & Aasa, A. (2006). Onset of spring starting earlier across the Northern Hemisphere. *Global Change Biology, 12*(2), 343-351.

Schwartz, M. D., & Reed, B. C. (1999). Surface phenology and satellite sensor-derived onset of greenness: an initial comparison. *International Journal of Remote Sensing, 20*(17), 3451-3457.

Schwartz, M. D., Reed, B. C., & White, M. A. (2002). Assessing satellite-derived start-of-season measures in the conterminous USA. *International Journal of Climatology, 22*(14), 1793-1805.

Shabbar, A., & Khandekar, M. (1996). The impact of El Niño-Southern Oscillation on the temperature field over Canada. *Atmosphere-Ocean, 34*(2), 401-416.

Sherry, R. A., Zhou, X. H., Gu, S. L., Arnone, J. A., Schimel, D. S., Verburg, P. S., . . . Luo, Y. Q. (2007). Divergence of reproductive phenology under climate warming. *Proceedings of the National Academy of Sciences of the United States of America, 104*(1), 198-202.

Sonnentag, O., Hufkens, K., Teshera-Sterne, C., Young, A. M., Friedl, M., Braswell, B. H., . . . Richardson, A. D. (2012). Digital repeat photography for phenological research in forest ecosystems. *Agricultural and Forest Meteorology, 152*, 159-177.

Spano, D., Cesaraccio, C., Duce, P., & Snyder, R. L. (1999). Phenological stages of natural species and their use as climate indicators. *International Journal of Biometeorology, 42*(3), 124-133.

Sparkes, T., Carey, P., & Coombes, J. (1997). First leafing dates of trees in Surrey between 1947 and 1996. *London Naturalist, 76*, 15-20.

StataCorp. (2013). Stata Statistical Software: Release 13. College Station, TX: StataCorp LP.

Thuiller, W. (2007). Biodiversity - Climate change and the ecologist. *Nature, 448*(7153), 550-552.

Trigo, I. F., Monteiro, I. T., Olesen, F., & Kabsch, E. (2008). An assessment of remotely sensed land surface temperature. *Journal of Geophysical Research-Atmospheres, 113*(D17).

Tuanmu, M. N., Vina, A., Bearer, S., Xu, W. H., Ouyang, Z. Y., Zhang, H. M., & Liu, J. G. (2010). Mapping understory vegetation using phenological characteristics derived from remotely sensed data. *Remote Sensing of Environment, 114*(8), 1833-1844.

van Leeuwen, W. J. D., Huete, A. R., & Laing, T. W. (1999). MODIS vegetation index compositing approach: A prototype with AVHRR data. *Remote Sensing of Environment, 69*(3), 264-280.

Visser, M. E., & Both, C. (2005). Shifts in phenology due to global climate change: the need for a yardstick. *Proceedings of the Royal Society B-Biological Sciences, 272*(1581), 2561-2569.

Wagenmakers, E.-J., & Farrell, S. (2004). AIC model selection using Akaike weights. *Psychonomic bulletin & review, 11*(1), 192-196.

Wan, Z. M., & Dozier, J. (1996). A generalized split-window algorithm for retrieving land-surface temperature from space. *IEEE Transactions on Geoscience and Remote Sensing, 34*(4), 892-905.

Wan, Z. M., Zhang, Y. L., Zhang, Q. C., & Li, Z. L. (2002). Validation of the land-surface temperature products retrieved from Terra Moderate Resolution Imaging Spectroradiometer data. *Remote Sensing of Environment, 83*(1-2), 163-180.

Warren, R. J., Bahn, V., & Bradford, M. A. (2011). Temperature cues phenological synchrony in ant mediated seed dispersal. *Global Change Biology, 17*(7), 2444-2454.

White, M. A., de Beurs, K. M., Didan, K., Inouye, D. W., Richardson, A. D., Jensen, O. P., . . . Lauenroth, W. K. (2009). Intercomparison, interpretation, and assessment of spring phenology in North America estimated from remote sensing for 1982-2006. *Global Change Biology, 15*(10), 2335-2359.

White, M. A., & Nemani, R. R. (2006). Real-time monitoring and short-term forecasting of land surface phenology. *Remote Sensing of Environment, 104*(1), 43-49.

White, M. A., Running, S. W., & Thornton, P. E. (1999). The impact of growing-season length variability on carbon assimilation and evapotranspiration over 88 years in the eastern US deciduous forest. *International Journal of Biometeorology, 42*(3), 139-145.

White, M. A., Thornton, P. E., & Running, S. W. (1997). A continental phenology model for monitoring vegetation responses to interannual climatic variability. *Global Biogeochemical Cycles, 11*(2), 217-234.

Williams, J. W., & Jackson, S. T. (2007). Novel climates, no-analog communities, and ecological surprises. *Frontiers in Ecology and the Environment, 5*(9), 475-482.

Wolter, K., & Timlin, M. S. (1998). Measuring the strength of ENSO events: How does 1997/98 rank? *Weather, 53*(9), 315-324.

Zhang, X. Y., Friedl, M. A., Schaaf, C. B., & Strahler, A. H. (2004). Climate controls on vegetation phenological patterns in northern mid- and high latitudes inferred from MODIS data. *Global Change Biology, 10*(7), 1133-1145.

Zhang, X. Y., Friedl, M. A., Schaaf, C. B., Strahler, A. H., Hodges, J. C. F., Gao, F., . . . Huete, A. (2003). Monitoring vegetation phenology using MODIS. *Remote Sensing of Environment, 84*(3), 471-475.